RSC Advances



REVIEW

View Article Online
View Journal | View Issue



Cite this: RSC Adv., 2025, 15, 30921

Metal-organic framework/MXene-based materials: preparations and applications

Shasha Zheng, (10)* Keke Zhou, Xiaoxue Zhang and Ning Ren

Metal-organic framework (MOF) materials have attracted significant attention due to their high surface area and adjustable pore structure, which enable potential applications across various fields. However, their practical application is often hindered by poor electrical conductivity and limited structural stability. Integrating MOF with two-dimensional transition metal carbides/nitrides (MXene) offers a powerful strategy to overcome these limitations, synergistically combining the porous architecture of MOF with the exceptional conductivity and mechanical robustness of MXenes. Notably, the performance of MOF/MXene-based materials is governed by the diversification of MOF components. This review provides a systematic and comprehensive analysis of MOF/MXene-based materials, emphasizing a component-driven design approach. These materials are classified into three different types: pure MOF/MXene, MOF composite/MXene, and MOF derivative/MXene, and their synthetic strategies are detailed, including *in situ* growth, solvothermal/hydrothermal methods, self-assembly, and co-precipitation method. Further exploration was conducted on their advanced performance in multifunctional applications such as batteries, supercapacitors, sensors, catalysts, and electromagnetic wave absorbing materials.

Received 22nd June 2025 Accepted 11th August 2025

DOI: 10.1039/d5ra04436g

rsc.li/rsc-advances

Introduction

The relentless progress in scientific innovation has driven the development of novel nanomaterials, whose outstanding physicochemical characteristics enable extensive applicability across diverse fields. 1-4 Among these, metal-organic framework (MOF) nanomaterials, a class of compounds constructed through the coordination of metal ions or clusters with organic ligands to form one-, two-, and three-dimensional (1D, 2D, and 3D) structures, have garnered significant attention.5-8 The exceptionally high specific surface area and tunable porosity of MOF materials endow them with superior adsorption and separation performance.9-11 Furthermore, the structural and functional versatility of MOF materials has enabled their application in fields such as catalysis, 12-14 energy storage, 15-17 and so on. 18-20 Despite these advantages, MOF materials also present certain limitations, including insufficient chemical stability, inadequate mechanical strength, poor electrical conductivity, and restricted adsorption capacity and selectivity.21-23 To address these challenges and fully exploit the potential of MOF materials, the design of MOF-based composites has emerged as a promising strategy.24-27 By integrating MOF materials with other functional materials, synergistic effects can be achieved, effectively combining the strengths of each component while compensating for their individual deficiencies.²⁸⁻³¹

materials science.32-36 Its unique 2D layered structure imparts exceptional electrical conductivity, good mechanical flexibility, intrinsic hydrophilicity, and abundant surface functional groups (e.g., -OH, -F, -O). These properties render MXene a highly promising material for diverse applications, including batteries, 42,43 supercapacitors (SCs), 44,45 catalysis, 46,47 water purification,48-50 adsorption,51,52 sensors,53-55 and various other fields. 56-60 Nevertheless, practical implementation of MXene is hindered by several intrinsic limitations, such as oxidative instability, restacking of the 2D nanosheets, and a relatively limited number of accessible active sites. 61-63 A particularly effective approach to overcome these challenges involves the integration of MXene with MOF porous materials. This hybridization generates significant synergistic effects: the porous structure of MOF materials can serve as a structural scaffold to prevent the restacking of MXene nanosheets, thereby preserving their high surface area and excellent electrical conductivity.64-68 Conversely, the highly conductive MXene network facilitates efficient electron transport, serving as a rapid charge transfer channel that markedly enhances the typically sluggish charge transfer kinetics of the inherently less conductive MOF component. 69-71 The distinctiveness of MOF/ MXene-based materials lies in the unique synergy offered by

MXene, which sets them apart from other common MOF-based

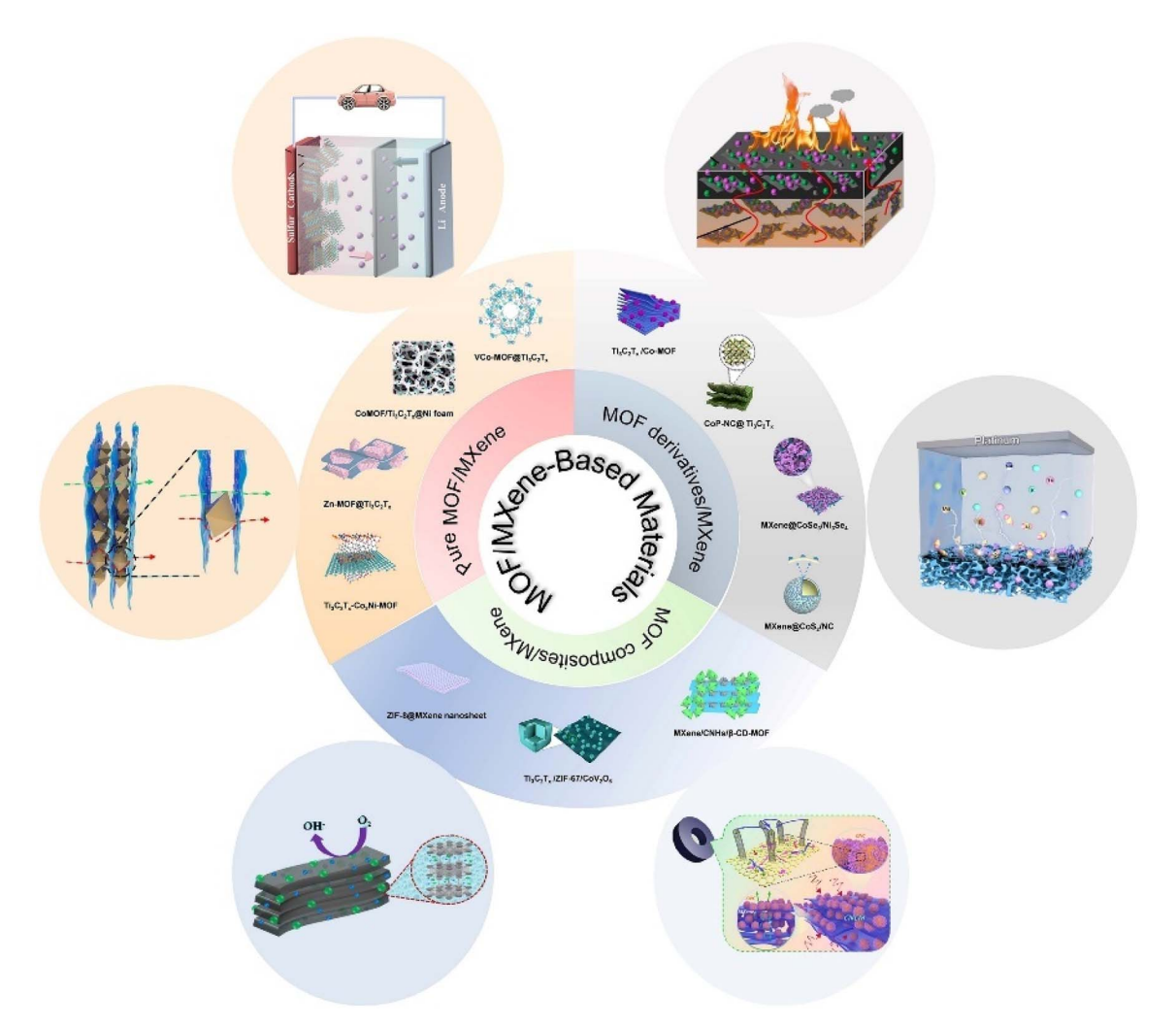
hybrids. Compared to MOF/carbon nanotubes (CNTs), the 2D

MXene, a novel class of 2D transition metal carbides and

nitrides with the general formula $M_{n+1}X_nT_x$ (M = early transition metals; X = carbon and/or nitrogen; $T_x = \text{surface func-}$

tional groups), has garnered significant attention in advanced

College of Energy Engineering, Huanghuai University, Zhumadian, 463000, Henan, P. R. China. E-mail: zhengshasha@huanghuai.edu.cn



Scheme 1 Overview of MOF/MXene-based materials and their application fields.

structure of MXene provides a larger contact interface and better dispersion. 63,72 Unlike MOF/graphene, MXene's rich surface functional groups enable strong chemical bonding with MOF materials, forming stable heterojunctions. 73,74 In contrast to MOF/metal nanoparticles (NPs), MXene enhances both conductivity and stability cost-effectively. 75,76 Finally, compared to MOF/polymer composites, MXene integration directly addresses the core issue of poor electrical conductivity. 77-79 This multifaceted advantage positions MOF/MXene-based materials as a highly attractive class of materials.

Numerous comprehensive reviews have been conducted on MOF/carbon-based materials, ⁸⁰⁻⁸⁴ MOF/polymers, ⁸⁵⁻⁹⁰ MOF/ quantum dots (QDs), ⁹¹⁻⁹³ MOF/metal NPs, ⁹⁴⁻⁹⁶ and other MOF composites. ⁹⁷⁻¹⁰³ However, in the field of MOF/MXene-based materials, despite a series of valuable reviews have been reported, they generally have limited scope. Many reviews focus on specific applications (such as energy storage, ^{72,77,104-109} catalysis, ^{75,110,111} biomedical, ⁷⁸ wastewater treatment, ^{112,113} electromagnetic interference shielding, ¹¹⁴ *etc.*) or specific types of materials (such as MOF derivatives/MXene¹¹⁵), resulting in a fragmented understanding of this field. Therefore, there is

currently a lack of a comprehensive, systematic, and up-to-date review that covers the complete system of MOF/MXene-based materials from basic classification, synthesis strategies to diverse applications. Compared with these existing reviews, the main purpose of this review is to provide a comprehensive and detailed analysis of MOF/MXene-based materials, providing a reference for researchers in materials science, chemistry, and engineering fields to fully understand this dynamic field.

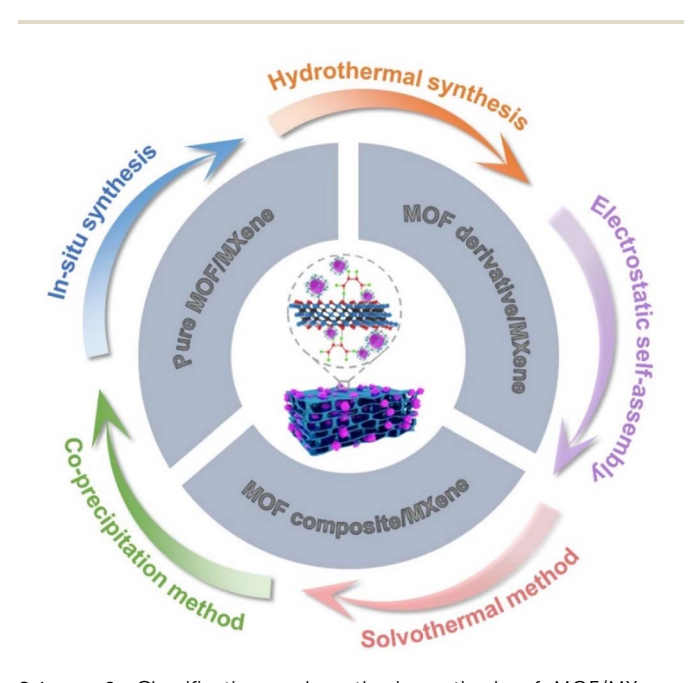
It is worth noting that the diversity of MOF components (including pure MOF, MOF composite and MOF derivative) in MOF/MXene-based materials has a decisive influence on the material properties. To our knowledge, there are currently no comprehensive reports on the component classification, synthesis strategies and multiple application potentials of MOF/MXene-based materials. Therefore, this review focuses on the classification of MOF/MXene-based materials, with emphasis on their preparation techniques and application fields. As shown in Scheme 1, MOF/MXene-based materials are systematically classified into three primary categories based on their MOF constituents: pure MOF/MXene, MOF composite/MXene, and MOF derivative/MXene. Their applications span

a wide range of fields, including batteries, SCs, sensors, catalysis, and absorption, among others. Furthermore, the future development trends and challenges that need to be addressed with MOF/MXene-based materials are also discussed.

2. Synthesis of MOF/MXene-based materials

MXene materials, featuring abundant surface functional groups and excellent electrical conductivity, are considered promising substrates for enhancing the stability and electrical conductivity of MOF materials.116-119 The integration of MOF and MXene is driven by interfacial interactions between the two components. The surface functional groups of MXene serve as active sites for the heterogeneous nucleation of MOF. Metal ions from the MOF precursor solution are attracted to the negatively charged oxygen-containing groups on the MXene surface via electrostatic interactions. This initial adsorption facilitates the coordination of organic ligands, initiating MOF growth directly on the MXene substrate. 65,120 Crucially, beyond physical interactions, strong chemical bonding often occurs at the interface, forming stable heterojunctions. Coordination bonds can form between the metal atoms (Ti) in the MXene layer and the donor atoms (O, N) from the organic ligands of MOF, such as Ti-O-C or Ti-N.113,121

This synergistic interaction has attracted significant research attention toward developing MOF/MXene-based materials through various synthetic strategies. These composites not only promote advancements in material design but also expand the application potential of MOF-based materials. As shown in Scheme 2, these composites are systematically classified into three main types based on their MOF constituents: pure MOF/MXene, MOF composites/MXene,



Scheme 2 Classification and synthesis methods of MOF/MXene-based materials.

and MOF derivatives/MXene. The primary synthesis methods for MOF/MXene-based materials encompass *in situ* synthesis, hydrothermal synthesis, electrostatic self-assembly, solvothermal method, and co-precipitation method. This section provides a comprehensive overview of the preparation of various MOF/MXene-based materials employing these different methods.

2.1. Pure MOF/MXene

Pure MOF/MXene composite materials are categorized into seven distinct categories according to the type of metal ions present in the MOF structure: (1) Fe-MOF/MXene, exemplified by Ti₃C₂T_x/MIL-53(Fe), ¹²⁶ synthesized via an in situ growth method; (2) Co-MOF/MXene, represented by Ti₃C₂-ZIF-67, ¹²⁷ fabricated through self-assembly; (3) Ni-MOF/MXene, such as Ni-MOF@Ti₃C₂T_x, 128 constructed using a solvothermal approach; (4) Cu-MOF/MXene, including Cu-MOF/MXene/ glassy carbon electrode (GCE),129 directly synthesized without intermediate steps; (5) Zn-MOF/MXene, typified by Zn-MOF-Ti₃C₂, ¹³⁰ prepared *via* a one-pot electrostatic self-assembly strategy in aqueous solution; (6) Zr-MOF/MXene, as demonstrated by MOF-801@MXene nanosheets,131 synthesized via an in situ strategy under ambient conditions; (7) bimetallic MOF/ MXene, such as CoNi-ZIF-67@Ti₃C₂T_x, 132 synthesized through coprecipitation process.

2.1.1. Fe-MOF/MXene. Liu et al. 126 fabricated a novel Ti₃C₂T_r/MIL-53(Fe) composite (TiCFe) through in situ integration of MIL-53(Fe) with layered Ti₃C₂T_x MXene. Initially, Ti₃AlC₂ MAX phase was selectively etched using hydrofluoric acid (HF) to generate accordion-like Ti₃C₂T_x nanosheets. The negatively charged surface of the exfoliated MXene facilitated the adsorption of metal ions, promoting their coordination with MIL-53(Fe). This synergistic interaction resulted in a hierarchical TiCFe architecture, which exhibited an enhanced specific surface area and abundant accessible active sites. Furthermore, a Fe-MOF/MXene hybrid material was developed by Xiao et al. 133 through a straightforward solvothermal approach, enabling the direct growth of Fe-MOF crystals on Ti₃C₂T_x MXene substrates. This composite retained the characteristic octahedral morphology of pristine Fe-MOF while significantly enhancing charge transfer efficiency through the incorporation of MXene. In the same year, Jia et al.134 designed a 2D hybrid electrode by utilizing $Mn_{n+1}X_nT_x$ as the electrode of the SCs, integrating electrochemically active sites from Fe-MOF (MIL-100(Fe)) to construct an interfacial columnar structure on the Ti₃C₂T_r MXene layer. Through chemical bond coupling, the Fe-MOF nanospheres and MXene nanosheets were transformed into a 3D multilayer porous nanostructure, which not only suppressed MXene aggregation but also preserved the laminar flow of reaction sites within the composite electrode. Similarly, Li et al. 135 synthesized butylimidazolium chloride (BIC)-modified MIL-101(Fe), denoted as BIC@MIL-101(Fe), by the solvothermal synthesis method. Subsequently, by employing vacuum-assisted self-assembly technology, they successfully prepared MXene-BIC@MIL-101(Fe) composite membrane exhibiting excellent structural stability, high mechanical RSC Advances Review

strength, and good separation performance. Recently, Wang *et al.*¹³⁶ fabricated a hydroxyl-rich MXene@MOF composite by the *in situ* growth of Fe-based MOF on MXene, inspired by the structure of bacterial cell walls, for the efficient isolation of lysozyme. In contrast, Han *et al.*¹³⁷ developed an innovative solar-driven evaporation system through synergistically integrating MXene with Fe-MOF@cellulose acetate/polyvinyl pyrrolidone. Their approach combined electrospinning and vacuum-assisted filtration to effectively couple the photothermal conversion properties of MXene with the enhanced hydraulic conductivity of electrospun cellulose acetate substrates. This design optimized both solar energy utilization and fluid transport, leading to significantly improved evaporation efficiency under solar irradiation. Meanwhile, Liu *et al.*¹³⁸

synthesized self-reporting molecularly imprinted polymers as internal reference probes and *in situ* grew Fe-MOF on MXene as signal nanoprobes, which were applied in a ratiometric electrochemical biosensor for rapid and effective detection of *Staphylococcus aureus*.

2.1.2. Co-MOF/MXene. In 2018, Ramachandran and colleagues fabricated a Co-MOF/Ti $_3$ C $_2$ T $_x$ composite directly on Ni foam (NF) through *in situ* hydrothermal deposition. Fig. 1a schematically illustrates the fabrication procedure for the Co-MOF/Ti $_3$ C $_2$ T $_x$ @NF composite. The porous structure of Co-MOF matrices, coupled with the high electrical conductivity of 2D Ti $_3$ C $_2$ T $_x$ nanosheets, synergistically enhances the availability of catalytic sites and facilitates efficient ionic diffusion. As illustrated in Fig. 1c and d, scanning electron microscopy (SEM)

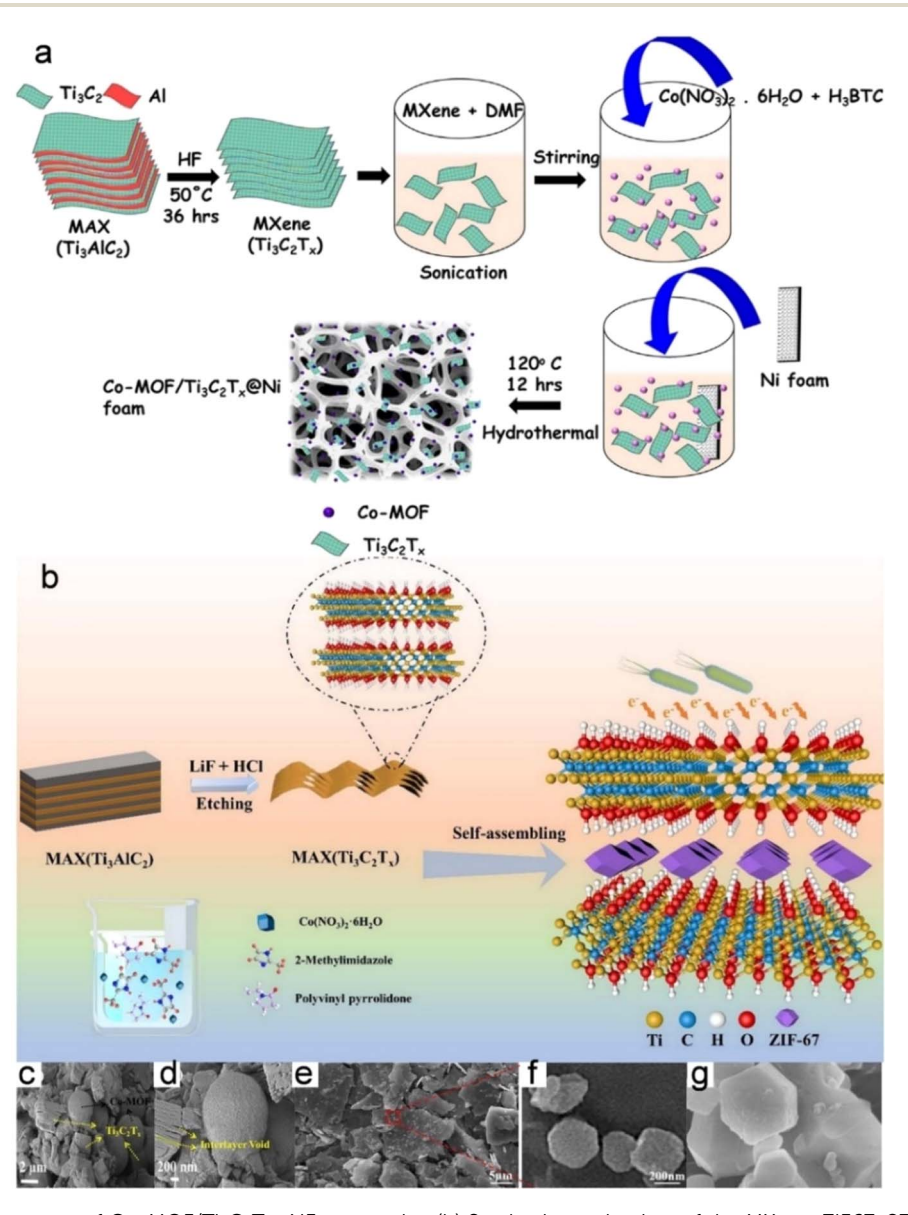


Fig. 1 (a) The synthesis process of Co-MOF/ $Ti_3C_2T_x$ @NF composite. (b) Synthesis mechanism of the MXene-ZIF67. SEM images of Co-MOF/ $Ti_3C_2T_x$ @NF (c and d), ZIF-67@MXene hybrid (e and f), and MXene-ZIF67 (g). (a, c and d) Reproduced with permission. Copyright 2018, Elsevier. (e and f) Reproduced with permission. Copyright 2022, Multidisciplinary Digital Publishing Institute. (b and g) Reproduced with permission. Copyright 2022, Elsevier.

analysis confirms the uniform coating and strong interfacial adhesion between the 2D Ti₃C₂T_x nansheets and Co-MOF on the NF substrate. 139 In 2021, Liang et al. utilized in situ growth to prepare ZIF-67@Ti₃C₂.¹⁴⁰ Transmission electron microscopy (TEM) images reveal the hybrid structure, with ZIF-67 particles, averaging approximately 800 nm in diameter, uniformly anchored on the surface of Ti₃C₂. Subsequently, Wan et al. developed an innovative ZIF-67 functionalized MXene composite using sequential precipitation synthesis. This hybrid material was subsequently integrated into thermoplastic polyurethane (TPU) matrices through melt compounding technology. The synthesis process involved dissolving 2.9 g (0.01 mol) of cobalt nitrate hexahydrate in 250 mL of methanol under continuous magnetic stirring for 10 min, followed by a 24 h aging period. Post-synthesis purification included sequential washing, vacuum filtration, and thermal drying at 80 °C for 24 h to obtain the final MXene/Co-ZIF composite. As illustrated in Fig. 1e and f, the resulting hybrid structure demonstrates unique interfacial features. MXene nanosheets with reactive surface groups (-O, -OH, and/or -F) facilitate effective chemical grafting, while ZIF-67 NPs provide abundant unsaturated cobalt coordination sites, promoting strong heterogeneous interfacial bonding. This mutual interaction promotes uniform dispersion of ZIF-67 crystallites across MXene lamellae, simultaneously achieving particle size refinement through surface confinement effects. The engineered TPU nanocomposites exhibited remarkable thermal performance enhancements, particularly demonstrating significant reduction in heat release rate

Concurrently, Yang et al. developed a "sandwich-like" Ti₃C₂-ZIF-67 composite through cubic-structured intercalation within MXene layer. Fig. 1b illustrates the fabrication process, in which MXene nanosheets were derived through selective HF etching of Al atoms from Ti₃AlC₂ precursors. The surface functional groups, which acquired negative charges during the etching process, facilitated the immobilization of ZIF-67 on the MXene substrate. Structural characterization, as evidenced by SEM image (Fig. 1g), confirmed the formation of ZIF-67 crystals, exhibiting a distinct crystalline morphology. The ZIF-67 NPs were uniformly modified on both sides of the MXene nanosheets. This composite material harnessed the combined advantages of its constituent components, namely, the hydrophilicity and conductivity of MXene and the biocompatibility of MOF. The composite exhibited exceptional colonization potential for microorganisms and maintained remarkable species diversity, while the synergistic interactions within the microbial consortium significantly improved bioelectricity production efficiency.¹²⁷ In addition to the above preparation strategies, there are some synthesis strategies about Ti₃C₂T_x/ ZIF-67 have been reported simultaneously. 142,143

alongside improved thermostability.141

In addition, Roy *et al.*¹⁴⁴ constructed a hierarchical Co-MOF-MXene@carbon black electrode architecture for electrochemical sensor electrodes and point-of-care testing chips by synthesizing MXene-supported Co-MOF-based nanocomposites and integrating them with carbon black ink through 3D printing technology. Ding *et al.*¹⁴⁵ adopted an interdiffusion reaction strategy to construct a 0D/2D heterostructure *via* self-

assembling Co-MOF onto highly conductive MXene nanosheets, enabling the design of highly reliable room-temperature gas sensing devices. In this architecture, the MXene nanosheets served as highly conductive core substrates, promoting efficient electron and mass transport while suppressing the agglomeration of MOF NPs during solution self-assembly. Concurrently, the Co-MOF functional sensing layer effectively separated the MXene nanosheets, mitigating their restacking and enhancing the overall thermodynamic stability of the composite.

2.1.3. Ni-MOF/MXene. Qin et al.146 utilized a straightforward self-assembly strategy to construct MXene QDs integrated with 2D Ni-MOF architectures in tunable ratios, thereby forming type II heterojunction structures. The composites demonstrated enhanced absorption and superior interfacial charge transfer ability, as evidenced by their optical and optoelectronic properties. The following year, Cheng et al. used layered Ti₃C₂ MXene as a catalyst and employed a facile electrostatic selfassembly process to synthesize 2D composites incorporating ultrathin Ni-MOF nanosheets. The similar layered structure of Ti₃C₂ MXene and Ni-MOF facilitated the formation of a conductive intimate interface, thereby promoting charge transfer and accelerating the separation of photogenerated charge carriers (electrons and holes).147 Concurrently, Zhang and co-workers reported an innovative MXene-directed synthesis strategy for high-performance SCs using Ti₃C₂T_x MXene/Ni-based MOF composite.148 Simultaneously, Zhang et al. developed an advanced battery-type nickel phosphates-MXene electrode material that is highly suitable for SCs. This material effectively inhibited the aggregation of MXene nanosheets while maintaining a laminar flow structure within the electrode, thereby facilitating rapid ion migration. ¹⁴⁹ In 2022, Ganiyat Olatoye et al. resolved the challenge of low specific capacitance by depositing Ni-ZIF-67 onto MXene substrates. The researchers first synthesized Ni-ZIF-67 hybrid materials under a controlled temperature gradient (150-450 °C), followed by the fabrication of Ni-ZIF-67-200/K-Ar-MXene composites through modification of intercalated 2D MXene layers (K-Ar-MXene) serving as a structural scaffold. 150

In addition, to address the inherent limitations of MOF, such as poor conductivity, unsatisfactory stability, and easy aggregation, Zheng et al. successfully developed Ti₃C₂ MXenesupported pillared-layer MOF with enhanced cyclability (MXene@Ni-MOF). The hybrid material features a 3D architecture stabilized by Ni-N coordination networks, which confers exceptional structural integrity, as evidenced by sustained performance during cyclic testing. Furthermore, the immobilization of Ni-MOF nanosheets on the MXene substrate facilitates rapid charge transfer between the two components, effectively mitigating the intrinsic low conductivity of Ni-MOF and preventing nanosheet agglomeration (Fig. 2a and b).70 In Fig. 2c, Wan et al. successfully fabricated 3D flower-like Ni-MOFs on multiterminal lamellar MXene using a solvothermal approach and investigated its flame retardant properties in TPU.128 Concurrently, Yang and colleagues prepared Ni-MOF/V2CTx-MXene composites through precisely controlled thermal annealing, resulting in heterostructured materials with hierarchically porous nanorod architectures. This engineered

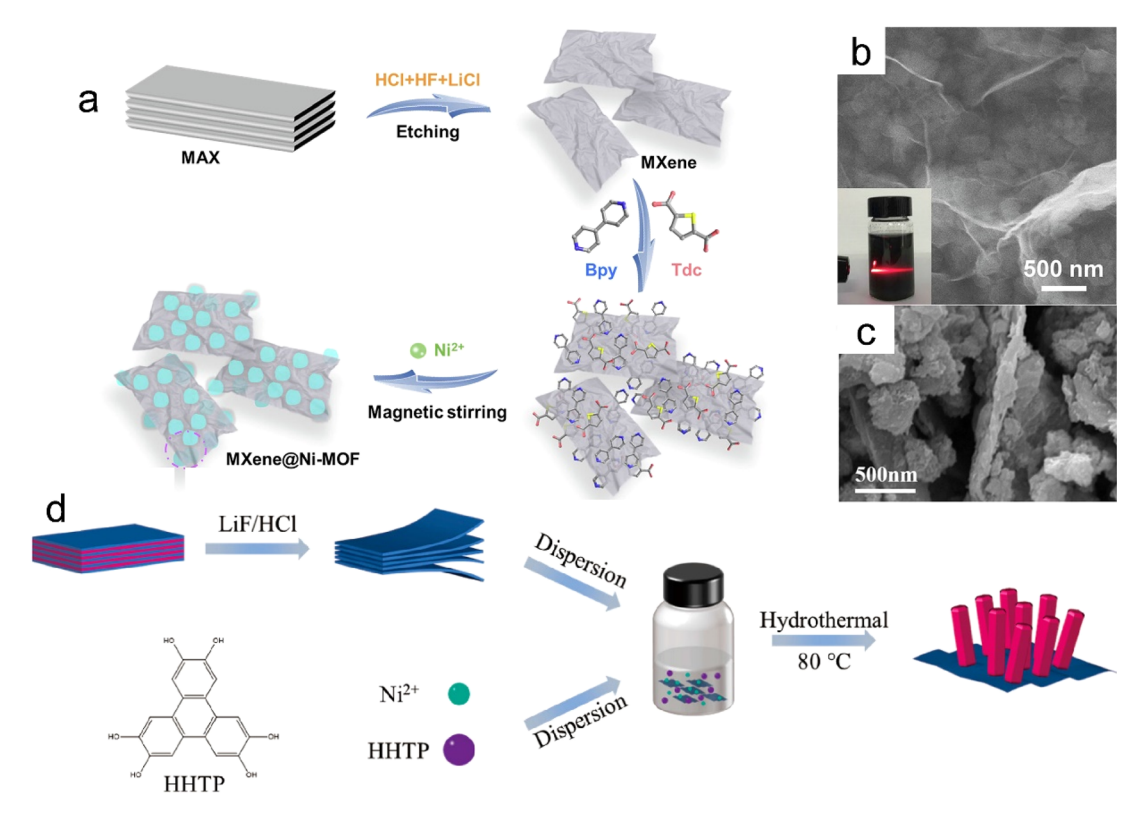


Fig. 2 (a) Schematic illustration of the synthetic process for MXene@Ni-MOF. (b) SEM and optical images of MXene@Ni-MOF. (c) SEM image for Ni-MOF@MXene hybrids. (d) Schematic diagram for the preparation of Ni-MOF/MXene. (a and b) Reproduced with permission.⁷⁰ Copyright 2022, Elsevier. (c) Reproduced with permission.¹²⁸ Copyright 2022, Elsevier. (d) Reproduced with permission.¹⁵² Copyright 2023, Multidisciplinary Digital Publishing Institute.

composite demonstrated significant improvements in both charge transport efficiency and electrochemically active surface characteristics. ¹⁵¹ In 2023, Li *et al.* leveraged the conductive properties of Ni-MOF and the high strength of ${\rm Ti_3C_2T_x}$ to enhance the stability of Ni-MOF. The prepared an innovative hybrid material featuring vertically aligned Ni-MOF nanorods on MXene substrates *via* controlled hydrothermal synthesis (Fig. 2d). ¹⁵² Additionally, Nanda *et al.* introduced a nickel-containing MXene composite with a nanosheet morphology, synthesized *via* solvothermal treatment in an autoclave. The resulting material demonstrated a high specific energy capacity and improved power delivery characteristics. ¹⁵³

The composite of highly conductive MXene and porous conductive MOF (Ni $_3$ (HITP) $_2$, HITP = 2,3,6,7,10,11-hexaminotriphenylene) has also been widely reported, Lin *et al.*¹⁵⁴ fabricated electrophysiological Ni $_3$ (HITP) $_2$ MOF/MXene electrodes. Xu *et al.*¹⁵⁵ fabricated a temperature sensor with high thermal sensitivity and excellent flexibility by loading conductive Ni $_3$ (HHTP) $_2$ MOF (HHTP = 2,3,6,7,10,11-hexahydroxytriphenylene) onto MXene *via in situ* polymerization. Moreover, the electrochemical performance of MXene was significantly improved by compounding it with Ni-HHTP¹⁵⁶ and (Fe-, Cu-, Co-, Ni)-1,3,5-benzene tricarboxylate (BTC) MOFs, ¹⁵⁷ which showed excellent performance for SCs. Shivade *et al.* used an innovative strategy to synthesize Ni-MOF/MXene composites

assisted by biomolecule folic acid, which effectively prevented the oxidation and restacking of MXene.¹⁵⁸

2.1.4. Cu-MOF/MXene. In 2021, a novel 3D flower-like Cu-MOF combined with ultrathin MXene nanosheets was synthesized and studied by Cheng et al. 129 The Cu-MOF was synthesized via a straightforward, one-step process utilizing copper nitrate and 2-aminoterephthalic acid as the starting materials (Fig. 3a-c). Subsequent progress in MOF engineering was demonstrated by Gu et al. through strategic modification of the conventional HKUST-1 framework. Their methodology involved the incorporation of 2D Ti₃C₂T_x MXene components, resulting in a novel composite material exhibiting enhanced structural integrity under hydrothermal conditions (Fig. 3d). Hassan et al.160 prevented the restacking of MXene sheets by integrating them with Cu-BTC MOF, thereby improving the electrochemical performance. However, Liu et al.161 adopted an innovative approach combining thermal induction with solvent-assisted oxygen anion etching, enabling precise modulation of pores in rigid microporous Cu-based MOFs. These engineered MOFs were subsequently assembled with MXenederived aerogels through self-assembly to construct flexible NO2 sensing platforms. Sharma et al. 162 designed MXene@Cu-TCPP (TCPP = tetrakis (4-carboxyphenyl) porphyrin) hybrid architectures that formed 2D heterogeneous nanostructures by van der Waals forces, exhibiting excellent stability and conductivity. Zhu et al.163 constructed a dimensional-matched

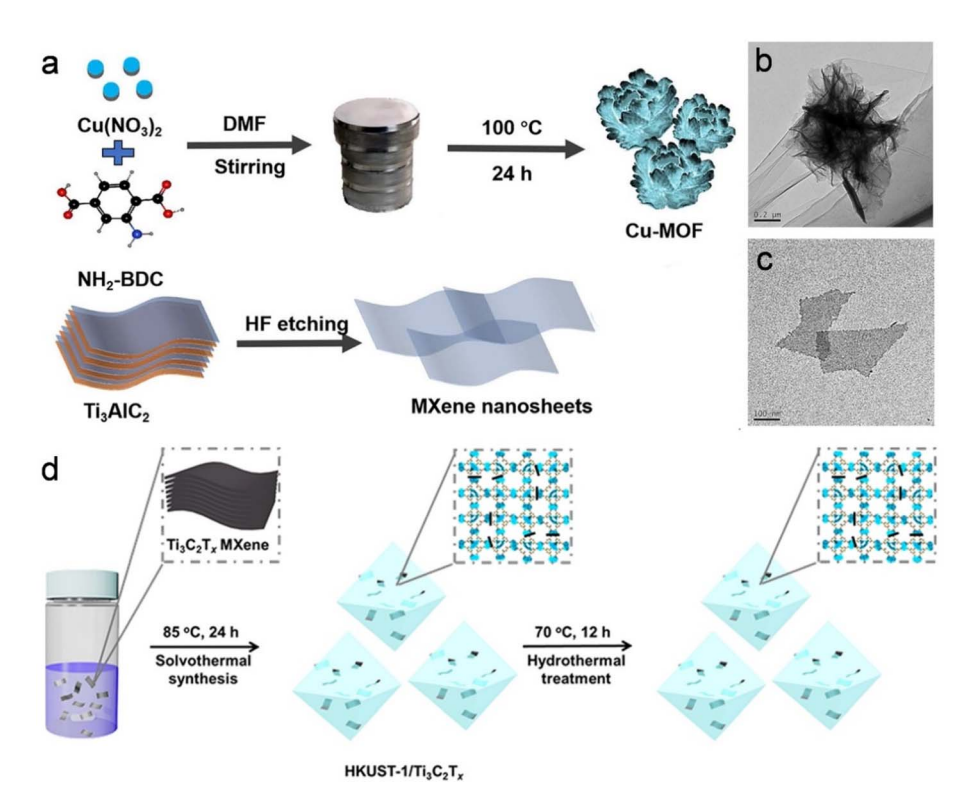


Fig. 3 (a) Preparation of Cu-MOF and MXene nanosheets. TEM images of Cu-MOF (b) and MXene (c). (d) Schematic diagram for the synthesis of HKUST-1/ $Ti_3C_2T_x$ MXene hybrid materials. (a–c) Reproduced with permission. Copyright 2021, Wiley. (d) Reproduced with permission. Copyright 2021, American Chemical Society.

organic-inorganic nanohybrid with high light absorption capacity and strong interfacial attraction by combining MXene/ TiO2 with a small amount of Cu-TCPP through a one-step solvothermal method. In addition, Lin et al. 164 reported a novel MXene/Cu-TCPP lamellar membrane that achieved efficient pervaporation energy generation by synergistically combining 2D MXene and Cu-TCPP MOF. Wang et al. 165 constructed MXene@MOF-based electrochemical biosensors via heterogeneous interface design: the TCPP organic ligand was first employed to functionalize MXene nanosheets, followed by surfactant-assisted solvothermal synthesis of MOF, yielding a MXene@MOF architecture with superior stability, enhanced conductivity, and a multilayered folded morphology. This architecture significantly increased electrochemical active sites, enabling label-free, ultrasensitive detection of glycoprotein nonmetastatic melanoma protein B in serum samples from patients with Parkinson's disease.

Recently, Zhou *et al.*¹⁶⁶ drew inspiration from the 3D interlocking hierarchical structure of the skin to construct a multifunctional artificial epidermal device through *in situ* growth of Cu₃(HHTP)₂ NPs on the surface of hollow spherical MXene, resulting in a biomimetic MXene@Cu₃(HHTP)₂ composite sensor. In this design, the gas-sensitive Cu₃(HHTP)₂ is heterogeneously assembled *in situ* at the MXene interface, mimicking the hollow spherical morphology found in skin, thereby structurally emulating the stratum spinosum and stratum granulosum of the epidermis. However, Ge *et al.*¹⁶⁷ proposed an all-solution process method to fabricate a photodetector by

sequentially spraying conductive $Cu_3(HHTP)_2$ and MXene onto a Si substrate, forming a van der Waals double heterojunction. The heterojunction structure promotes unidirectional electron hole separation with type I band alignment within the $Cu_3(HHTP)_2/Si$ interface, while it also takes advantage of the potential barrier difference between the $Cu_3(HHTP)_2/Si$ and $MXene/Cu_3(HHTP)_2$ Schottky junctions. The $MXene/Cu_3(HHTP)_2/Si$ photodetector exhibits excellent photoelectric properties.

2.1.5. Zn-MOF/MXene. In 2020, Li et al. employed a gentle water freezing-and-thawing approach to exfoliate multilayer MXene, followed by the integration of ZIF-8 NPs into the MXene layers through a straightforward layer-by-layer assembly strategy. The MXene/ZIF-8 composite exhibits unique architectural characteristics, featuring flexible MXene nanosheets with surface corrugations that serve as effective nucleation sites for the controlled growth of ZIF-8. This methodology provides an efficient solution to the persistent challenge of MXene layer restacking commonly encountered in conventional synthesis methods.168 Concurrently, Yao and co-workers utilized the MXene/ZIF-8 nanocomposite as an electrode material through an in situ growth method. 169 At almost the same time, Wang and co-workers prepared MXene/ZIF-8 nanocomposites by mixing the Zn(NO₃)₂·6H₂O solution with the 2-methylimidazole solution, followed by stirring for approximately 24 h, and subsequent centrifugation, washing, and drying steps. 170 Rabiee et al. constructed an innovative inorganic MXene/MOF-5 nanostructure using a vacuum-assisted filtration process.171 In 2022,

RSC Advances Review

Guo et al. successfully synthesized a bioactive Zn-MOF over the Ti₃C₂T_x nanosheets through in situ growth. The fabrication pathway of the Zn-MOF@Ti₃C₂T_x composite is schematically depicted in Fig. 4a. Expanding on earlier work, Yao et al. systematically investigated ZIF-8@Ti₃C₂T_r hybrid materials through an optimized single-step microemulsion synthesis. 173 The experimental scheme involved the gradual incorporation of microemulsion phases A and B into Ti₃C₂T_r suspensions, followed by vigorous stirring under ambient conditions. The product was then isolated via centrifugation, purified through repeated methanol washes, and finally dehydrated under vacuum at 60 °C. More recently, Jose Paul et al. synthesized $[Zn_4(1,2,4,5-benzene-tetra carboxylate)_2(H_2O)_6]_n \cdot 3nH_2O$ MOF using pyromellitic acid-based linkers and Zn(NO₃)₂·6H₂O as precursors via a reticular synthesis approach. Multilayer MXene was prepared through conventional HF etching, and the MOF-MXene hybrid composite was subsequently constructed through the one-step electrostatic self-assembly process in aqueous medium. As demonstrated in Fig. 4b, this integration process successfully occurred under ambient conditions within distilled water through reticular synthesis principles. SEM and TEM images of the MOF-MXene microstructure (Fig. 4c-e) indicate that the MOF envelops MXene with a casually oriented, block-structured configuration.¹³⁰ Deng et al. developed polyurethane (PU)-MXene-MOF sponge using an in situ growth technique.174 As shown in Fig. 4f and g, the ZIF-8 NPs were

uniformly dispersed on the surface of the PU-MXene sponge, resulting in a significantly roughened surface morphology of the PU-MXene-MOF sponge skeleton. Building upon previous research, Hao *et al.* successfully synthesized MXene@ZIF-8 to a mitigate the inherently low electrical conductivity of MOF.¹⁷⁵ In addition, Shahriyari Far and co-workers fabricated MXOF composites *via* solvothermal growth, demonstrating the synergistic effect between Zn-MOF and MXene nanosheets.¹⁷⁶

2.1.6. Zr-MOF/MXene. Li et al. 131 constructed a significantly improved MOF@MXene membrane for gas separation by a room temperature in situ synthesis strategy. Initially, the negatively charged MXene nanosheets immobilized adjacent Zr metal ions through electrostatic interactions. Subsequently, under ambient conditions, these metal ions coordinated with organic ligands, promoting the homogeneous nucleation and growth of MOF-801 crystalline structures on the MXene surfaces, thereby yielding MOF-801@MXene nanosheets. The as-prepared nanocomposites were then uniformly deposited onto a porous organic support via vacuum-assisted filtration, ultimately forming the MOF@MXene composite membrane. Wen et al.177 synthesized the 3D hierarchical Zr-MOF/Ti₃C₂T_x nanocomposite through a facile method that involved electrostatic interaction between the Ti₃C₂T_x MXene nanosheet and Zr⁴⁺, followed by the solvothermal method for the *in situ* synthesis of Zr-MOF on the Ti₃C₂T_x nanosheets. In addition, Kashif et al. 178 fabricated UiO-66/MXene hybrids via

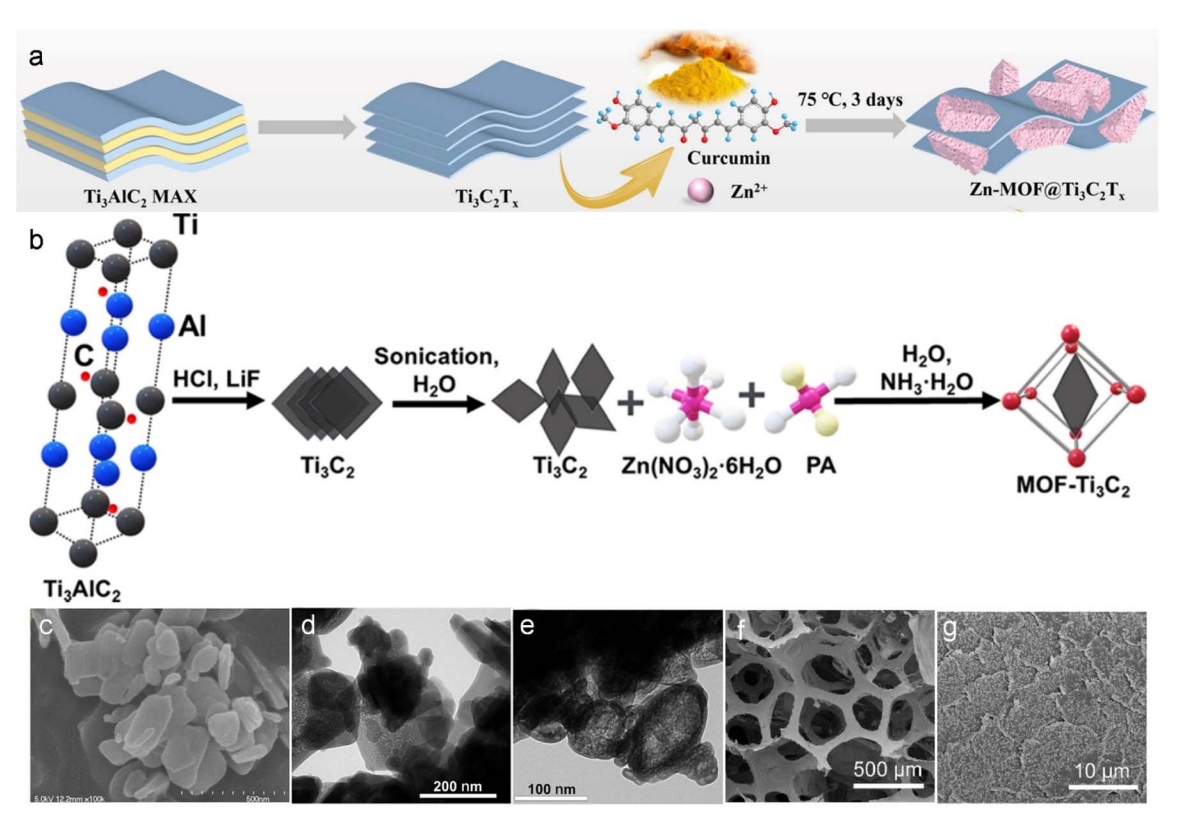


Fig. 4 (a) Schematic diagram for the preparation of Zn-MOF@MXene hybrid. (b) Schematic illustration of the synthetic process for MOF-MXene composite. (c) SEM image of MOF-MXene. (d and e) TEM images of MOF-MXene. (f and g) SEM images of PU-MXene-MOF sponge. (a) Reproduced with permission. Copyright 2023, Elsevier. (f and g) Reproduced with permission. Copyright 2023, Elsevier. (f and g) Reproduced with permission. Copyright 2023, Elsevier.

the atomic force microscope (AFM) characterization of $\text{Co}_2\text{Ni-MOF}$ $\oplus \text{Ti}_3\text{C}_2\text{T}_x$ reveals a uniform thickness distribution, in contrast to its individual components ($\text{Co}_2\text{Ni-MOF}$ and $\text{Ti}_3\text{C}_2\text{T}_x$). Beyond these strategies, recent studies $^{188-191}$ have reported analogous *in situ* growth methods for fabricating MXenesupported bimetallic NiCo-MOF composites.

In addition to the above-mentioned NiCo-MOF/MXene, other bimetallic MOF/MXene composite materials such as VCo-MOF/ MXene, FeCu-MOF/MXene, FeNi-MOF/MXene, FeCo-MOF/ MXene, CuZn-MOF/MXene and NiMn-MOF/MXene have also been reported. Li and co-workers synthesized a composite catalyst by in situ growth of VCo-MOF on the surface of MXene using a solvothermal method. 192 Furthermore, M. Adil and coworkers synthesized the FeCu MOF/MXene composite via in situ hydrothermal growth on NF to form a binder-free electrode. 193 A hybrid electrocatalyst, FeNi-MOF@MXene, composed of Fe, Ni-based MOF (FeNi-BTC MOF) and MXene, was prepared via a solvothermal reaction. 194 Meanwhile, Thai et al. 195 developed a novel bimetallic FeCo-MOF composite (MIL-100@ZIF-67) supported on MXene nanosheets, resulting in the hybrid material MIL-100@ZIF-67@MXene. To optimize the ion transport pathway and improve the ion permeability, Li et al. 196 used block copolymers to generate mesopores within 2D MOF nanosheets, thereby constructing hierarchically porous Cu-Zn-MOF@MXene hybrids. In addition, both Ali et al. 197 and Siva Shalini et al. 198 synthesized NiMn-MOF nanocomposites through a hydrothermal method, and similarly achieved MXene incorporation into NiMn-MOF to improve electrochemical performance through the same synthetic route.

2.1.8. Others. As mentioned above, a variety of single-metal (Fe, Co, Ni, Cu, Zn, and Zr) and bimetallic (NiCo, VCo, FeCo, FeNi, FeCu, ZnCu, and NiMn) MOF-based materials have been reported for the construction of composites with MXene. In addition to these, several other representative MOF/MXenebased materials incorporating Bi-, Ce-, Al-, Ti-, La-, and Mobased MOF have also been recently developed. For example, Gong et al. fabricated leaf-like MXene-based flame retardants (MXene@Bi-MOF) through the in situ growth of shuttle-shaped Bi-MOF on the surface of MXene. 199 Chen et al. successfully prepared a novel Ce-MOF/MXene composite via employing the 3D straw-sheaf-like Ce-MOF and MXene nanosheets.200 Meanwhile, Li et al.201 prepared MXene@Ce-MOF composites featuring abundant oxygen vacancies. Zhang et al.202 synthesized MXene@MOF-303(Al) composites through in situ growth of MOF-303(Al) on MXene, effectively combining the advantageous properties of both components. Subsequently, a composite membrane composed of MXene@MOF-303(Al), polyvinyl alcohol, and polyacrylonitrile was prepared using the composite as a filler and a polyacrylonitrile ultrafiltration membrane as substrate. In addition, Li et al. 203 utilized MXene as a Ti source to synthesize layered Ti-MOF nanosheets via organic ligand coordination, followed by strategic integration of mesopores to create multiscale porous MXene-MOF composites with superior charge storage characteristics. Zhao et al.204 achieved in situ synthesis of a Ti-based MOF (NH2-MIL-125) using 2aminoterephthalic acid and tetrabutyl titanate, concurrently hybridizing it with MXene to form a Ti-MOF@MXene composite

solvothermal method. UiO-66 and MXene were heat treated in solvent to make them closely combined to form composite materials. Xiang et al.179 prepared a polyethylene glycol/ MXene@MOF membrane with stable interlayer spacing and excellent antifouling performance by a simple interface selfassembly strategy. In this approach, UiO-66-NH2 MOF NPs were used as structural supports to induce intercalation within layered MXene nanosheets, effectively tuning the interlayer spacing and enhancing the permeability. Subsequently, hydrophilic polyethylene glycol was introduced through hydrogen bonding, further stabilizing the intercalated architecture. However, Maleki et al. 180 focused on the preparation of a novel MXene modified polyether sulfone membrane. By compounding UiO-66-NH2 NPs with MXene, UiO-66-NH2@MXene 2D nanocomposites were created to modify polyethersulfone membrane. During the membrane modification process, 0.25 wt% UiO-66-NH₂@MXene nanocomposite was used as modifier to successfully synthesize the modified MXene based polyethersulfone membrane. Recently, Meng et al. 181 employed electrostatic self-assembly to rationally integrate NH2-UiO-66 with MXene nanosheets, resulting in an innovative hybrid material. This process involved the solution-phase mixing of oppositely charged Zr-MOF and MXene components, which spontaneously assembled into an ordered multilayer structure driven by electrostatic interactions.

2.1.7. Bimetallic MOF/MXene. In 2019, Wen et al. 132 synthesized CoNi-ZIF-67@Ti₃C₂T_x by in situ coprecipitation growth of bimetallic CoNi-ZIF-67 rhombic dodecahedrons on Ti₃C₂T_x. The resulting hybrid structure is clearly depicted in the SEM image (Fig. 5a), where the layered structure of $Ti_3C_2T_x$ is well preserved, with uniformly dispersed CoNi-ZIF-67 particles embedded within the interlayer spaces. For comparison, SEM analysis (Fig. 5b) of pristine CoNi-ZIF-67 highlights its distinct morphological features in the absence of Ti₃C₂T_x support. Liu et al. 182 engineered 3D MXene/NiCo-MOF composite films by integrating 2D nanosheets with NiCo-MOF nanoflakes through hydrogen bonds, employing vacuum-assisted filtration. This approach initiated with the synthesis of 2D NiCo-MOF nanosheets under ambient conditions, followed by multilayered MXene production through HF etching of Ti₃AlC₂ and subsequent alkalization (Fig. 5f). In 2021, Du et al.183 obtained Ti₃C₂T_x/CoNi-MOF nanosheets by in situ growth process. Additionally, Wu and co-workers developed the 1D heterostructure via integrating MXene fibers with CoNi-MOF. 184 In recent years, Xiao et al. demonstrated a novel 2D heterostructure synthesized by vertically growing NiCo-MOF ultrathin nanosheets on exfoliated Ti₃C₂T_x MXene substrates. This architecture effectively integrates the synergistic merits of conductive MXene with the enhanced electrochemical properties inherent to bimetallic MOF nanomaterials. 185 The superior electrical conductivity and effective interfacial compatibility of aminated MXene with electrolytes enables homogeneous in situ anchoring of bimetallic NiCo-MOF on its surface. Yue et al. successfully prepared highly redox-active NiCo-MOF that were in situ stabilized using 2D aminated Ti₃C₂T_x. 186 Recently, Tan et al. 187 fabricated multiple 2D MOF/Ti₃C₂T_x hybrid materials through electrostatically directed assembly (Fig. 5g). As illustrated in Fig. 5c-e,

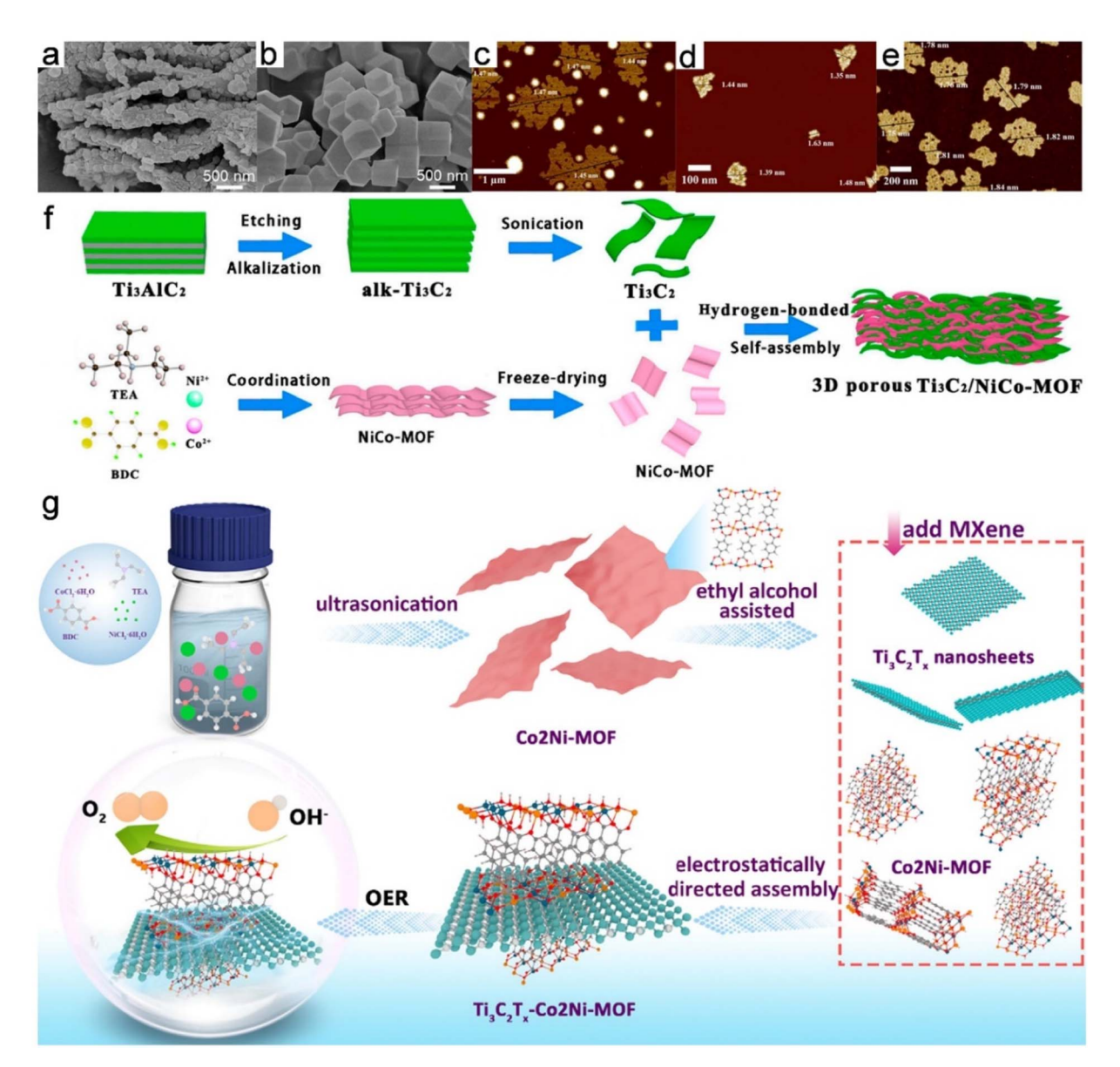


Fig. 5 SEM images of CoNi-ZIF-67@ $T_{13}C_{2}T_{x}$ (a) and pure CoNi-ZIF-67 (b). AFM images of Co₂Ni-MOF (c), $T_{13}C_{2}T_{x}$ (d), and $Co_{2}Ni$ -MOF@ $T_{13}C_{2}T_{x}$ (e). (f) Fabrication process of MXene/NiCo-MOF. (g) A scheme for the preparation of MXene/NiCo-MOF. (a and b) Reproduced with permission. Copyright 2019, Molecular Diversity Preservation International. (c-e and g) Reproduced with permission. Copyright 2022, Elsevier. (f) Reproduced with permission. Copyright 2020, Molecular Diversity Preservation International.

material, which was further functionalized with polyethyleneimine and covalently connected immobilized onto a gold electrode to construct a sensing platform. Yu *et al.*²⁰⁵ developed lanthanide-based La-MOF on MXene nanosheets *via* an *in situ* growth strategy, producing La-MOF@MXene hybrid flame retardants. In addition, Lin *et al.*²⁰⁶ proposed an interface engineering strategy to construct defect-engineered La-MOF@MXene nanohybrids with oxygen vacancies by synergistic defect and *in situ* growth. Kaur *et al.*²⁰⁷ fabricated a composite by combining Mo-MOF with MXene (NH₂-Mo-MOF/MXene), which was subsequently deposited onto screenprinted electrodes.

To address structural limitations inherent in conventional MOF synthesis, Wang *et al.*²⁰⁸ proposed an innovative metal-ion-

assisted conversion methodology employing 2D MXene as a precursors. This method enabled the successful fabrication of 3D catechol-functionalized TiCu-HHTP MOFs with a non-interpenetrated $SrSi_2$ architecture. The transformation mechanism involves three synergistic processes: (1) electron transfer from MXene substrates to adsorbed Cu^{2+} , initiating oxidation-reduction reactions, (2) cleavage of Ti–C bonds releasing Ti^{4+} ions, and (3) subsequent coordination of Ti^{4+}/Cu^{2+} with the HHTP ligand to form a stable MOF structure. Notably, this approach exhibits remarkable versatility, V_2CT_x can substitute conventional MXene precursors, and various M^{n+} (Ni^{2+} , Co^{2+} , Mn^{2+} , and Zn^{2+}) can effectively replace the original metal ions, highlighting the broad adaptability of the methodology.

2.1.9 Summary. The synthesis of pure MOF/MXene composites, as detailed in the previous sections, relies on a variety of strategies, among which the selection of metal ions plays a crucial role in determining the best approach and the properties of the composites. A critical comparison reveals the different patterns in the synthesis approaches employed for different metal ions.

- (1) *In situ* growth is the most versatile method, successfully applied for Fe-MOF/MXene (*e.g.*, ${\rm Ti_3C_2T_x/MIL\text{-}53(Fe)^{126}}$), Zr-MOF/MXene (*e.g.*, MOF-801@MXene¹³¹), Zn-MOF/MXene (*e.g.*, ZIF-8@Ti₃C₂T_x¹⁷³), and bimetallic MOF/MXene (*e.g.*, CoNi-ZIF-67@Ti₃C₂T_x¹³²). This method generally promotes strong interfacial interaction and good dispersion of MOF on the MXene surface, making it a robust choice for achieving intimate contact.
- (2) Solvothermal and hydrothermal methods are frequently used for Co-MOF/MXene (e.g., Co-MOF/Ti $_3$ C $_2$ T $_x$ @NF 139) and Ni-MOF/MXene (e.g., Ni-ZIF-67/MXene 150). These techniques offer good control over crystal morphology but require high temperatures, which can be detrimental to the stability of MXene if the temperature cannot be precisely controlled.
- (3) Self-assembly strategies, including electrostatic self-assembly and vacuum-assisted filtration, are effective for Zn-MOF/MXene (e.g., Zn-MOF-Ti $_3$ C $_2$ T $_x$ via one-pot strategy 130), Ni-MOF/MXene (e.g., MXene QDs coupled with 2D Ni-MOF 146), and Cu-MOF/MXene (e.g., Cu-BTC MOF/MXene 160). These methods usually carried out under mild conditions, which is beneficial for preserving the integrity of MXene and is particularly suitable for creating layered or membranous structures.
- (4) Coprecipitation is a straightforward method used for the synthesis of bimetallic MOF/MXene composites, such as CoNi-ZIF-67@ ${\rm Ti}_3{\rm C}_2{\rm T}_x$, offering a rapid route to bimetallic integration.

In conclusion, while *in situ* growth emerges as the most widely adopted and effective strategy for achieving strong interfacial bonding across various metal ions, the selection of a synthesis method must be carefully tailored to the specific MOF and the desired composite morphology. The diversity of approaches highlighted in this section underscores the flexibility in designing pure MOF/MXene materials, with each method offering a unique balance of interfacial strength, morphological control, and compatibility with the MXene substrate.

2.2. MOF composite/MXene

In recent years, significant research efforts have been devoted to the fabrication of MOF composite/MXene-based materials. These MOF composites typically involve the integration of MOF materials with various functional components, including metal NPs, metal oxides, carbon-based materials, organic compounds, metal hydroxides, and other materials.

With respect to MOF@metal NPs/MXene composites, Dai and co-workers²⁰⁹ successfully synthesized Zr-Fc MOF/AuNPs/4-mercaptophenylboronic acid (4-MPBA) nanocomposites, which were subsequently integrated with 2D ${\rm Ti}_3{\rm C}_2{\rm T}_x$ MXene. Huang $et~al.^{210}~$ introduced a bottom-up synthesis of porous

heterostructure substrates by stepwise solvothermal reactions with Zn-based MOFs and MXene nanosheets, and spatially constructed stable ultrafine Pt nanocrystals on them (Pt/ZIF-Ti₃C₂T_x). In addition, Wen et al.²¹¹ developed a hierarchical assembly approach involving the direct in situ growth of porous ZIF-8 nanocrystals on multilayer MXene substrates, followed by the precise immobilization of abundant Pt NPs on the MXene@ZIF-8 hybrid substrate. The resulting MXene@ZIF-8@Pt NPs composite material demonstrates enhanced electrochemical durability and catalytic efficiency, attributed to the complementary characteristics of its constituent materials: the conductive MXene framework, surface-enhanced ZIF-8 matrix, and catalytically active Pt nanostructures. Recently, Zhang et al.212 successfully prepared a Ru-doped Co-MOF@MXene composite catalyst with high conductivity and high catalytic activity, achieved by modulating the electronic structure of Copyridinedicarboxylic MOF through Ru doping and room temperature hybridization with MXene nanosheets.

The development of MOF@metal oxide/MXene composites has also advanced significantly. Lu et al.213 successfully fabricated an innovative Fe₃O₄@MXene@MOF-74 composite through a straightforward synthesis strategy. Structural characterization revealed the formation of well-defined crystalline NPs after Fe₃O₄ modification, with Fig. 6a illustrating the homogeneous magnetic integration across the MXene substrate. Elemental mapping analysis quantitatively verified the coexistence of Zn, Fe, C, Ti, and O, thereby verifying the compositional homogeneity and structural integrity of the composite. Liu et al. 120 reported a universal strategy for constructing 3D MXene/MOF composites. Through in situ growth via a coprecipitation reaction, a series of hollow 3D MXene/MOF composites (Ti₃C₂T_x/Cu-BTC, Ti₃C₂T_x/ZIF-8, Ti₃C₂T_x/ZIF-67, Ti₃C₂T_x/FeCo-PBA, and Ti₃C₂T_x/ZIF-67/CoV₂O) were successfully prepared (Fig. 6e). Furthermore, Chi et al.214 prepared a MXene@SnO2-Ce-MOF Z-scheme heterojunction with abundant oxygen vacancies as a photoactive material by hydrothermally combining the etched MXene with SnO2, and then combining it with Ce-MOF prepared by co-precipitation method.

Recently, MOF@carbon-based material/MXene composites have attracted considerable attention. Tu et al.215 synthesized a novel composite material through the integration of MXene with carbon nanohorns and β-cyclodextrin MOFs (MXene/ CNHs/β-CD-MOFs). The layered MXene component maintained its characteristic accordion-like configuration, while the CNHs preserved their quasi-spherical nanostructure. Fig. 6b demonstrates the successful encapsulation of MXene/CNHs assemblies within elongated β-CD-MOF crystalline matrices. Rana et al.216 employed a MOF-525@Ecoffex nanocomposite featuring a layer of Ecoffex@MXene@Co-nanoporous carbon (NPC) to construct stretchable and humidity-resistant multifunctional triboelectric nanogenerator (TENG). In this configuration, MOF-525 (Fig. 6c) served as the charge generation layer, while the Co-NPC@MXene nanocomposite (Fig. 6d) functioned as the conductive intermediate layer. However, Rajan et al.217 constructed a ternary heterojunction photocatalyst (Ni-MOF/ graphitized carbon nitride $(g-C_3N_4)/MXene)$

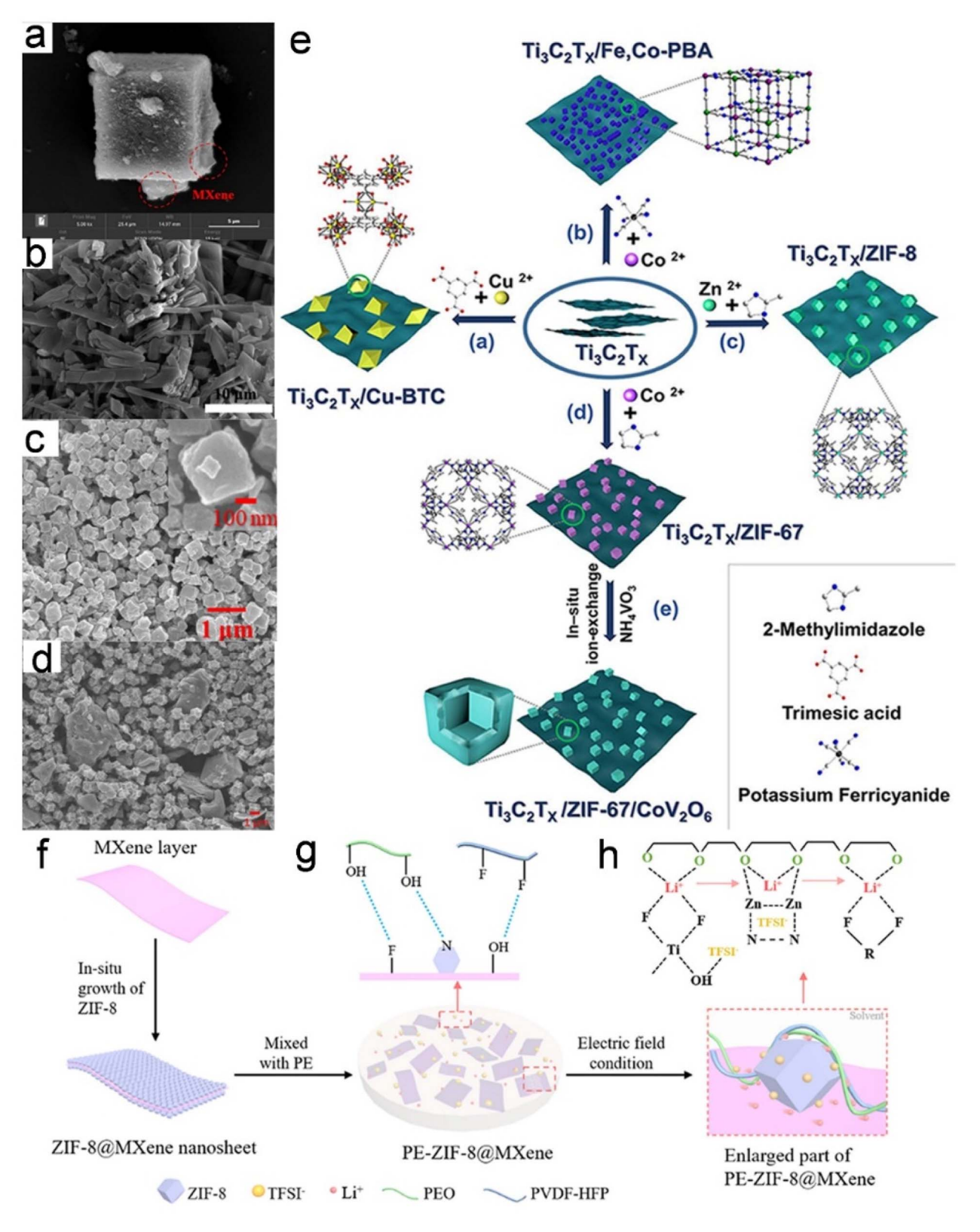


Fig. 6 SEM images of Fe₃O₄@MXene@MOF-74 (a), MXene/CNHs/β-CD-MOFs (b), MOF-525 (c), and MXene@Co-NPC (d). Synthesis procedure of 3D MXene/MOF (e), ZIF-8@MXene (f) and PE-ZIF-8@MXene (g). (h) Schematic illustration of the intermolecular interaction between ZIF-8@MXene, polymer molecules and lithium salt. (a) Reproduced with permission. Copyright 2022, Elsevier. (b) Reproduced with permission. Copyright 2020, Elsevier. (c and d) Reproduced with permission. Copyright 2022, Elsevier. (e) Reproduced with permission. Copyright 2022, Wiley. (f–h) Reproduced with permission. Elsevier.

integrated solvothermal synthesis and wet impregnation techniques. This innovative architecture combined Ni-MOF, g-C₃N₄, and MXene, establishing dual charge-transfer mechanisms through an engineered Type II heterojunction configuration coupled with a noble-metal-free Schottky interface. Subsequently, Qi et al. 218 engineered a Fe-MOF-NH2/CNT-NH2/MXene composite through electrostatic self-assembly, strategically combining positively charged amino-functionalized components (Fe-MOF-NH2 and CNT-NH2) with negatively charged MXene, and further prepared molecularly imprinted polymer modified resistive type electrochemical sensor using electropolymerization technology. In addition, Hassan et al.219 synthesized carbon aerogel induced chromium MOF (CA@MIL-101) with Ti₃C₂T_x MXene nanocomposite material (CA@MIL-101-(Cr)/Ti₃C₂T_r) by hydrothermal method, which had interconnected porous structure that provided abundant divalent ionic active sites and significantly enhanced charge transfer kinetics. Recently, Lin et al.220 prepared g-C3N4 nanosheets

using thermal polymerization and peeling method under air

conditions. Subsequently, MIL-101(Fe)/g-C₃N₄ composites were

constructed using hydrothermal method at 120 °C. Subse-

quently, MXene nanosheets were added, and MXene@MIL-

101(Fe)/g-C₃N₄ composite materials were prepared by sol-

vothermal method. The results showed that MIL-101(Fe)/g-C₃N₄

successfully deposited on the MXene nanosheets. Building upon advancements in MOF@carbon-based materials/MXene composites, investigators have extended their efforts to engineer MOF@organic compound/MXene composites, aiming to achieve richer functions and performance. Zhao and colleagues²²¹ engineered a polymer composite electrolyte reinforced with ZIF-8@MXene nanosheet (PE-ZIF-8@MXene) via an in situ growth process. Fig. 6f-h demonstrate the fabrication process for both ZIF-8@MXene and PE-ZIF-8@MXene, accompanied by molecular-level interaction schematics among the hybrid nanofillers, polymer matrix, and lithium salt components. Guo et al. 222 successfully synthesized ZIF-67@MXene/polyimide (PI) hybrid materials with ordered lamellar structures through thermal compression of 3D networked aerogels, where PI was synergistically integrated with MXene-supported ZIF-67 crystalline frameworks. This synthesis method took advantage of the compressibility of the aerogel, which kept the aerogel walls always parallel to the sliding direction and thus provided significant antifriction effect. In addition, Liang et al.223 employed a ternary mixed ligand system comprising Eu3+, 1,3,5-benzenetricarboxylic acid, and terephacid with polydopamine-functionalized MXene (PDA@MXene) to fabricate multilayered sandwich-structured Eu-MOF/PDA@MXene composites through an in situ assembly strategy. This synthesis method not only endowed the material with a multilayer porous structure but also realized the magnetic functionalization of the material by uniformly immobilizing Fe₃O₄ NPs in Eu-MOF/PDA@MXene through selfassembly. However, Hou et al.224 reported the successful synthesis of MXene@PDA/MOF composites with a unique honeycomb-like morphology, achieved by in situ coordination of 2-methylimidazole and Zn²⁺ on the surface of PDA-modified MXene. This synthesis method endowed the material with

extensive surface area and superior electrical conductivity, establishing fundamental advantages for electrochemical sensing applications. Recently, Zhu *et al.*²²⁵ successfully intercalated tannic acid (TA) etched ZIF-8 (TZIF-8) nanocrystals with hollow structures into the interlayer spacing of MXene, thus forming MXene/TZIF-8 membranes with high permeability and good separation effects on various oil-water emulsions. Moreover, Yang *et al.*²²⁶ reported a novel photocatalyst created through *in situ* growth and self-assembly, where MXene served as a support for ZIF-8 MOF immobilization. The MXene@ZIF-8 was further modified with TA and polyphenol compounds to form a cross-linked network that enhanced the heterogeneous interface, which is essential for efficient photocatalysis. The performance of the photocatalyst was optimized by exploring different concentrations of TA.

In addition to the previously described metal NPs, metal oxide, carbon-based materials, organic compound@MOF composites combined with MXene, Sun *et al.*²²⁷ adopted a novel kirkendall effect assisted electrostatic self-assembly method to construct a MOF (MIL-88A) substrate surface decorated with Ni–Fe layered double hydroxide (LDH) and formed multilayer nanocages, which were coated with MXene on the outer surface of the nanocage. By adjusting the adsorption of MXene on the LDH surface, the heterogeneous interface in the MOF-LDH-MXene ternary composite exhibited excellent interfacial polarization loss. Recently, hybrid systems incorporating MnCO₃@-MOF,²²⁸ polydimethylsiloxane-MOF@Ag,²²⁹ and the reduced graphene oxide (rGO)/PDA/FeCu-MOF²³⁰ composites with MXene have also been investigated.

The synthesis of MOF composite/MXene materials, as detailed in the preceding sections, is characterized by a remarkable diversity in both the composition of the MOF composite and the strategies used to integrate it with MXene. A critical analysis reveals that the choice of synthesis method often depends on the properties of the MOF composite and the desired final architecture.

- (1) *In situ* growth is a powerful strategy for constructing multi-layered or core–shell architectures. This approach was used to prepare $Pt/ZIF-Ti_3C_2T_x$ by sequentially growing ZIF-67 on MXene and then depositing Pt nanocrystals,²¹⁰ and to construct the hierarchical MXene@ZIF-8@Pt NPs composite.²¹¹ This method allows for precise, step-by-step engineering of complex heterostructures with strong interfacial contact.
- (2) Solvothermal and hydrothermal methods are particularly effective for the synthesis of MOF@metal oxide/MXene and MOF@carbon-based material/MXene composites. The synthesis of Fe₃O₄@MXene@MOF-74 (ref. 213) and the MXene@SnO₂-Ce-MOF Z-scheme heterojunction²¹⁴ relied on these techniques. Similarly, the integration of MXene with preformed MIL-101(Fe)/g-C₃N₄ composites was achieved *via* a solvothermal process.²²⁰ These methods are highly suitable for reactions that require controlled temperature and pressure to form crystalline composites.
- (3) Self-assembly strategies, including electrostatic self-assembly, vacuum-assisted filtration, and thermal compression, are highly versatile for creating layered, membrane-like, or 3D aerogel-based composites. This approach was used to

RSC Advances Review

synthesize MOF-525@Ecoffex nanocomposites with a MXene@Co-NPC hybrid,216 to construct ZIF-67@MXene/PI hybrid materials via thermal compression of aerogels,222 and to fabricate MXene/TZIF-8 membranes with high permeability.²²⁵ The self-assembly of MOF@organic compound/MXene composites is also common, as demonstrated by the electrostatic selfassembly of Fe-MOF-NH2/CNT-NH2/MXene218 and the in situ growth of ZIF-8@MXene for polymer electrolytes.221 These methods are often conducted under mild conditions, preserving the integrity of MXene.

(4) Coprecipitation is a direct and scalable method for the in situ formation of MOF composites on MXene, as demonstrated by the universal strategy for fabricating hollow 3D MXene/MOF composites.120

In conclusion, the synthesis of MOF composite/MXene materials is highly flexible, with the choice of method enabling the design of a wide range of morphologies and architectures. In situ growth excels in building complex, multicomponent systems, solvothermal/hydrothermal methods are ideal for crystalline composite integration, and self-assembly offers a powerful route to layered and functionalized materials.

2.3. MOF derivative/MXene

MOF derivatives, which exhibit high specific surface area and porosity, structural flexibility, tunable functionality, and excellent chemical stability, have been effectively integrated with MXene, known for its ultra-thin nature, robust mechanical toughness, and superior electrical conductivity. This synergistic combination has garnered significant attention from research groups worldwide. Several successful syntheses of MOF derivative/MXene composites are documented herein, categorized into seven distinct groups based on the variations in MOF derivatives: (1) MOF-derived metal/MXene; (2) MOF-derived metal oxide/MXene; (3) MOF-derived metal phosphide/MXene; (4) MOF-derived metal selenide/MXene; (5) MOF-derived metal sulfide/MXene; (6) MOF-derived metal hydroxide/MXene; (7) carbon-based material derived from MOF/MXene-based materials. Each category presents unique challenges and opportunities, highlighting the diverse potential applications of these composite materials.

2.3.1. MOF-derived metal/MXene. With the increasing demand for high-performance composite materials, the combination of MOF-derived metal-based materials with MXene has emerged as a prominent research focus. Wang et al.231 developed a hierarchical composite through electrostatic-mediated assembly. By leveraging cationic attraction between Co and Fe ions and anionic MXene substrates functionalized with surface-terminating groups, they achieved uniform adsorption of metallic precursors. Subsequent introduction of 1,4-benzenedicarboxylic acid as bridging ligand induced spontaneous coordination assembly, generating interlamellar FeCo-MOF spacers that effectively mitigated MXene restacking through structural confinement. The carbonization protocol under controlled pyrolysis enabled in situ formation of bimetallic nanocatalysts, where the spatial restriction from the MOF-derived matrix ensured homogeneous

dispersion of FeCo NPs across the MXene scaffolds. The resulting engineered nanohybrids exhibited dual functional advantages: (1) simultaneous high polarity and ionic-electronic conductivity facilitating polysulfide redox mediation, and (2) optimized sulfur electrochemistry through shortened chargetransfer pathways. Notably, the 0D-2D architecture demonstrated synergistic catalytic functionality by integrating metallic active sites with conductive MXene platforms, significantly enhancing sulfur utilization efficiency in energy storage systems.

Furthermore, considering the suboptimal electrochemical performance of MXene layered 2D structures, Haridas B. Parse et al.232 reported the preparation and electrocatalytic ability of a composite material comprising MXene and Co NPs derived from Co-MOF, encapsulated within N-doped carbon (NC). Han and co-workers²³³ explored the construction of accordion-like MXene@Co-CZIF and MXene@Ni-CZIF composites (derived from the pyrolysis of Co-ZIF and Ni-ZIF, denoted as Co-CZIF and Ni-CZIF, respectively) via an electrostatic self-assembly strategy coupled with subsequent pyrolysis in H₂/Ar atmosphere. As depicted in Fig. 7b, the Co-CZIF component maintained welldefined polyhedral geometry throughout MXene's surface and internal matrix. Fig. 7c demonstrates the effective incorporation of spherical Ni-ZIF nanostructures with hierarchical architecture into the MXene framework through this assembly process, with NPs distributed across both the exterior and interior regions. Xiang et al.234 prepared laminated Ti₃C₂T_x/CNTs/Co through combining microwave-assisted synthesis, in situ carbonization, and electrostatic assembly methods. A schematic illustration of the nanocomposite formation mechanism is presented in Fig. 7a, while Fig. 7d specifically illustrates the anchoring of sea urchin-shaped CNTs/Co nanostructures onto Ti₃C₂T_x MXene substrates. In a subsequent advancement, Liu and co-workers235 fabricated Ti3C2Tx/carbon nanofibers (CNFs)/ TiO₂/CoNi nanocomposites via electrostatic self-assembly combined with thermal treatment. Fig. 7e-g provide a comprehensive overview of the synthetic pathway and morphological characterization, as revealed by SEM analysis.

2.3.2. MOF-derived metal oxide/MXene. MOF-derived metal oxide-based materials/MXene composites have garnered significant research interest owing to their distinctive structural characteristics and synergistically enhanced functional performance.236 These hybrid materials effectively combine the intrinsic high catalytic activity of MOF-derived oxides with the excellent electrical conductivity and robust mechanical stability of MXene. This section provides a systematic overview of the prevailing synthetic strategies employed in the fabrication of MOF-derived metal oxide/MXene.

Ji et al.237 prepared uniform-sized MOF structures via hydrothermal synthesis, which were subsequently subjected to thermal decomposition to yield hollow Fe₂O₃. Concurrently, MXene was synthesized via in situ etching and processed under controlled conditions to enable directional alignment of MXene nanosheets driven by ice-crystal compression, resulting in highly ordered MXene aerogel frameworks. The hollow Fe₂O₃ structures were then dispersed in a silica sol and infiltrated into the porous MXene structure. Ultimately, the processed

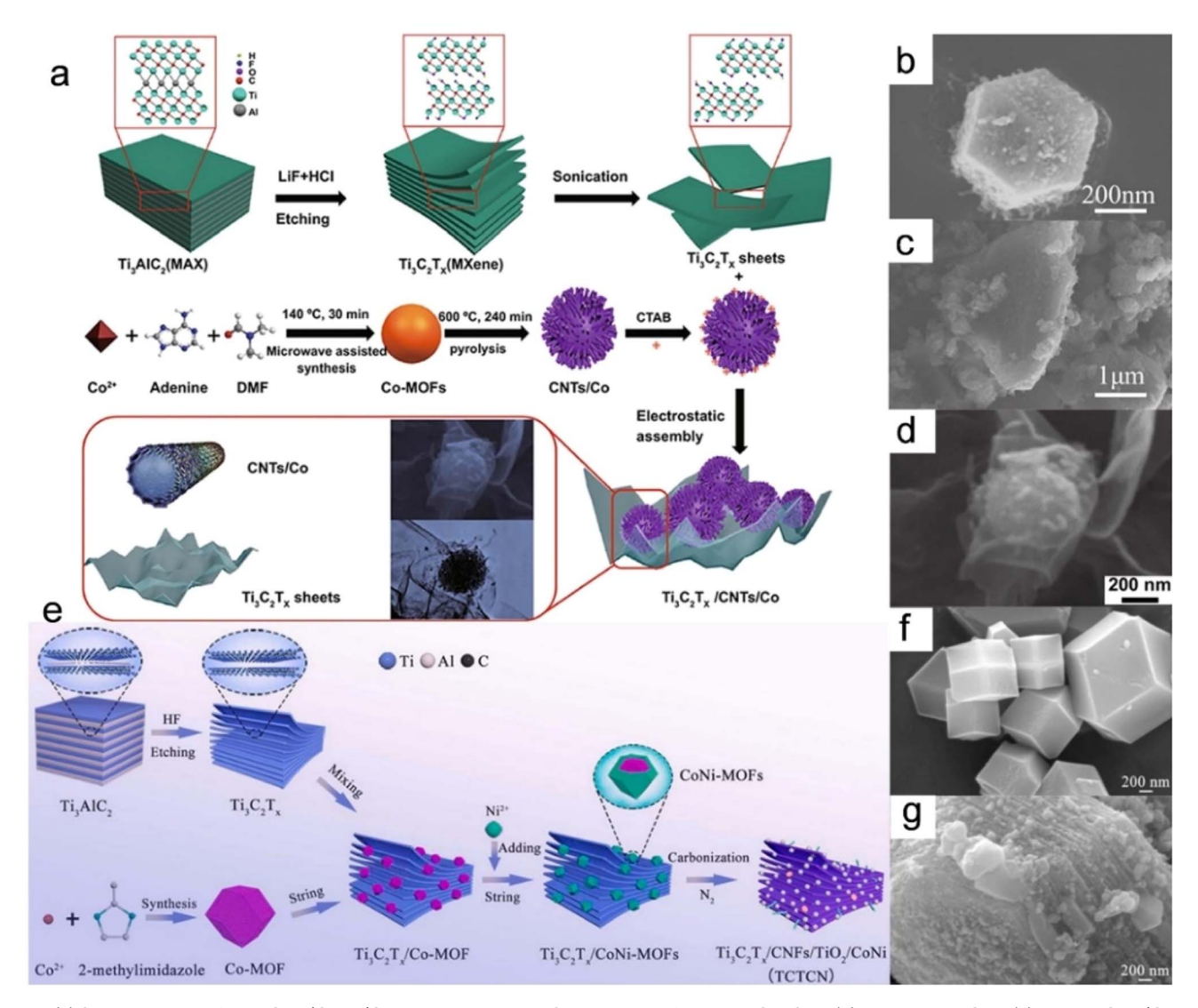


Fig. 7 (a) Synthetic route for $Ti_3C_2T_x/CNTs/Co$ nanocomposites. SEM images of MXene@Co-CZIF (b), MXene@Ni-CZIF (c), and $Ti_3C_2T_x/CNTs/Co$ (d). (e) Scheme for the preparation of $Ti_3C_2T_x/CNFs/TiO_2/CoNi$ nanocomposites. SEM images of CoNi-MOF (f) and $Ti_3C_2T_x/CNFs/TiO_2/CoNi$ nanocomposites (g). (a and d) Reproduced with permission.²³⁴ Copyright 2021, Springer. (b and c) Reproduced with permission.²³⁵ Copyright 2020, American Chemical Society. (e-g) Reproduced with permission.²³⁵ Copyright 2022, Elsevier.

composite underwent lyophilization, yielding MXene-Fe₂O₃-SiO₂ aerogels. Xie and co-workers²³⁸ successfully synthesized a flexible electrode film through vacuum filtration integration of Ti₃C₂T_x and MOF-derived Co-Fe oxide porous nanorods. Fig. 8a illustrates the composite fabrication process, which involves three principal stages. Firstly, the precursor Ti₃AlC₂ undergoes chemical etching using HCl/LiF solution, yielding multilayer MXene sediment that is subsequently delaminated into colloidal suspension via manual agitation. Concurrently, hydrothermal synthesis produces Co-Fe-MOF nanorod precursors that are subsequently calcined in oxidative atmosphere to generate porous mixed oxide phases. The resulting dispersions are combined and subjected to vacuum-assisted filtration, yielding a free-standing Co-Fe oxide/MXene composite film. In 2022, Lei et al.²³⁹ prepared a layered Ti₃C₂T_x hybrid material designated as Ti₃C₂T_x@CoFe@TiO₂ through microwaveassisted thermal treatment of CoFe-MOF@ $Ti_3C_2T_x$ precursor at multiple temperature gradients, employing an integrated in situ synthesis strategy. Shi et al.240 also demonstrated the construction of MOF-derived porous CoFe₂O₄@carbon@alkalized MXene composite architecture using electrospinning, in situ growth, and subsequent calcination. Shingte et al.241 embedded MOF-derived rhombic nickel ferrite NPs (NFO NPs) into Ti₃C₂T_x MXene layers by a straightforward blending technique. The embedded NFO NPs served as effective interlayer spacers, mitigating restacking of MXene nanosheets and thereby increasing the accessible surface area of the composite.

Liu *et al.*²⁴² fabricated a MOF-derived $In_2O_3/Ti_3C_2T_x$ MXene composite using a simple oil-bath method. The synthetic process is illustrated in Fig. 8c. Morphological characterization (Fig. 8d and e) demonstrates the successful growth of pristine

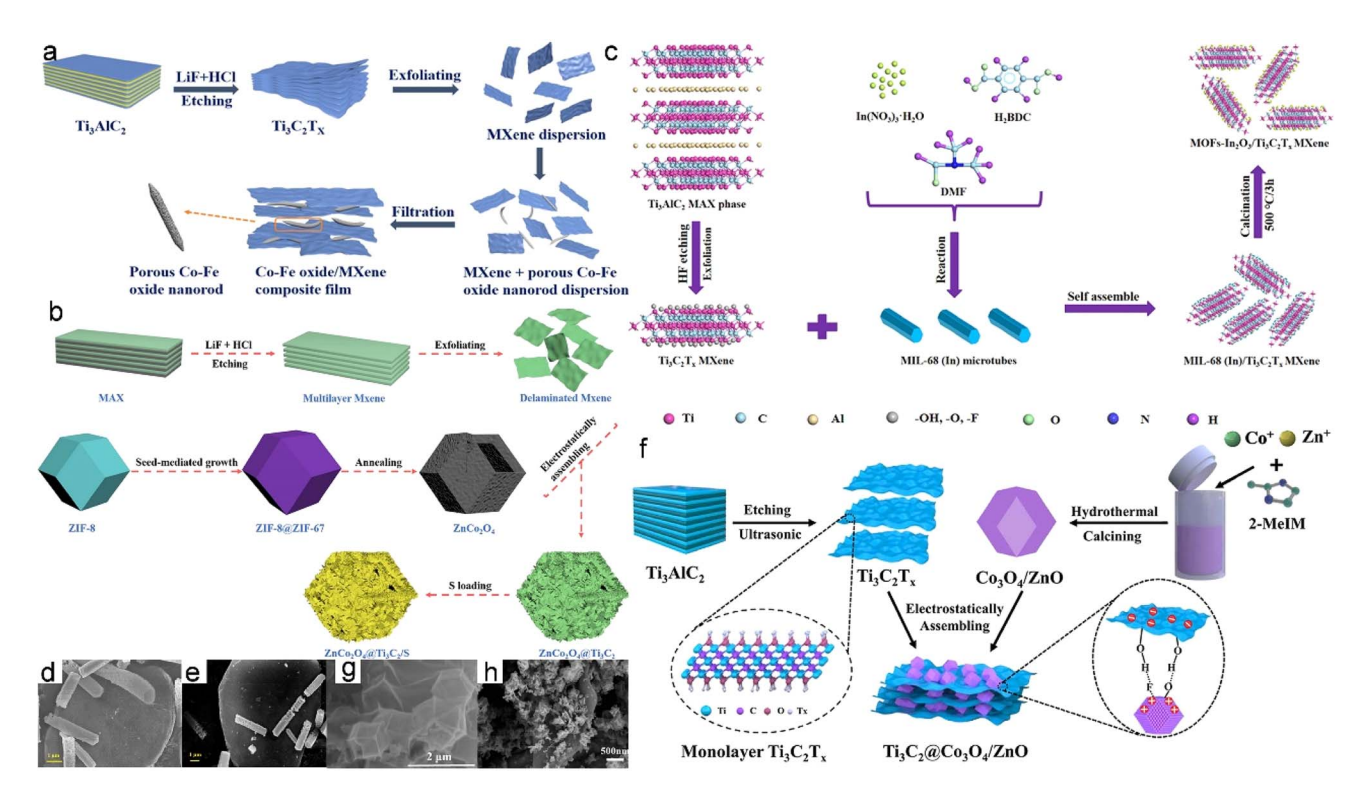


Fig. 8 Schematic fabrication process of Co–Fe oxide/MXene composite film (a), $ZnCo_2O_4@MXene/S$ composite (b), and $In_2O_3/Ti_3C_2T_x$ MXene composite (c). (d and e) SEM images of $In_2O_3/Ti_3C_2T_x$ MXene composite. (f) Schematic illustration of the synthesis approach of MXene@ Co_3O_4/T ZnO composite. (g and h) SEM images of MXene@ Co_3O_4/T and Co_3O_4/T And an anocomposite. (a) Reproduced with permission. Copyright 2020, Elsevier. (b) Reproduced with permission. Copyright 2021, Elsevier. (c-e) Reproduced with permission. Copyright 2022, Elsevier. (f) Reproduced with permission. Copyright 2022, Elsevier. (h) Reproduced with permission

 $\rm In_2O_3$ microtubes on delaminated MXene substrates, confirming effective heterostructure formation through this solution-phase approach. Subsequently, Zhang $et~al.^{243}$ successfully synthesized $\rm In_2O_3/ZnO/MXene$ by integrating MOF-derived hollow $\rm In_2O_3/ZnO$ nanotubes with MXene. The process began with the hydrothermal synthesis of MIL-68(In), followed by the introduction of $\rm Zn(NO_3)_2\cdot 6H_2O$ to form $\rm In_2O_3/ZnO$ hollow nanotubes after calcination. These nanotubes, surface-modified with (3-aminopropyl) triethoxysilane, were dispersed in deionized water and stoichiometrically combined with MXene to yield the final ternary nanocomposite.

Wei and colleagues²⁴⁴ synthesized the ZnCo₂O₄@MXene/S composite. The process involves coating the MXene layer onto hollow ZnCo₂O₄ polyhedron through electrostatic assembly, as shown in Fig. 8b. The synthesis commenced with the production of faceted ZIF-8 nanocrystals through Zn²⁺ coordination with 2-methylimidazole in methanol, which subsequently acted as templates for the epitaxial deposition of ZIF-67 shells. A sequential growth approach was then implemented in Co2+containing methanol solution to construct the core-shell ZIF-8@ZIF-67 architecture. Hollow porous ZnCo2O4 polyhedrons were obtained after annealing treatment. Afterwards, MXene layers were coated on the surface of hollow ZnCo2O4 polyhedrons through electrostatic assembly to form ZnCo₂O₄(a)-MXene composites. Finally, sulfur was introduced into ZnCo₂O₄@MXene 155 $^{\circ}C$ to easily synthesize

ZnCo₂O₄@MXene/S composites. In 2022, Kshetri et al.²⁴⁵ engineered two specialized electrode architectures: a capacitor-type Co-porous carbon (PC)@MXene-CNF and a battery-type MnO₂@Co₃O₄-PC@MXene-CNF assembly, both strategically constructed through hierarchical integration of Co-MOF@MXene-CNF. By strategically combining MOF-derived components with MXene substrates, Wu et al.246 developed a MXene@Co3O4/ZnO hybrid material using an optimized fabrication protocol. The architectural evolution of this multilevel MXene@MOF derivative system is schematically presented in Fig. 8f, revealing its sequential assembly mechanism. morphological characteristics of the synthesized MXene@Co₃O₄/ZnO material are further evidenced by SEM analysis, with representative microstructural features displayed in Fig. 8g. Recently, Bu et al. synthesized the novel mesoporous Co₃O₄/MXene nanocomposites by direct calcination of ZIF-67 grown in situ on MXene sheets. The SEM image of Co₃O₄/ Ti₃C₂T_x nanocomposite (Fig. 8h) reveals that the surfaces of the Ti₃C₂T_x sheets are entirely covered by Co₃O₄ NPs, demonstrating strong interfacial coupling between constituent phases.247 Then, Oh et al. constructed a simple strategy involving the construction of a 2D structural hybrid material consisting of Co₃O₄ and MXene nanosheets coated with N-doped graphite C (NGC), represented as Co₃O₄@NGC. The presence of MXene nanosheets can impart high electronic conductivity and structural stability to the composite material.²⁴⁸ Given that the

restacking of 2D layered materials such as MXene limits their practical scalability, Zhou et~al. prepared an electrocatalyst consisting of MOF-derived hollow ${\rm CoV_2O_6}$ nanocubes (TS- ${\rm V_2CT_x/CoV_2O_6}$ HN) anchored on lattice-stretched ${\rm V_2CT_x}$ MXene, achieved through an ion-exchange process followed by liquid nitrogen quenching. To enhance the electronegativity of nanocomposites, Rahman et~al. engineered a dual-layer triboelectric device with enhanced flexibility and multifunctionality by incorporating MOF-derived nanoporous cobalt oxide (NPCO) blended with silicone polymer alongside MXene-based nanocomposites. Wang et~al. conducted a series of studies on the construction of a hollow ${\rm Co_9S_8}$ core@multi-shell MXene@Bi $_2{\rm O_3}$ structure using MOF as a precursor, with optimization of the flexible substrate by varying the concentration of ${\rm Co_9S_8}$.

In addition, Wang et al.252 designed a Ti₃C₂T_r MXene composite integrated with MOF-derived CuO components. This architecturally layered structure, composed of alternating MXene sheets and CuO NPs derived from MOF precursors, significantly augmented the effective surface area of the resultant MXene-CuO hybrid material. Song et al.253 introduces the strategic combination of MnO2/Mn3O4 derived from MOFs with MXene, leading to the construction of a multifunctional MnO₂/ Mn₃O₄/MXene/Au NPs composite. The hierarchical architecture features 3D MnO₂/Mn₃O₄ microcuboids embedded with vertically oriented nanosheets, which, in synergistic combination with MXene-supported Au NPs, substantially improves both electrochemical characteristics and interfacial accessibility. This design achieves dual enhancement in signal transduction efficiency and biocompatibility through complementary material properties.

2.3.3. MOF-derived metal phosphide/MXene. Zong et al. 254 synthesized a novel MOFs-CoP@MXene composite via the selfassembly method. The MOFs-CoP component is easily deformable, and its heterostructure forms a hollow polyhedral structure that enhances the stability of the MOFs-CoP@MXene composite. Similarly, Liu and co-workers²⁵⁵ successfully synthesized the hierarchical sandwich-like CoP-NC@Ti₃C₂T_x composite through argon-protected in situ intercalation and phosphorylation of MOF@MXene precursors (Fig. 9a). Their approach involved the deposition of geometrically distorted ZIF-67 rhombic dodecahedrons onto Ti₃C₂T_x substrates, creating a ZIF-67@Ti₃C₂T_x architecture. Subsequent thermal treatment triggered ZIF-67 decomposition into 100-200 nm CoP-NC NPs. In a related methodology, Zong et al. 256 engineered Ti2NTr@MOF-CoP heterostructures phosphatefunctionalizing Ti₂NT_x@ZIF-67 assemblies. This protocol commenced with Ti2NTx MXene synthesis, followed by electrostatic-driven ZIF-67 integration and final phosphidation. Li and colleagues reported MXene@MOF-Co₂P nanocomposites through ZIF-67 templating, where nitrogen/carbon-doped Co₂P architectures were immobilized on bimetallic MXene matrices.257 Building on their previous study, Wang and coworkers developed a simple procedure to prepare CoPC/ CNTs@MXene absorbers by combining 0D/1D stratified CoPC/ CNTs with MXene via electrostatic self-assembly. 258

Ma et al.²⁵⁹ employed a self-assembly strategy combined with in situ phosphorization to construct a porous core-shell

CoP@NC nano-polyhedral composite system (CoP@NC/ MXene), using 2D MXene nanosheets as a conductive substrate. The precursor framework was first formed via selfassembly, followed by a phosphorization process that simultaneously generated the CoP core and a NC shell. The incorporation of MXene enhanced charge transfer efficiency through its 2D conductive network and suppressed the pulverization of active materials. Cui et al. 260 focused on the integration of MOFs with 2D materials, synthesizing a layered porous material (graphene oxide (GO)/MXene@NiZrP) by in situ compositing UIO-66 with GO and MXene via hydrothermal and calcination methods. This approach leveraged the dual-substrate synergistic effects of GO and MXene to offer plentiful active sites and modulate interlayer spacing. During calcination, the MOF structure was transformed into metal phosphides while retaining high specific surface area and surface defect characteristics. Zhang et al.261 further expanded the MOF-derived strategy for MXene composites by embedding Co-doped Cu₃P/ NC octahedra (derived from MOF precursors) into MXene interlayers through an in situ growth method, forming a 3D@2D heterostructure (Co-Cu₃P/NC@MXene). This synthetic route not only modulated the electronic structure of Cu₃P via heterometal doping but also leveraged the 2D interlayer confinement effect of MXene to facilitate mass transport, thereby achieving dual optimization of hierarchical architecture and electronic properties.

2.3.4. MOF-derived metal selenide/MXene. Through a practical two-stage synthesis approach involving hydrothermal treatment and subsequent selenization at 400 °C in an argon environment, Hou et al. successfully fabricated multilayer NiSe₂-CoSe₂@C/Ti₃C₂T_x composites. As depicted in Fig. 9b and c, the petal-like structure was disrupted following hightemperature selenization, resulting in the appearance of carbon-coated particles adhering to each other.262 In 2022, Yang and co-workers achieved the fabrication of distinctive 2D hierarchical MXene@CoSe2/Ni3Se4 nanosheets through an innovative template-assisted approach. This method encompassed the in situ growth of MOF on MXene substrates, followed by sequential ion exchange and controlled selenization processes. Fig. 9d presents the synthetic pathway for constructing these multilayered heterostructures. Morphological characterization (Fig. 9e and f) reveals a well-defined architecture in which CoSe₂/Ni₃Se₄ nanolayers uniformly adhere to both sides of the MXene substrates, forming a stable sandwich-like configuration.263 More recently, Li et al. reported on the recent research development regarding the VSe₂-ZrO₂/C/MXene composite by a practical solvothermal method and in situ selenization process.²⁶⁴ Additionally, Shi et al. synthesized the CoSe₂@C/ MXene composite material by annealing a pre-prepared Co-MOF/MXene (mass ratio 10:1) with selenium powder at 650 ° C in an Ar atmosphere for 3 h. The resulting CoSe₂ NPs were uniformly dispersed both on the surface and within the multiheteroatom-doped carbon matrix, while the MXene nanosheets maintained their sheet structure within the composite material.²⁶⁵ Wang et al. reported a series of hollow-structured ZnSe-CoSe composites (45@ZnSe-CoSe/S, 45@ZnSe-CoSe/P/S, 45@ZnSe-CoSe/MXene/S) with distinct hollow

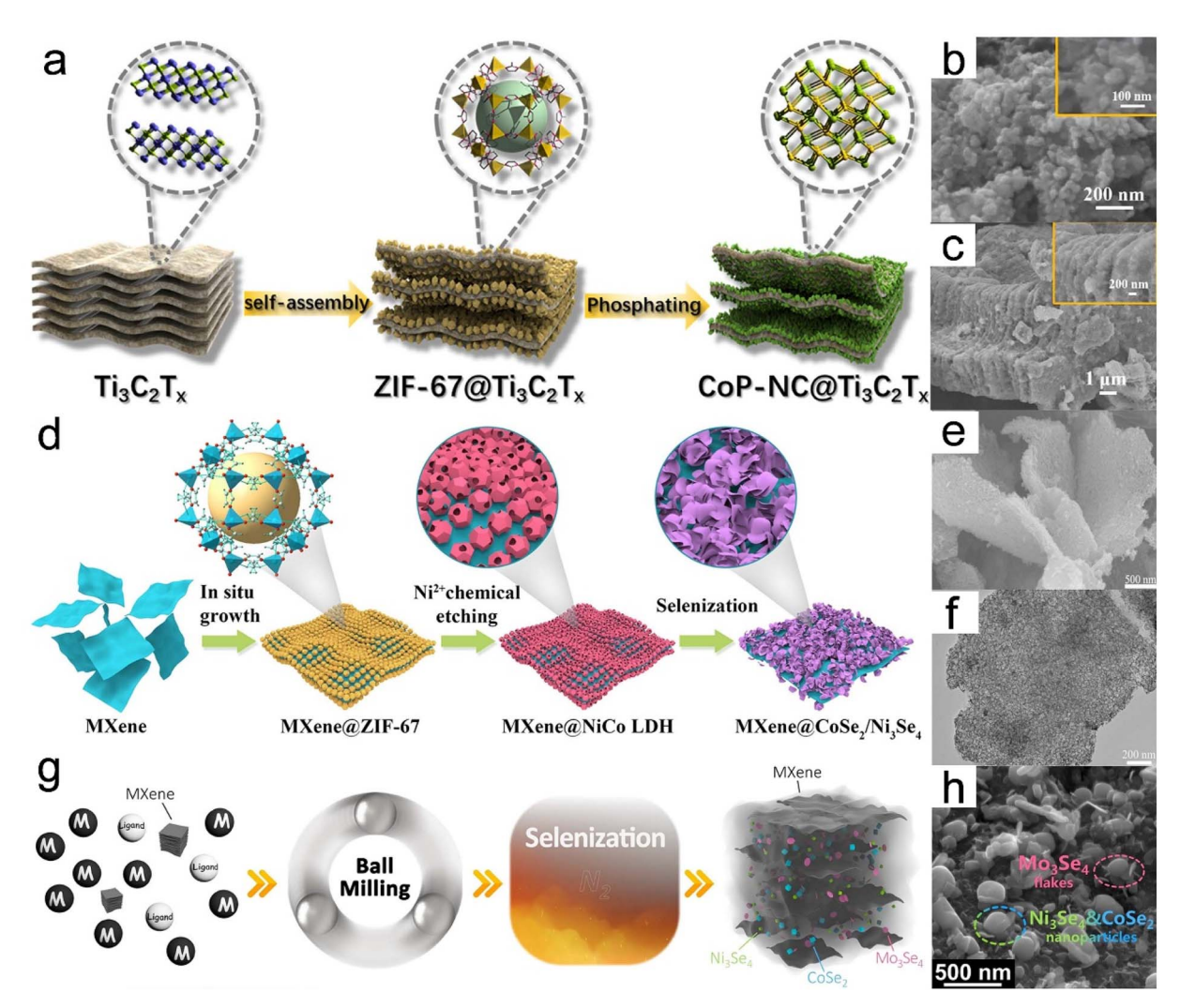


Fig. 9 (a) Formation approach of CoP-NC@Ti $_3$ C $_2$ T $_x$. SEM images of NiSe $_2$ -CoSe $_2$ @C (b) and NiSe $_2$ -CoSe $_2$ @C/Ti $_3$ C $_2$ T $_x$ (c). (d) Schematic view of formation for the hierarchical 2D MXene@CoSe $_2$ /Ni $_3$ Se $_4$ nanosheets. (e) SEM and (f) TEM images of MXene@CoSe $_2$ /Ni $_3$ Se $_4$ nanosheets. (g) Synthetic route of NCMS@C/MX. (h) SEM image of NCMS@C/MX. (a) Reproduced with permission. 255 Copyright 2021, Elsevier. (b and c) Reproduced with permission. 263 Copyright 2022, Elsevier. (g and h) Reproduced with permission. 267 Copyright 2023, Wiley.

architectures, fabricated through a simple two-step synthesis method. This approach combined TA-assisted etching with subsequent selenization treatment of ZIF-8@ZIF-67.266 Fig. 9g presents a schematic diagram outlining the synthesis procedure of MOFs/MXene-derived multi-metal selenides@C/MXene (NCMS@C/MX). Liang et al. achieved the preparation of NCMS@C/MX by first synthesizing MOF and exfoliating MXene, followed by further selenization of the selenides@C/MXene composite. The morphology of NCMS@C/MX composite is depicted in the SEM image (Fig. 9h), where Ni₃Se₄ and CoSe₂ NPs, as well as Mo₃Se₄ nanosheets, are uniformly distributed within the multi-heteroatom-doped carbon matrix.²⁶⁷ Furthermore, the advancement of K-ion batteries (KIBs) faces challenges stemming from insufficient anode materials possessing optimal theoretical capacity, rapid K⁺ transport characteristics, and environmental sustainability. To address this challenge, Hu et al. developed a MOF-templated synthetic route to

fabricate ZnTe@C composites. Their strategy enabled homogeneous dispersion of ZnTe NPs within a conductive carbon framework, which was subsequently immobilized on MXene substrates. Crucially, electronic structure modulation of ZnTe enhanced K⁺ adsorption kinetics, while their pioneering work elucidated the conversion mechanism: $yZnTe + xK^+ + xe^- \rightarrow$ yZn + K_xTe_y, establishing ZnTe as a promising KIB anode.²⁶⁸ Jeong Ho Na and colleagues successfully prepared 3D MXene microspheres via spray-drying assembly. This configuration effectively mitigates MXene sheet restacking while encapsulating MOF-derived ZnSe@NC heterostructures, demonstrating enhanced electrode stability.269 Vallem et al.270 proposed a rational design of a high-efficiency selenium host material, Fe-CNT/TiO2, based on a tailored composite nanostructure. The synthetic protocol involved the initial construction of a MOF-MXene composite, followed by CNT surface decoration, and final high-temperature sintering. The key innovation lies in

utilizing the MOF-derived Fe-CNT structure to provide both conductive networks and catalytic active sites, while the MXene transforms into a TiO₂ phase through sintering, forming a hierarchical porous architecture.

2.3.5. MOF-derived metal sulfide/MXene. Metal sulfides are regarded as highly promising nanomaterials. However, their practical applications are hindered by intrinsic limitations such as poor conductivity and significant volume expansion during electrochemical processes. To address these issues, metal sulfides derived from MOF offer a viable solution by enhancing electrical conductivity and mitigating volume expansion. Moreover, integrating MOF-derived metal sulfides to MXene conductive substrates can further improve their conductivity.²⁷¹ In 2018, Zou et al. synthesized a unique porous Ni-Co mixed metal sulfide (NiCoS), which was grown on MXene derived from ZIF-67/MXene. The preparation process for NiCoS/MXene is depicted in Fig. 10a.272 Subsequently, Wei et al. designed and constructed a MOF-derived NiCo2S4 attached to MXene to form a NiCo2S4@MXene composite. The MOF-derived NiCo2S4 promotes the surface hydroxylation of MXene, facilitating the adsorption of metal ions and inducing sulfur vacancy formation. In addition, MXene provides a high specific surface area, enabling rapid charge carrier transport. Through synergistic interactions between components, the resulting composites have significantly enhanced nonlinear optical and electrochemical properties.²⁷³ In Fig. 10b, Li et al. addressed the primary limitations of metal sulfide materials, namely slow kinetics and severe volume expansion, via utilizing poly(methyl methacrylate) spheres as sacrificial template to form MXene nanosheets. Subsequently, through a multi-step procedure

involving in situ growth, carbonization, and sulfurization processes, they successfully synthesized MXene@CoS₂/NC composite materials comprising MOF-derived CoS2/NC integrated with MXene nanosheets.274 More recently, Adil et al. developed an inventive method for creating the MXene cobalt sulfide (MXene-CoS) composite material. A cost-effective Co-MOF was sulfided and directly integrated with an MXene film via a binder-free in situ growth strategy on NF, resulting in the formation of MXene-CoS/NF. This architecture exhibits favorable structural characteristics, including increased porosity, abundant active sites, enlarged interfacial area, and superior electrocatalytic activity.275 Additionally, Farooq et al.276 established a synthetic strategy for preparing bifunctional electrocatalyst CoS@C/MXene through high-temperature vulcanization. The process involves first combining ZIF-67 with MXene to form a precursor hybrid material, followed by hightemperature vulcanization treatment in a H₂S atmosphere. For instance, the CoS@C/MXene underwent vulcanization at 800 °C, which transformed the cobalt species in ZIF-67 into CoS while simultaneously carbonizing them into a carbon layer structure encapsulating CoS. This structure tightly integrated with the MXene, ultimately forming the CoS@C/MXene nanocomposite.

2.3.6. MOF-derived metal hydroxide/MXene. In recent years, the synthesis strategies of MOF-derived metal hydroxides/MXene composite have demonstrated unique advantages in structural engineering. Hu *et al.*²⁷⁷ innovatively constructed CoFe LDH/MXene composite structure through an "etching-coprecipitation" post-treatment method: by utilizing MXene as a multifunctional support, they anchored MOF precursors and

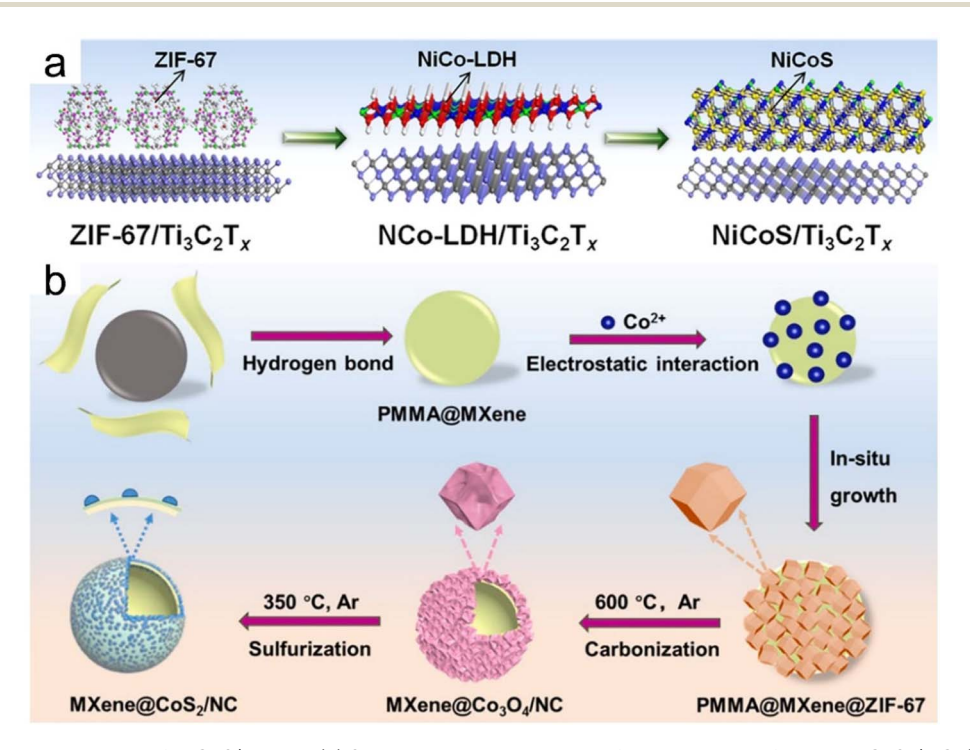


Fig. 10 (a) The preparation process of NiCoS/MXene. (b) Schematic representation of the synthesis of MXene@CoS₂/NC. (a) Reproduced with permission.²⁷² Copyright 2018, American Chemical Society. (b) Reproduced with permission.²⁷⁴ Copyright 2022, Elsevier.

achieved controlled etching to release metal ions, thereby inducing the *in situ* coprecipitation growth of LDH. This interfacial engineering not only optimized the charge transport pathways but also regulated the intermediate adsorption

strength at active sites through strong electronic interactions between CoFe LDH and MXene. In contrast, Kasinathan *et al.*²⁷⁸ adopted a "charge-directed self-assembly" strategy, leveraging electrostatic interactions to integrate chitosan (CS)-modified

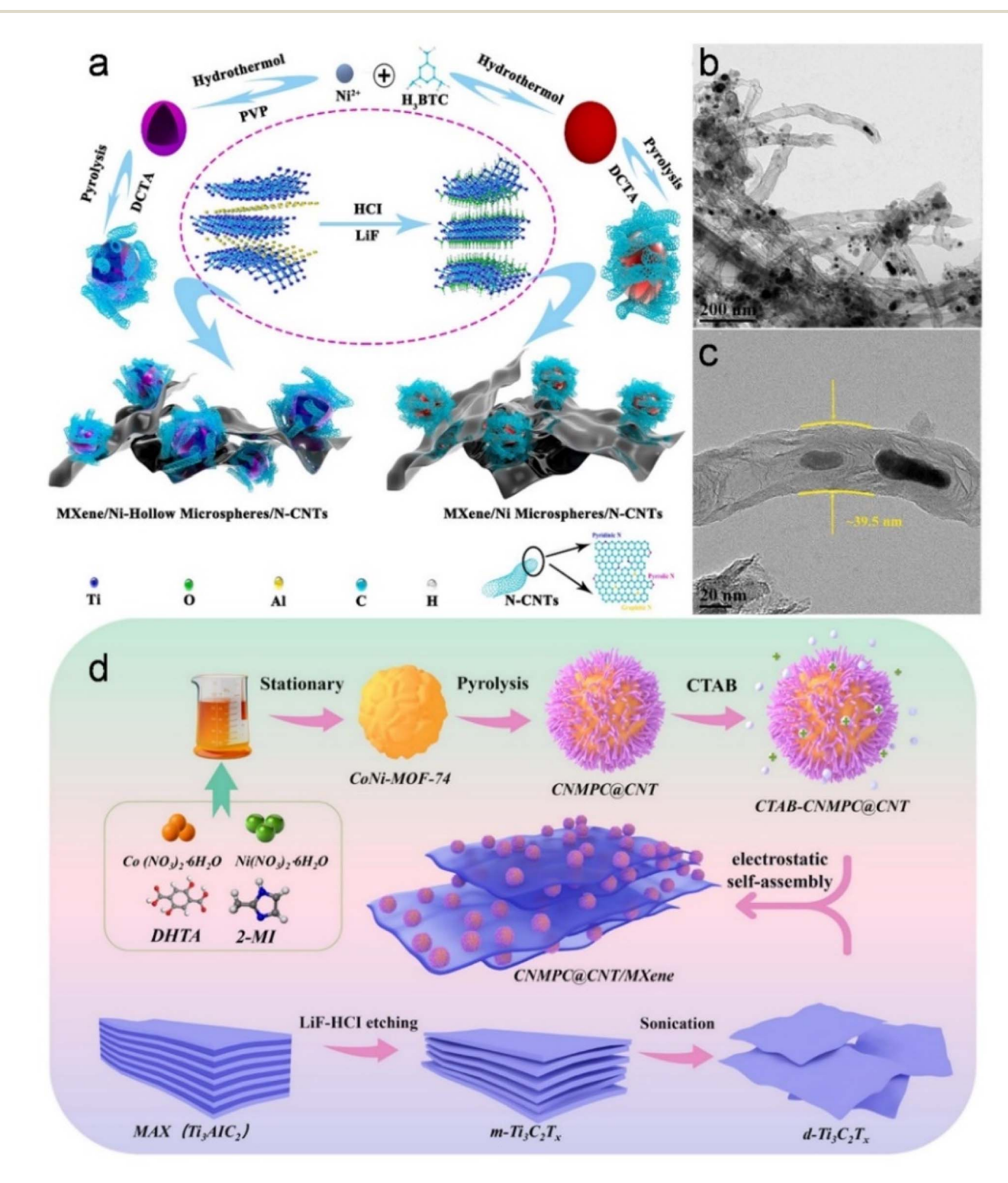


Fig. 11 (a) Schematic illustration of the synthesis of MXene/Ni/N-CNTs. (b and c) TEM images different magnifications of MXene/Ni/N-CNTs nanocomposites. (d) Schematic illustration of the fabrication of CoNi-MPC@CNTs/MXene. (a–c) Reproduced with permission.²⁸² Copyright 2021, Elsevier. (d) Reproduced with permission.²⁸⁴ Copyright 2024, Elsevier.

MXene nanosheets with cobalt-tungsten LDH, resulting in the formation of a CS/MXene@LDH hybrid structure. The selfassembly process, driven by the complementary surface charges of negatively charged MXene and positively charged CoW LDH, enabled uniform dispersion and robust integration of the nanoscale components. Although these two studies differ in application fields, both highlight the shared philosophy of precise structural regulation and functional integration in composite system fabrication through interfacial synergistic design with MXene, employing distinct pathways of chemical etching reconstruction and physical electrostatic adsorption respectively.

2.3.7. Carbon-based material from MOF/MXene-based materials. Synthesis methods of MOF-derived carbon/MXenebased materials have demonstrated diversified innovative pathways in recent years.279-281 To advance the development of high-performance microwave absorption materials, Zhou et al.282 developed an innovative approach by integrating 1D CNTs derived from Ni-MOFs (exhibiting hollow solid microsphere architecture) with 2D MXene to establish an interconnected 3D conductive framework (Fig. 11a-c). In addition, Gu et al. reported a MXene-supported MOF-derived Fe-N-C catalyst (Fe-Nx/N/MXene), which exhibits good oxygen

reduction reaction (ORR) activity and long-term stability.283 To achieve optimal electromagnetic wave (EMW) absorption capability, Wu et al. synthesized a Co-Ni-MOF-derived waxberry-like magnetic porous carbon (CoNi-MPC)@CNTs/ MXene hybrid (CoNi-MPC@CNTs/MXene) through a simple solution precipitation, heat treatment, and electrostatic selfassembly strategy (Fig. 11d).284

In 2018, in order to further enhance the electromagnetic attenuation ability, Liao and co-workers285 prepared laminated Co/TiO₂-C hybrids through thermal treatment of Ti₃C₂T_r/Co-MOF, integrating them with MXene-derived TiO₂-C laminates (Fig. 12a-d). Building upon this foundation, Deng et al. 286 subsequently engineered innovative sandwich-structured 2D nanocomposites containing Fe & TiO2 NPs embedded in carbon matrices, utilizing MXene-MOF hybrid architectures as synthetic platforms. As shown in Fig. 12e-h, Fe-MOFs were initially transformed into Fe₃O₄/PC, and subsequently formed carbon-coated Fe NPs (Fe@C) under a reducing atmosphere. With increasing pyrolysis temperature, both TiO2 and Fe particles exhibited progressive growth and pronounced aggregation. Recently, Wang and colleagues287 successfully prepared 3D spherical Ni/TiO₂/C microspheres alongside hierarchically layered Ni/TiO2/C nanocomposites through an innovative

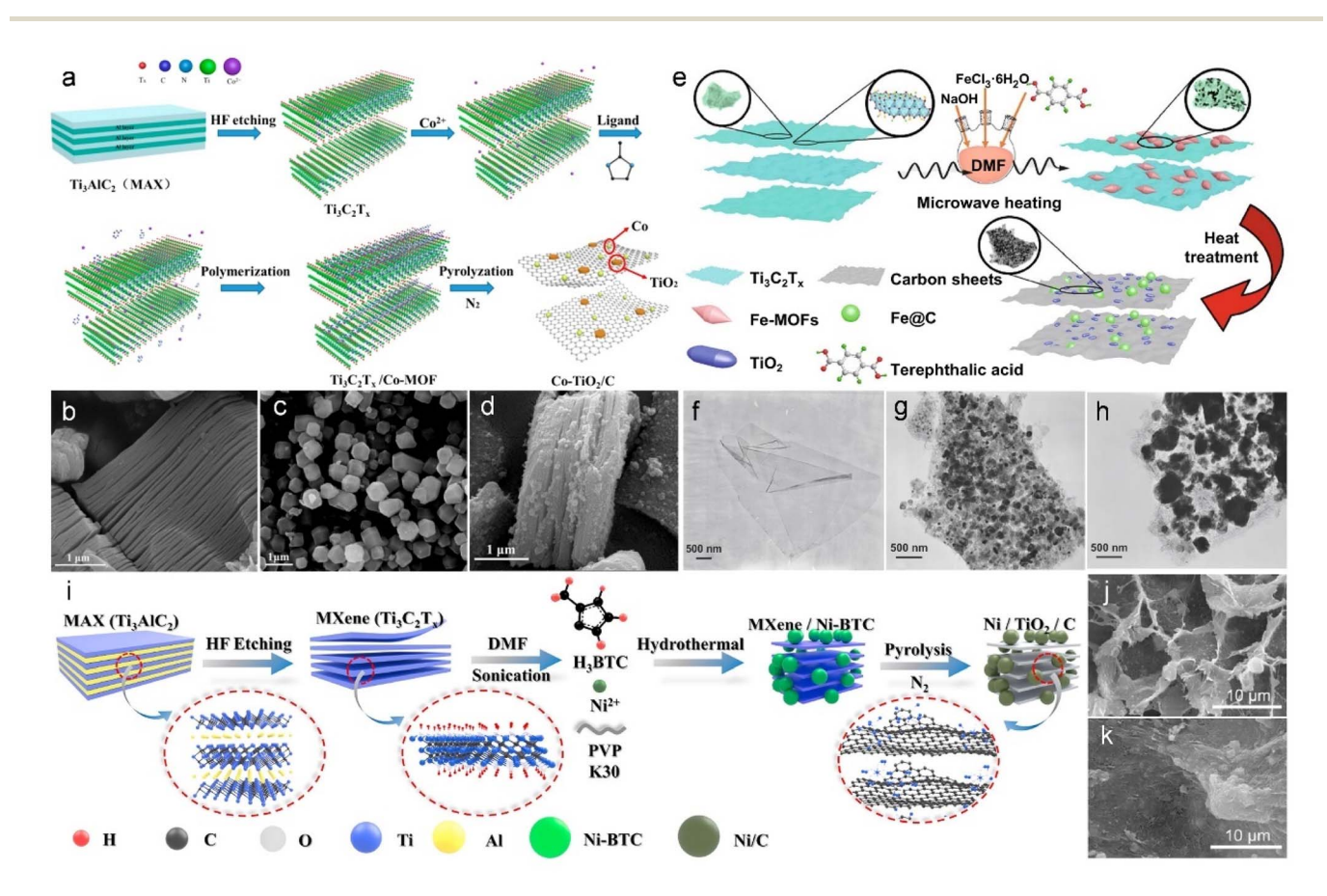


Fig. 12 (a) Illustration of the preparation of Co/TiO₂–C. (b–d) SEM images of $Ti_3C_2T_x$, Co-MOF, and Co/TiO₂–C composites. (e) Preparation of Fe & TiO₂@C. (f-h) TEM images of $Ti_3C_2T_x$, Fe & TiO_2 @C (700 °C), and Fe & TiO_2 @C (800 °C). (i) Illustration of the fabrication process of Ni/TiO₂/C nanocomposites. (j and k) SEM images of ZIF-67/Nb₂CT_x/cellulose aerogel and Co/Nb₂CT_x/cellulose CA. (a–d) Reproduced with permission. 285 Copyright 2018, American Chemical Society. (e-h) Reproduced with permission.²⁸⁶ Copyright 2020, Springer. (i) Reproduced with permission.²⁸⁷ Copyright 2022, Elsevier. (j and k) Reproduced with permission.²⁸⁸ Copyright 2023, American Chemical Society.

RSC Advances Review

synthesis approach. Utilizing Ni-BTC and Ti₃C₂T_x MXene as precursor materials, the researchers implemented an in situ solvothermal self-assembly strategy coupled with controlled thermal annealing. The resulting nanostructures incorporate precisely arranged 2D carbon matrices hosting uniformly dispersed TiO2 NPs (Fig. 12i). Cui et al.288 employed biomassderived bamboo as carbon source to construct a 3D interconnected network through porous structure engineering strategy. Briefly, bamboo cellulose was assembled with few-layer Nb₂CT_r MXene to form a 3D aerogel framework. Subsequently, ZIF-67 precursors were uniformly anchored via chemical deposition, and ultimately Co NPs/Nb2CT2/CA composite was obtained through high-temperature pyrolysis (Fig. 12j and k). This architecture establishes a conductive network through synergistic interactions between the biomass-derived carbon matrix and MXene components, while simultaneously optimizing impedance matching via interfacial polarization and magnetic loss contributions from MOF-derived magnetic nanoparticles. Zheng et al. 289 proposed a biomimetic structural design strategy. Their methodology employed solvothermal synthesis to realize controlled in situ crystallization of bimetallic CoNi-MOF within MXene layers, which subsequently underwent pyrolysis conversion into magnetically responsive carbon hybrids (CoNi@C). This transformation process yielded a hierarchically organized structure mimicking marine coral morphology. This strategy effectively alleviates MXene stacking through interlayer-embedded MOF-derived carbon nanorods, while introducing porous heterogeneous interfaces to enhance dielectric-magnetic coupling effects. Furthermore, Guo et al.290 innovatively addressed limitations associated with single-layer architectures through a sequential vacuum-assisted filtration strategy. Their Janus architecture combined two functionally distinct components: a magnetic CNF composite derived from CoNi-MOF-74 served as the electromagnetic absorption layer, and MXene/CNF acting as the reflective layer. The integrated system achieved robust interfacial bonding via hydrogen bonding interactions between constituent layers. This duallayer architecture not only optimizes electromagnetic dissipation pathways through "absorption-reflection-reabsorption" mechanism, but also enhances multifunctionality by harnessing MXene's plasmonic effects and the mechanical reinforcement properties of CNF.

2.3.8 Summary. The synthesis of MOF derivative/MXene composites, as detailed in the previous sections, is fundamentally different from that of pure MOF/MXene or MOF composite/MXene materials. The defining characteristic of this type of material is the essential role of post-synthetic thermal treatment (*e.g.*, calcination, pyrolysis, sintering) in transforming the MOF structure into the final derivative while preserving the structural integrity of the MXene substrate.

A critical analysis reveals that the synthesis strategy is a multi-step process: firstly, a precursor composite is formed by integrating the MOF with MXene, and secondly, this composite undergoes a controlled thermal transformation to generate the derivative. The choice of the initial integration method for the precursor is diverse. *In situ* growth is a common approach, used to construct MOF@MXene that are subsequently converted into

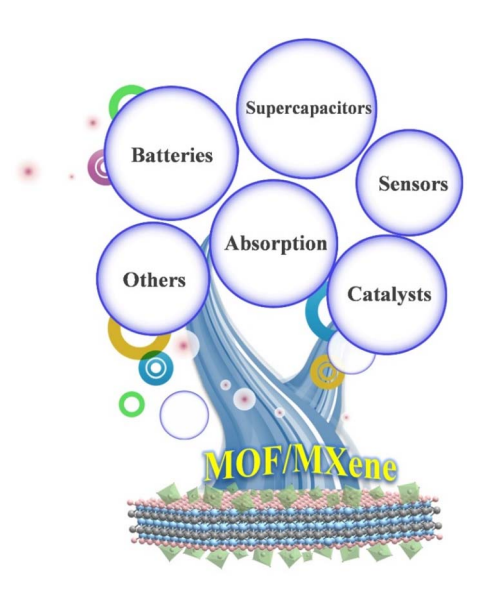
metal phosphides²⁶¹ or metal sulfides.²⁷⁵ Electrostatic self-assembly is also highly effective for creating the initial hybrid, as demonstrated by the formation of MXene@Co-CZIF and MXene@Ni-CZIF composites, which were then pyrolyzed to form metal/carbon hybrids.²³³ Solvothermal methods are employed to create layered porous materials, such as GO/MXene@NiZrP, which are then transformed into phosphides *via* calcination.²⁶⁰

The thermal treatment step is the most critical and challenging aspect. The temperature, atmosphere (*e.g.*, N₂, Ar), and heating rate must be meticulously controlled. The objective is to completely decompose the MOF into the desired derivative (*e.g.*, metal, oxide, phosphide, sulfide), while minimizing the oxidation and degradation of the MXene. For instance, the successful synthesis of MOF-derived metal phosphides, ^{260,261} sulfides, ^{275,276} and hydroxides ²⁷⁷ depends on finding this delicate balance. The use of MXene as a conductive and mechanically robust substrate not only provides a support for MOF precursors but also plays a crucial role in stabilizing the derivative phases and preventing its aggregation during the high-temperature process.

In conclusion, the synthesis of MOF derivative/MXene composites is a complex process, with the core being the integration of MOF precursors with MXene, followed by precisely controlled thermal transformation. The success of this strategy depends on the synergy between a well-designed precursor architecture and optimized thermal conditions to achieve high-performance hybrid materials.

3. Applications

The versatility of MOF/MXene-based materials is illustrated in Scheme 3, highlighting their broad applicability batteries, 291-293 SCs, 120,245 sensors, 294-296 catalysts, 297-299 and absorption. 300-302 In advanced battery systems, MOF compounds serve bifunctional roles. These porous materials serve not only as high-performance anode components in lithium-ion batteries (LIBs) due to their exceptional specific capacity and outstanding energy storage properties, but also show promise as cathode materials by maintaining stable redox activity and effectively mitigating detrimental shuttling effects.303 For SC applications, MOF/MXene composites demonstrate ultra-high specific capacitance and excellent reversibility, rendering them strong candidates as binder-free electrode materials. 105,196 Furthermore, MOF/MXene composites are extensively utilized in multiple sensing applications, showcasing remarkable adaptability. For example, efficient sensors for arsenate detection in electrochemistry, self-powered biomotion and tactile sensing applications, electrochemically sensitive sensors for H₂O₂ detection, and as organoid gas sensors. 129,133,216 In summary, these sensors demonstrate outstanding selectivity, consistent reproducibility, and durable operational stability, attributes that collectively contribute to technological advancements in societal infrastructure. The unique combination of adjustable surface properties, architectural versatility, and expansive active interfaces has positioned MOF/MXene hybrid systems as a focal point in advanced materials



Scheme 3 Application of MOF/MXene-based materials

research. These attributes make it a promising catalyst material with high electrical conductivity, including oxygen evolution reaction (OER),³⁰⁴ hydrogen evolution reaction (HER),³⁰⁵ ORR,³⁰⁶ and photocatalysts.^{307,308}

In the field of EMW absorption, MOF/MXene-based materials demonstrate exceptional EMW attenuation capabilities, significantly enhancing absorption efficiency and exhibiting great potential for next-generation intelligent electromagnetic shielding systems.²⁹⁰ Due to their lightweight nature and broad absorption bandwidth, these materials can address a range of electromagnetic pollution issues in daily life. High-performance

absorbing materials can markedly enhance the absorption performance of EMW and positively impact microwave absorption performance, showcasing an excellent absorption bandwidth.²⁸⁶ This suggests that MOF/MXene-based materials play a significant role in societal development. MOF/MXene-based materials can serve as highly effective flame retardants, enhancing fire safety while also possessing adsorption and sterilization effects.^{141,172} These hybrid systems show particular promise for dual applications in agricultural engineering (particularly paddy field management) and biomedical wound care, with documented therapeutic implementations already contributing to enhanced healthcare outcomes and quality-of-life improvements.³⁰⁹

3.1. Batteries

MOF materials demonstrate significant potential as battery electrode materials, offering advantages including numerous active sites, hierarchically porous architectures, minimized ion transport distances, and tunable chemical compositions. However, their relatively low electronic conductivity remains a limitation. Therefore, developing innovative electrode architectures with enhanced energy storage performance and mechanical robustness represents a vital research direction. The research findings on MOF/MXene-based materials for battery over the past few years are presented in Table 1.

Within the realm of MOF/MXene composites, both 3D $\rm Ti_3C_2$ MXene/NiCo-MOF composite films¹⁸² and 2D MXene/NiCo MOF heterostructures¹⁸⁵ have been identified as highly effective anodes for high-performance LIBs. The optimized MXene/NiCo-MOF electrode showcases remarkable electrochemical characteristics, delivering a reversible capacity of 402 mA h g $^{-1}$ at 0.1 A g $^{-1}$ with sustained rate capability (256 mA h g $^{-1}$ at 1 A g $^{-1}$)

Table 1 MOF/MXene-based materials for batteries, including LIBs, LSBs and others

Type of	Reversible capacity/	Cycling performance	
batteries	current density	(capacitance retention, cycle, current density)	Ref.
LIBs	402 mA h g ⁻¹ /0.1 A g ⁻¹	$85.7\%, 400, 1 \text{ A g}^{-1}$	182
LIBs	637 mA h $g^{-1}/0.2 A g^{-1}$	304 mA h g^{-1} , 800 , 1 A g^{-1}	185
LIBs	980 mA h $g^{-1}/0.2 A g^{-1}$	80% , 5000 , 5 A g^{-1}	311
LIBs	121 mA h $g^{-1}/5C$	89.6%, 500, 1C	221
LIBs	706.5 mA h $g^{-1}/0.2$ A g^{-1}	585.8 mA h g ⁻¹ , 1000, 0.5 A g ⁻¹	254
LIBs	612.2 mA h $g^{-1}/0.1$ A g^{-1}	430 mA h g ⁻¹ , 1000, 1 A g ⁻¹	264
LIBs	536.7 mA h $g^{-1}/1$ A g^{-1}	$63.1\%, 2000, 1 \text{ A g}^{-1}$	310
LIBs	1300 mA h $g^{-1}/0.5$ A g^{-1}	1097 mA h g^{-1} , 1000, 1 A g^{-1}	271
LIBs	$327 \text{ mA h g}^{-1}/50 \text{ A g}^{-1}$	830 mA h g ⁻¹ , 500, 1 A g ⁻¹	248
LSBs	$1017 \text{ mA h g}^{-1}/0.1\text{C}$	46%, 1000, 1C	177
LSBs	840 mA h $g^{-1}/0.5C$	38.5%, 1500, 1C	293
LSBs	$547 \text{ mA h g}^{-1}/0.2\text{C}$	26.8%, 400, 0.5C	244
LSBs	$478 \text{ mA h g}^{-1}/0.2\text{C}$	387.2 mA h g ⁻¹ , 400, 0.5C	266
LSBs	$703 \text{ mA h g}^{-1}/4\text{C}$	58%, 1000, 1C	231
KIBs	$408 \text{ mA h g}^{-1}/0.1 \text{ A g}^{-1}$	230.2 mA h g ⁻¹ , 3500, 1 A g ⁻¹	268
KIBs	180 mA h $g^{-1}/0.5$ A g^{-1}	238 mA h g ⁻¹ , 1000, 0.5 A g ⁻¹	269
KIBs			312
SIBs			255
SIBs	658.6 mA h $g^{-1}/0.05 A g^{-1}$	61 mA h g^{-1} , 500, 2 A g^{-1}	259
SIBs	$620 \text{ mA h g}^{-1}/0.2 \text{ A g}^{-1}$	87.5% , 5000 , 5 A g^{-1}	274
SIBs	$402.9 \text{ mA h g}^{-1}/0.1 \text{ A g}^{-1}$	259.8 mA h g ⁻¹ , 1800, 1 A g ⁻¹	265
SIBs	416 mA h $g^{-1}/0.1$ A g^{-1}	$130, 1000, 1 \text{ A g}^{-1}$	240
	LIBS LIBS LIBS LIBS LIBS LIBS LIBS LIBS	LIBS 402 mA h g ⁻¹ /0.1 A g ⁻¹ LIBS 637 mA h g ⁻¹ /0.2 A g ⁻¹ LIBS 980 mA h g ⁻¹ /0.2 A g ⁻¹ LIBS 121 mA h g ⁻¹ /0.2 A g ⁻¹ LIBS 706.5 mA h g ⁻¹ /0.2 A g ⁻¹ LIBS 612.2 mA h g ⁻¹ /0.1 A g ⁻¹ LIBS 536.7 mA h g ⁻¹ /0.1 A g ⁻¹ LIBS 1300 mA h g ⁻¹ /0.5 A g ⁻¹ LIBS 327 mA h g ⁻¹ /0.1C LSBS 1017 mA h g ⁻¹ /0.1C LSBS 840 mA h g ⁻¹ /0.5C LSBS 840 mA h g ⁻¹ /0.2C LSBS 478 mA h g ⁻¹ /0.2C LSBS 478 mA h g ⁻¹ /0.2C LSBS 703 mA h g ⁻¹ /0.1 A g ⁻¹ KIBS 408 mA h g ⁻¹ /0.5 A g ⁻¹ KIBS 408 mA h g ⁻¹ /0.2 A g ⁻¹ SIBS 180 mA h g ⁻¹ /0.0 A g ⁻¹ SIBS 658.6 mA h g ⁻¹ /0.05 A g ⁻¹ SIBS 620 mA h g ⁻¹ /0.2 A g ⁻¹ SIBS 620 mA h g ⁻¹ /0.1 A g ⁻¹	LIBs

RSC Advances Review

through 300 cycles. These enhancements stem from synergistic effects including three-dimensional porous networks, expanded surface area, accelerated electron transport kinetics, and optimized Li⁺ diffusion pathways. Long-term cycling stability data (Fig. 13a) reveal 85.7% capacity retention after 400 cycles at 1 A g⁻¹, confirming structural resilience under high current operation. Complementary cyclic voltammetry (CV) analysis conducted at various scan rates (Fig. 13b) further confirms the superior electrochemical behavior of these composites. 182 Electrochemical characterization of the Ti₃C₂T_x/NiCo MOF heterostructure displays progressive capacity enhancement during cycling (Fig. 13c), a phenomenon associated with gradual electrode activation and dynamic evolution of a functional gel-like interfacial layer. The material's exceptional rate adaptability, as shown in Fig. 13d, combined with its distinctive voltage profiles across cycling stages, highlights the advantages of combining conductive MXene substrates with redox-active bimetallic MOF structure (Fig. 13e).185 Notably, the MOF@M-Xene heterostructure anode developed by Sun et al. exhibits remarkable electrochemical performance, maintaining 80% capacity retention over 5000 cycles at 5A g⁻¹, a significant improvement compared to individual MXene and MOF components. Li⁺ kinetics were investigated *via* CV measurements across scan rates ranging from 0.1 to 1 mV s⁻¹ (Fig. 13f), with long-term cycling stability at high current density is illustrated in Fig. 13g. Structural analysis in Fig. 13h identifies two distinct Li⁺ adsorption sites (labeled 1 and 2) in the pure NF-MOF. Overall, this hybrid architecture demonstrates enhanced Li storage capabilities and superior rate performance as LIB anodes, exceeding the electrochemical characteristics of both constituent materials when used separately.³¹¹

Furthermore, a novel polymer composite electrolyte reinforced with ZIF-8@MXene nanosheets (PE-ZIF-8@MXene) was developed by Zhao *et al.* When implemented in symmetric lithium battery configurations, the PE-ZIF-8@MXene enabled stable operation for 2000 h at 0.5 mA cm⁻². Electrochemical performance evaluation revealed that Li|PE-ZIF-8@MXene|Li batteries maintained 89.6% of their initial capacity through 500 cycles (Fig. 14c). Comparative analysis with conventional PE demonstrated the modified electrolyte's superior voltage hysteresis characteristics across varying current densities (Fig. 14a). Current-dependent polarization effects were observed

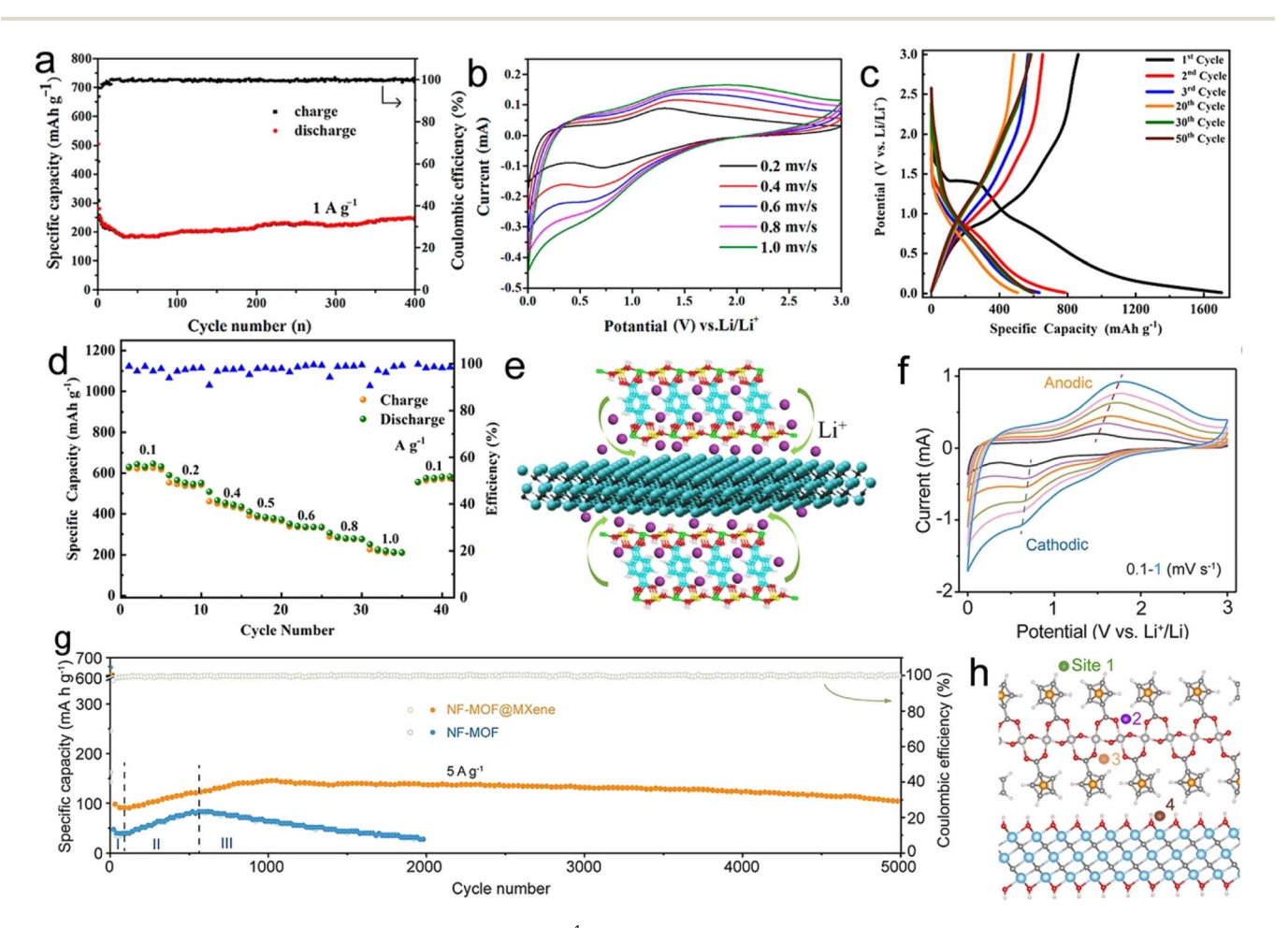


Fig. 13 (a) Cycle performance of MXene/NiCo-MOF at 1 A g^{-1} . (b) CV curves of the MXene/NiCo-MOF at different scan rates. (c) The discharging/charging curves of the $Ti_3C_2T_x/NiCo-MOF$ electrode at 0.2 A g^{-1} . (d) Rate performance of the $Ti_3C_2T_x/NiCo-MOF$. (e) Illustration of the Li⁺ intercalation of the MXene/NiCo-MOF heterostructure. (f) CV curves of NF-MOF@MXene at different scan rates. (g) Cycling performance at 5 A g^{-1} . (h) Lithium adsorbed at different sites. (a and b) Reproduced with permission. Diversity Preservation International. (c-e) Reproduced with permission. Copyright 2022, Elsevier.

in the voltage-capacity profiles, with minimal increases noted when scaling current density from 0.5C to 2C (Fig. 14b).²²¹

In the development of MOF derivative@MXene composites, Zong *et al.* synthesized an innovative MOFs-CoP@MXene hybrid through structural engineering. When employed as a LIB anode, this composite demonstrated exceptional cycling durability. As a cathode material for lithium–sulfur batteries (LSBs), it exhibited dual functionality: stable sulfur redox kinetics and significant mitigation of polysulfide shuttle phenomena through chemical confinement. Electrochemical characterization revealed distinct redox peaks in CV profiles (1.5–3.0 V, 0.1 mV s⁻¹), with the MOFs-CoP@MXene/S configuration showing enhanced cathodic activity evidenced by dual

reduction peaks at 2.02 and 2.37 V, compared to the MOFs-CoP/S counterpart (Fig. 14d). The initial charge and discharge capacities of the MOFs-CoP@MXene/S were 1138.8 mA h g $^{-1}$ at 0.2C (Fig. 14f). Fig. 14g presents the inherent mechanism by which MOFs-CoP@MXene/S inhibits the sulfide shuttle effect, thereby exerting its catalytic potential. 254 A MXene-based composite integrating VSe $_2$ –ZrO $_2$ and carbon components (VSe $_2$ –ZrO $_2$ /C/MXene) was developed by Li and co-workers as advanced LIB anode material. This engineered material exhibited enhanced electrochemical characteristics, initially displaying capacity fluctuation before achieving remarkable improvement from 461.2 to 1238.5 mA h g $^{-1}$ at 100 mA g $^{-1}$. Notably, the composite exhibited exceptional durability with

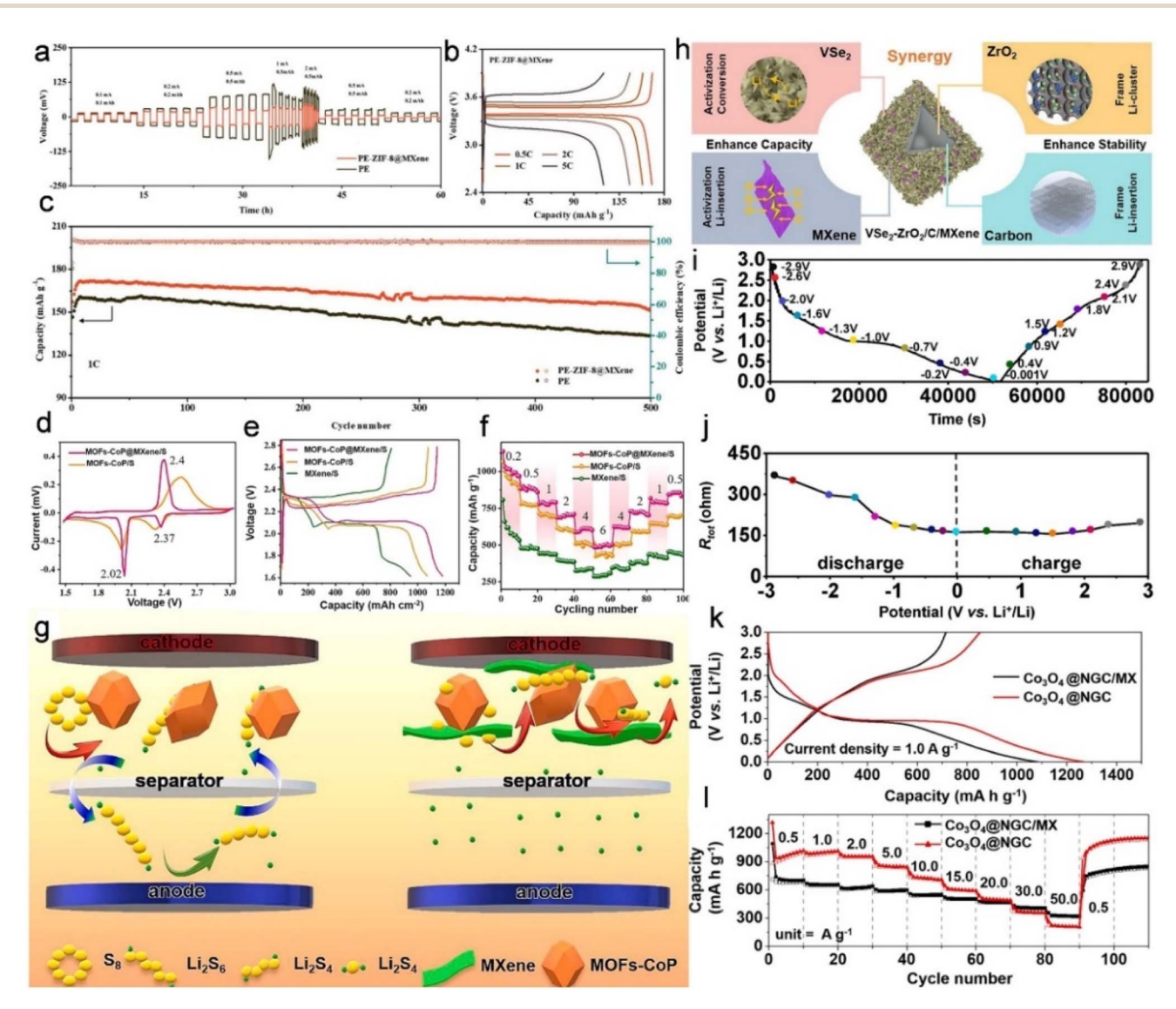


Fig. 14 (a) Rate performances of symmetric batteries with PE-ZIF-8@MXene and PE. (b) Concentrated voltage-capacity curves of PE-ZIF-8@MXene. (c) Cycling performance of PE-ZIF-8@MXene and PE. (d) CV curves of MOFs-CoP/S and MOFs-CoP@MXene/S. (e) Discharge-charge curves of MOFs-CoP@MXene. (f) Rate capability of MXene/S, MOFs-CoP/S and MOFs-CoP@MXene/S. (g) Schematic illustration of the inhibition mechanism of MOFs-CoP/S and MOFs-CoP@MXene/S. (h) Schematic of VSe₂-ZrO₂/C/MXene for the Li-ion storage mechanism. (i) Potential vs. time curve and (j) graph for the change of R_{tot} values at specific potential levels of Co_3O_4 @NGC/MXene electrode for LIBs during the initial cycling. (k) The initial profile curves and (l) rate performance of Co_3O_4 @NGC and Co_3O_4 @NGC/MXene electrodes for LIBs. (a-c) Reproduced with permission.²⁵⁴ Copyright 2021, Elsevier. (h) Reproduced with permission.²⁶⁴ Copyright 2023, Royal Society of Chemistry. (i-l) Reproduced with permission.²⁶⁸ Copyright 2021, Elsevier.

RSC Advances Review

430 mA h g⁻¹ retention after 1000 cycles under1.0 A g⁻¹, confirming its structural resilience. The underlying charge storage mechanism is visually elucidated in the corresponding schematic diagram (Fig. 14h).264 Recent studies by Oh et al. have identified the Co₃O₄@NGC/MXene hybrid as a promising LIBs anode material, demonstrating remarkable energy storage characteristics. The composite maintained 830 mA h g⁻¹ after 500 cycles at 1.0 A g^{-1} , along with superior rate performance delivering 327 mA h g^{-1} at 50.0 A g^{-1} . The electrochemical behavior analysis reveals: Fig. 14i quantifies cycle endurance across different voltage windows, while Fig. 14j tracks the evolution of total resistance (Rtot) during initial battery operation. Comparative charge-discharge curves of Co₃O₄@NGC and Co₃O₄@NGC/MXene electrodes at 1.0 A g⁻¹ are presented in Fig. 14k. Both configurations showed stable long-term cyclability, sustaining performance over 500 cycles as evidenced in Fig. 14l.248

LSBs have garnered significant attention as a promising rechargeable battery.³¹³ Wen *et al.* initially synthesized the 3D

hierarchical Zr-MOF/Ti₃C₂T_x nanocomposite, which displayed a substantial discharge/charge capacity of 801 mA h g⁻¹ (Fig. 15b) at 1C and excellent cycling properties. Fig. 15c illustrates the long-term cycling performance of the Zr-MOF/Ti₃C₂T_r composite over 1000 cycles at 1C rate. Fig. 15a depicts the working mechanism of the Zr-MOF/Ti₃C₂T_r/S composite in LSBs. 177 The superior architecture of the Zr-MOF/Ti₃C₂T_x nanocomposites significantly enhances the electronic conductivity and charge transfer kinetics of the entire cathode, accelerates the redox conversion rate of chemisorbed polysulfide, and effectively protects the lithium anode from contamination. Building upon previous advancements, Wei and co-workers further engineered a ZnCo₂O₄@Ti₃C₂/S composite serving as an effective sulfur host material for LSBs. This innovative configuration achieved remarkable electrochemical metrics, including a primary discharge capacity of 1283.9 mA h g⁻¹ and an exceptional initial coulombic efficiency of 98.7% under 0.1C. The system's electrochemical durability was further validated through extended cycling evaluations at 0.5C, with

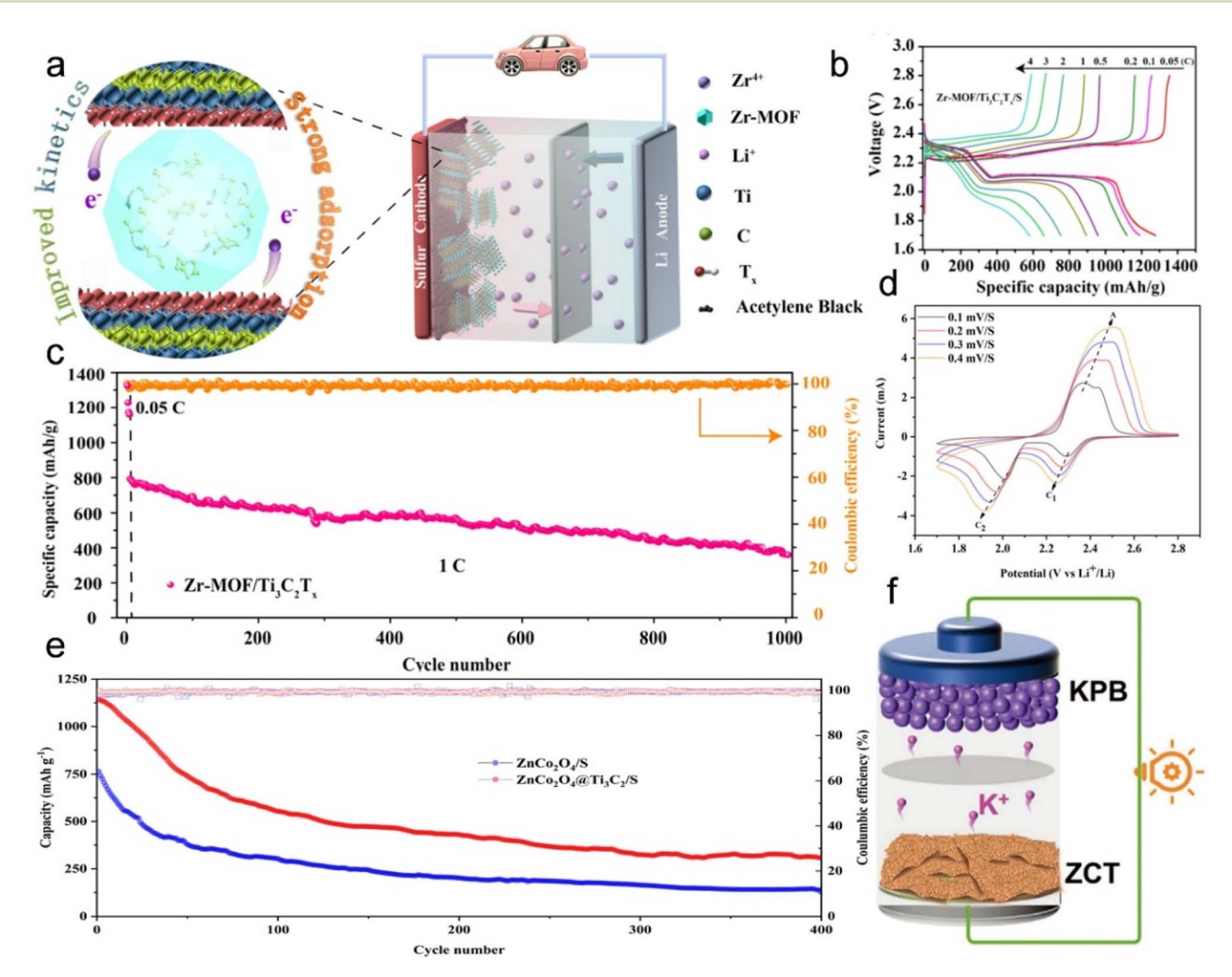


Fig. 15 (a) The working mechanism of the Zr-MOF/Ti₃C₂T_x/S in LSBs. (b) Charge/discharge voltage profiles of the Zr-MOF/Ti₃C₂T_x. (c) Cycle performance of the Zr-MOF/Ti₃C₂T_x at 1C. (d) CV curves of ZnCo₂O₄@Ti₃C₂/S. (e) Cycling performance for ZnCo₂O₄@Ti₃C₂/S cathodes at 0.5C. (f) Schematic illustration of KPB||ZCT full cells. (a–c) Reproduced with permission. ¹⁷⁷ Copyright 2021, American Chemical Society. (d and e) Reproduced with permission. ²⁴⁴ Copyright 2021, Elsevier. (f) Reproduced with permission. ²⁶⁸ Copyright 2022, Wiley.

corresponding data visualization provided in Fig. 15e. The CV curves analysis across scanning rates (0.1–0.4 mV s $^{-1}$), as depicted in Fig. 15d, confirmed the material's stable redox behavior. 244 Recent developments introduced the 45@ZnSeCoSe/MXene/S composite as a high-performance cathode candidate for LSB systems. Comprehensive electrochemical characterization demonstrated multiple superior attributes: a substantial initial capacity of 1198.5 mA h g $^{-1}$ at 0.1C, robust rate capability maintaining 489.8 mA h g $^{-1}$ at 2C, along with exceptional cycling stability and electrochemical reversibility. These collective properties significantly enhance sulfur redox kinetics, positioning this material as a promising solution for durable LSB applications. 266

In addition to the previously discussed LIBs and LSBs, several other representative battery systems have been explored. For instance, Hu and co-workers demonstrated ZnTe an effective anode candidate for K⁺ storage, subsequently synthesizing the ZnTe@C/Ti₃C₂T_x (ZCT) nanohybrids.²⁶⁸ The ZCT exhibited a high capacity of 408.0 mA h g⁻¹ at 0.1 A g⁻¹ and superior longterm cycle ability (230.2 mA h g⁻¹ at 1.0 A g⁻¹ after 3500 cycles), making it a promising candidate for practical applications. Fig. 15f provides a schematic illustration of potassium Prussian blue (KPB)||ZCT full cells. Furthermore, Na et al. have highlighted the application of 3D MXene/ZnSe@NC as anode materials in KIBs. This innovative architecture exhibited enhanced electrochemical performance, maintaining a capacity retention of 238 mA h g⁻¹ at 0.5 A g⁻¹ through 1000 chargedischarge cycles, while delivering 110 mA h g⁻¹ under 2.0 A g⁻¹. ²⁶⁹ Concurrently, sodium-ion batteries (SIBs) have garnered as a cost-effective energy storage solution, benefiting from the abundant availability and versatile substitution characteristics of Na⁺-related materials, establishing it as a leading candidate to replace Li⁺-based systems in contemporary battery applications. Yang and co-workers successfully prepared Ti₃C₂-ZIF-67, which was utilized as microbial fuel cell anode material. This engineered interface significantly enhanced extracellular electron transport efficiency through optimized microorganism colonization and enhanced biodiversity preservation at the bioelectrode interface. These findings establish new paradigms for MXene-based nanomaterials in bioelectrochemical energy conversion systems. 127 Shi and co-workers reported the CoSe₂@C/MXene composite, which, when used as an electrode for SIBs, exhibited high cyclic stability and rate performance.265 CoFe₂O₄@carbon@alkalized Subsequently, the composite was found to reduce the diffusion pathways for both Li⁺ and Na⁺. As a negative electrode material for batteries, it demonstrated superior rate capability and high capacity retention, achieving a satisfactory rate performance of 149 mA h g⁻¹ at 5 A g⁻¹ and a discharge capacity of 130 mA h g⁻¹ at 1 A g⁻¹ even after 1000 cycles for SIBs.240 In parallel, the Co3C/ MXene@C electrodes were constructed, exhibiting exceptional energy storage characteristics including enhanced specific capacity and remarkable electrochemical activity. The optimized architecture enabled stable charge storage with capacity retention of 236 mA h g⁻¹ after 100 cycles for KIB, while SIB systems demonstrated 275.9 mA h g⁻¹ under identical cycling conditions. Particularly noteworthy were the high-rate

capabilities, with capacities maintaining 80.6 mA h g⁻¹ for KIBs and 105 mA h g⁻¹ for SIBs at 2000 mA g⁻¹. ³¹² In complementary research, Liu *et al.* developed a hierarchically structured CoPNC@Ti₃C₂T_x composite. Electrochemical evaluation revealed that this sandwich-type architecture achieved outstanding rate performance (147.8 mA h g⁻¹ at 2000 mA g⁻¹) along with unprecedented cycling stability, sustaining capacity retention exceeding 100% through 2000 continuous charge–discharge cycles. ²⁵⁵ Recently, Sun *et al.* ³¹⁴ developed zinc ion batteries (ZIBs) based on 3D cross-linked VO_x/V₂CT_x-MXene-x composite, the device delivers specific capacities of 336.39 mA h g⁻¹ and 213.06 mA h g⁻¹ at 1 A g⁻¹ and 10 A g⁻¹ with excellent rate performance, and an energy density of 356.27 Wh kg⁻¹ at 1280 W kg⁻¹.

3.2. Supercapacitors

SCs have emerged as promising candidates for next-generation energy storage devices due to their exceptional cycle longevity, fast charge/discharge capabilities, and sustainable characteristics. These distinctive advantages enable SCs to outperform conventional energy storage technologies including dielectric capacitors, fuel cells, and rechargeable batteries. 139 The implementation of MOF materials leverages their unparalleled structural versatility, adjustable nanoscale porosity, and expansive interfacial areas,70 while MXene demonstraties particular efficacy as an electrochemical substrate through its remarkable mechanical resilience and densely populated reactive sites.152 Therefore, the unique properties of MOF/MXene composites are crucial for SCs. 315,316 A comprehensive compilation of recent advancements in MOF/MXene composite research specific to SCs has been systematically organized in Table 2.

Early studies by Jia et al. engineered MIL-100(Fe)/Ti₃C₂T_x MXene electrodes for SCs. The nanospheres, embedded within MXene nanosheets, were able to store more ionic charge. The composite electrode exhibited a maximum energy density of 85.53 Wh kg⁻¹ coupled with 962.17 F g⁻¹ specific capacitance at 0.5 A g⁻¹.134 More recently, Ramachandran et al. successfully synthesized Co-MOF/Ti₃C₂T_x, which exhibited an ultra-high areal capacitance of 18.7 F cm⁻² and demonstrated good reversibility. This material was proposed as a novel binder-free electrode material for SCs. Fig. 16a presents the CV response of Co-MOF/ Ti₃C₂T_x@Ni at various scan rate. The cycling stability of Co-MOF@Ni and Co-MOF/Ti₃C₂T_x@Ni was comparatively analyzed through galvanostatic charge-discharge (GCD) measurements at 6 mA cm⁻², as illustrated in Fig. 16b. Notably, the Co-MOF/Ti₃C₂-T_x@Ni hybrid demonstrated enhanced electrochemical durability with 92.1% capacitance preservation after 3000 cycles. 139 Yang et al. fabricated MOF/MXene/NF-300 as electrode, which demonstrated superior performance (1 A g⁻¹, 2453 F g⁻¹). Notably, the prepared MOF/MXene/NF-300 electrode material showed exceptional electrochemical durability, maintaining 83.84% capacitance retention through 3000 cycles.151 Zhang et al. constructed a Ti₃C₂T_x/Ni-MOF-based SC achieving remarkable energy storage performance, with specific capacitance reaching 1124 F g⁻¹ at 1 A g⁻¹(Fig. 16c). This configuration maintained 62% capacity

Table 2 MOF/MXene-based materials for SCs

$\begin{array}{c ccccccccccccccccccccccccccccccccccc$	MOF/MXene-based materials	Surface area	Current density	Capacitance	Cycling performance (capacitance retention, cycle, current density)	Electrolyte	Ref.
$ \begin{array}{cccccccccccccccccccccccccccccccccccc$	Pure MOF/MXene						
$\begin{array}{cccccccccccccccccccccccccccccccccccc$	$MIL-100(Fe)/Ti_3C_2T_x$	$529.49 \text{ m}^2 \text{ g}^{-1}$	$0.5~{\rm A~g^{-1}}$		93%, 10000 , $0.5~{\rm A~g^{-1}}$	6 М КОН	134
$ \begin{array}{cccccccccccccccccccccccccccccccccccc$	$\text{Co-MOF/Ti}_3\text{C}_2\text{T}_x$	$14.012 \text{ m}^2 \text{ g}^{-1}$		18.7 F cm^{-2}		3 М КОН	139
Ni-ZiF-67-200/K-Ar-MXene	$Ti_3C_2T_x/Ni$ -MOF		$1~\mathrm{A~g}^{-1}$	$1124 \; \mathrm{F} \; \mathrm{g}^{-1}$	83.2% , 4000 , 10 A g^{-1}	6 М КОН	148
Ni-ZiF-67-200/K-Ar-MXene	MXene/Ni-MOF	$184 \text{ m}^2 \text{ g}^{-1}$			98%, 5000, 3 mA cm ^{-2a}	3 M KOH	70
$\begin{array}{llllllllllllllllllllllllllllllllllll$	Ni-ZIF-67-200/K-Ar-MXene	$549.78 \text{ m}^2 \text{ g}^{-1}$	0.5 A g^{-1}	$557C g^{-1}$	66% , 5000 , 2 A g^{-1}	6 M KOH	150
$\begin{array}{cccccccccccccccccccccccccccccccccccc$	$Ni-MOF/Ti_3C_2T_x$		0.5 A g^{-1}		85% , 1000 , 0.5 A g^{-1}	6 M KOH	152
Ni-MOF@MXene — 1 A g $^{-1}$ 1160.5 F g $^{-1}$ 52.2%, 10 000, 10 A g $^{-1}$ 3 M KOH 157 Ni-MOF/MXene — 1 A g $^{-1}$ 716.19 F g $^{-1}$ 724.29%, 2000, 5 A g $^{-1a}$ 11 M KOH 158 MXene/ZIF-8 — 0.5 A g $^{-1}$ 1279.5 F g $^{-1}$ 90.88%, 10 000, 5 A g $^{-1a}$ 1 M KOH 168 Ni-MOF@Ti ₃ C ₂ T _x 85 m 2 g $^{-1}$ 0.2 A g $^{-1}$ 154 F g $^{-1}$ 84%, 5000, 1 A g $^{-1}$ 1 M KOH 203 Ni/Co-MOF@Ti ₃ C ₂ T _x NH ₂ 129.22 m 2 g $^{-1}$ 0.5 A g $^{-1}$ 1924 F g $^{-1}$ 58.13%, 10 000, 5 A g $^{-1}$ 3 M KOH 186 NiCo-MOF/MXene 38.2 m 2 g $^{-1}$ 1 A g $^{-1}$ 176.5 F g $^{-1}$ 72.5%, 5000, 10 A g $^{-1}$ 2 M KOH 188 MXene/Ni/Co-MOF 11 m 2 g $^{-1}$ 1 A g $^{-1}$ 1 A g $^{-1}$ 58 m A h g $^{-1}$ 89%, 10 000, 1 A g $^{-1}$ 2 M KOH 189 MXene-FeCu-MOF — 3 mA cm $^{-2}$ 440 mA h g $^{-1}$ 93%, 5000, 15 mA cm $^{-2}$ 2 M KOH 193 Meso-CuZn-MOFs@Ti ₃ C ₂ T _x 72 m 2 g $^{-1}$ 0.2 A g $^{-1}$ 1028C g $^{-1}$ 68.9%, 10 000, 1 A g $^{-1}$ 3 M KOH 196 MnNi-MOF-MXene 251.77 m 2 g $^{-1}$ 1 A g $^{-1}$ 1285.5 F g $^{-1}$ 94.4%, 4000, 3 A g $^{-1}$ 3 M KOH 190 MOF composite/MXene 208 m 2 g $^{-1}$ 1.5 A g $^{-1}$ 2285.5 F g $^{-1}$ 94.4%, 4000, 3 A g $^{-1}$ 3 M KOH 120 Ca ₃ O ₄ @MXene 76.14 m 2 g $^{-1}$ 1.5 A g $^{-1}$ 732.5 F g $^{-1}$ 88.7%, 5000, 1 S m A cm $^{-2}$ 1 M KOH 218 MOF derivative/MXene 76.14 m 2 g $^{-1}$ 1.5 A g $^{-1}$ 732.5 F g $^{-1}$ 88.9%, 10 000, 10 A g $^{-1}$ 3 M KOH 120 Ca ₃ O ₄ @MXene 76.14 m 2 g $^{-1}$ 1.5 A g $^{-1}$ 732.5 F g $^{-1}$ 88.9%, 10 000, 2 A g $^{-1}$ 3 M KOH 223 MnO ₂ @Co ₃ O ₄ -PC@MXene 76.14 m 2 g $^{-1}$ 1 A g $^{-1}$ 732.5 F g $^{-1}$ 88.9%, 10 000, 5 A g $^{-1}$ 3 M KOH 253 MnO ₂ @Co ₃ O ₄ -PC@MXene 76.14 m 2 g $^{-1}$ 1 A g $^{-1}$ 732.5 F g $^{-1}$ 88.9%, 10 000, 5 A g $^{-1}$ 2 M KOH 253 MnO ₂ @Co ₃ O ₄ -PC@MXene 76.14 m 2 g $^{-1}$ 1 A g $^{-1}$ 475.4 m h h g $^{-1}$ 90.68%, 10 000, 2 A g $^{-1}$ 2 M KOH 253 MnO ₂ @Co ₃ O ₄ -PC@MXene Poly Poly Poly Poly Poly Poly Poly Poly	Ni-BDC/V ₂ CT _x /NF	$14.34 \text{ m}^2 \text{ g}^{-1}$	1 A g^{-1}	2453 F g^{-1}	83.84% , 3000 , 1 A g^{-1}	1 M KOH	151
Ni-MOF@MXene — 1 A g $^{-1}$ 1160.5 F g $^{-1}$ 52.2%, 10 000, 10 A g $^{-1}$ 3 M KOH 157 Ni-MOF/MXene — 1 A g $^{-1}$ 716.19 F g $^{-1}$ 724.29%, 2000, 5 A g $^{-1a}$ 11 M KOH 158 MXene/ZIF-8 — 0.5 A g $^{-1}$ 1279.5 F g $^{-1}$ 90.88%, 10 000, 5 A g $^{-1a}$ 1 M KOH 168 Ni-MOF@Ti ₃ C ₂ T _x 85 m 2 g $^{-1}$ 0.2 A g $^{-1}$ 154 F g $^{-1}$ 84%, 5000, 1 A g $^{-1}$ 1 M KOH 203 Ni/Co-MOF@Ti ₃ C ₂ T _x NH ₂ 129.22 m 2 g $^{-1}$ 0.5 A g $^{-1}$ 1924 F g $^{-1}$ 58.13%, 10 000, 5 A g $^{-1}$ 3 M KOH 186 NiCo-MOF/MXene 38.2 m 2 g $^{-1}$ 1 A g $^{-1}$ 176.5 F g $^{-1}$ 72.5%, 5000, 10 A g $^{-1}$ 2 M KOH 188 MXene/Ni/Co-MOF 11 m 2 g $^{-1}$ 1 A g $^{-1}$ 1 A g $^{-1}$ 58 m A h g $^{-1}$ 89%, 10 000, 1 A g $^{-1}$ 2 M KOH 189 MXene-FeCu-MOF — 3 mA cm $^{-2}$ 440 mA h g $^{-1}$ 93%, 5000, 15 mA cm $^{-2}$ 2 M KOH 193 Meso-CuZn-MOFs@Ti ₃ C ₂ T _x 72 m 2 g $^{-1}$ 0.2 A g $^{-1}$ 1028C g $^{-1}$ 68.9%, 10 000, 1 A g $^{-1}$ 3 M KOH 196 MnNi-MOF-MXene 251.77 m 2 g $^{-1}$ 1 A g $^{-1}$ 1285.5 F g $^{-1}$ 94.4%, 4000, 3 A g $^{-1}$ 3 M KOH 190 MOF composite/MXene 208 m 2 g $^{-1}$ 1.5 A g $^{-1}$ 2285.5 F g $^{-1}$ 94.4%, 4000, 3 A g $^{-1}$ 3 M KOH 120 Ca ₃ O ₄ @MXene 76.14 m 2 g $^{-1}$ 1.5 A g $^{-1}$ 732.5 F g $^{-1}$ 88.7%, 5000, 1 S m A cm $^{-2}$ 1 M KOH 218 MOF derivative/MXene 76.14 m 2 g $^{-1}$ 1.5 A g $^{-1}$ 732.5 F g $^{-1}$ 88.9%, 10 000, 10 A g $^{-1}$ 3 M KOH 120 Ca ₃ O ₄ @MXene 76.14 m 2 g $^{-1}$ 1.5 A g $^{-1}$ 732.5 F g $^{-1}$ 88.9%, 10 000, 2 A g $^{-1}$ 3 M KOH 223 MnO ₂ @Co ₃ O ₄ -PC@MXene 76.14 m 2 g $^{-1}$ 1 A g $^{-1}$ 732.5 F g $^{-1}$ 88.9%, 10 000, 5 A g $^{-1}$ 3 M KOH 253 MnO ₂ @Co ₃ O ₄ -PC@MXene 76.14 m 2 g $^{-1}$ 1 A g $^{-1}$ 732.5 F g $^{-1}$ 88.9%, 10 000, 5 A g $^{-1}$ 2 M KOH 253 MnO ₂ @Co ₃ O ₄ -PC@MXene 76.14 m 2 g $^{-1}$ 1 A g $^{-1}$ 475.4 m h h g $^{-1}$ 90.68%, 10 000, 2 A g $^{-1}$ 2 M KOH 253 MnO ₂ @Co ₃ O ₄ -PC@MXene Poly Poly Poly Poly Poly Poly Poly Poly	MXene@Ni-HHTP	_	0.5 A g^{-1}	416.6 F g^{-1}		3 M KOH	156
$ \begin{array}{cccccccccccccccccccccccccccccccccccc$	Ni-MOF@MXene	_	1 A g^{-1}	$1160.5 \; \mathrm{F \; g}^{-1}$	52.2% , 10000 , $10~{\rm A~g}^{-1}$	3 M KOH	157
$ \begin{array}{cccccccccccccccccccccccccccccccccccc$	Ni-MOF/MXene	_	1 A g^{-1}	$716.19 \; \mathrm{F \; g^{-1}}$	74.22%, 2000, 5 A g ^{-1a}	1 M KOH	158
$\begin{array}{c} \text{Ni/Co-MOF@Ti}_3\text{C}_2\text{T}_x\text{-NH}_2 & 129.22 \text{ m}^2\text{ g}^{-1} & 0.5 \text{ A} \text{ g}^{-1} & 1924 \text{ F} \text{ g}^{-1} & 58.13\%, 10000, 10\text{ A} \text{ g}^{-1} & 3\text{ M} \text{ KOH} & 186\text{NiCo-MOF/MXene} & 38.2 \text{ m}^2\text{ g}^{-1} & 1\text{ A} \text{ g}^{-1} & 1176.8 \text{ F} \text{ g}^{-1} & 72.5\%, 5000, 10\text{ A} \text{ g}^{-1} & 2\text{ M} \text{ KOH} & 188\text{MXene/Ni,Co-MOF} & 11\text{ m}^2\text{ g}^{-1} & 1\text{ A} \text{ g}^{-1} & 58\text{mA} \text{ h} \text{ g}^{-1} & 89\%, 10000, 1\text{ A} \text{ g}^{-1} & 1\text{ M} \text{ KOH} & 189\text{MXene/FeCu-MOF} & - & 3\text{ mA}\text{ cm}^{-2} & 440\text{ mAh} \text{ h} \text{ g}^{-1} & 93\%, 5000, 15\text{ mA}\text{ cm}^{-2} & 2\text{ M} \text{ KOH} & 198\text{MXene/FeCu-MOF} & 251.77\text{ m}^2\text{ g}^{-1} & 1\text{ A}\text{ g}^{-1} & 1028\text{C}\text{g}^{-1} & 68.9\%, 10000, 10\text{ A}\text{ g}^{-1a} & 3\text{ M} \text{ KOH} & 198\text{MNi-MOF-MXene} & 251.77\text{ m}^2\text{ g}^{-1} & 1\text{ A}\text{ g}^{-1} & 1028\text{C}\text{g}^{-1} & 68.9\%, 10000, 10\text{ A}\text{ g}^{-1} & 3\text{ M} \text{ KOH} & 198\text{MOF} \\ \textbf{MOF composite/MXene} & 251.77\text{ m}^2\text{ g}^{-1} & 1\text{ A}\text{ g}^{-1} & 285.5\text{ F}\text{ g}^{-1} & 94.4\%, 4000, 3\text{ A}\text{ g}^{-1} & 3\text{ M} \text{ KOH} & 120\text{CA@MIL-101(Cr)/MXene} & 208\text{ m}^2\text{ g}^{-1} & 1.5\text{ A}\text{ g}^{-1} & 2720\text{ F}\text{ g}^{-1} & 88\%, 5000, 7\text{ A}\text{ g}^{-1} & 3\text{ M} \text{ KOH} & 317\text{COFe}_2O_4/\text{Ti}_3C_2T_x & - & 0.2\text{ mA}\text{cm}^{-2} & 2467.6\text{ F}\text{ cm}^{-3} & 88.2\%, 10000, 1.5\text{ mA}\text{cm}^{-2a} & 1\text{ M}\text{Licl} & 238\text{MO}_2O_3O_3O_3O_3O_3O_3O_3O_3O_3O_3O_3O_3O_3O$	MXene/ZIF-8	_			90.88% , 10000 , 5 A g^{-1}	7 M KOH	168
NiCo-MOF/MXene $38.2 \mathrm{m}^2 \mathrm{g}^{-1}$ $1 \mathrm{A} \mathrm{g}^{-1}$ $1176.8 \mathrm{F} \mathrm{g}^{-1}$ $72.5\%, 5000, 10 \mathrm{A} \mathrm{g}^{-1}$ $2 \mathrm{M} \mathrm{KOH}$ $188 \mathrm{MXene/Ni,Co-MOF}$ $11 \mathrm{m}^2 \mathrm{g}^{-1}$ $1 \mathrm{A} \mathrm{g}^{-1}$ $58 \mathrm{mA} \mathrm{h} \mathrm{g}^{-1}$ $89\%, 10 000, 14 \mathrm{g}^{-1}$ $1 \mathrm{M} \mathrm{KOH}$ $189 \mathrm{MXene-FeCu-MOF}$ $ 3 \mathrm{mA} \mathrm{cm}^{-2}$ $440 \mathrm{mA} \mathrm{h} \mathrm{g}^{-1}$ $93\%, 5000, 15 \mathrm{mA} \mathrm{cm}^{-2}$ $2 \mathrm{M} \mathrm{KOH}$ $193 \mathrm{MSeo-CuZn-MOFs} \mathrm{gn}^{-1} \mathrm{Ge}^{-1}$ $0.2 \mathrm{A} \mathrm{g}^{-1}$ $404 \mathrm{F} \mathrm{g}^{-1}$ $88.7\%, 5000, 14 \mathrm{g}^{-1a}$ $3 \mathrm{M} \mathrm{KOH}$ $196 \mathrm{MnNi-MOF-MXene}$ $251.77 \mathrm{m}^2 \mathrm{g}^{-1}$ $1 \mathrm{A} \mathrm{g}^{-1}$ $1028 \mathrm{C} \mathrm{g}^{-1}$ $68.9\%, 10 000, 10 \mathrm{A} \mathrm{g}^{-1}$ $2 \mathrm{M} \mathrm{KOH}$ $198 \mathrm{MOF} \mathrm{composite/MXene}$ $208 \mathrm{m}^2 \mathrm{g}^{-1}$ $1.5 \mathrm{A} \mathrm{g}^{-1}$ $285.5 \mathrm{F} \mathrm{g}^{-1}$ $94.4\%, 4000, 3 \mathrm{A} \mathrm{g}^{-1}$ $3 \mathrm{M} \mathrm{KOH}$ $198 \mathrm{MOF} \mathrm{composite/MXene}$ $208 \mathrm{m}^2 \mathrm{g}^{-1}$ $1.5 \mathrm{A} \mathrm{g}^{-1}$ $2720 \mathrm{F} \mathrm{g}^{-1}$ $84\%, 10 000, -0 \mathrm{M} \mathrm{G}^{-1}$ $ -$	$Ti-MOF@Ti_3C_2T_x$	$85 \text{ m}^2 \text{ g}^{-1}$		154 F g^{-1}	84% , 5000 , 1 A g^{-1}	1 M KOH	203
NiCo-MOF/MXene $38.2 \mathrm{m}^2 \mathrm{g}^{-1}$ $1 \mathrm{A} \mathrm{g}^{-1}$ $1176.8 \mathrm{F} \mathrm{g}^{-1}$ $72.5\%, 5000, 10 \mathrm{A} \mathrm{g}^{-1}$ $2 \mathrm{M} \mathrm{KOH}$ $188 \mathrm{MXene/Ni,Co-MOF}$ $11 \mathrm{m}^2 \mathrm{g}^{-1}$ $1 \mathrm{A} \mathrm{g}^{-1}$ $58 \mathrm{mA} \mathrm{h} \mathrm{g}^{-1}$ $89\%, 10 000, 14 \mathrm{g}^{-1}$ $1 \mathrm{M} \mathrm{KOH}$ $189 \mathrm{MXene-FeCu-MOF}$ $ 3 \mathrm{mA} \mathrm{cm}^{-2}$ $440 \mathrm{mA} \mathrm{h} \mathrm{g}^{-1}$ $93\%, 5000, 15 \mathrm{mA} \mathrm{cm}^{-2}$ $2 \mathrm{M} \mathrm{KOH}$ $193 \mathrm{MSeo-CuZn-MOFs} \mathrm{gn}^{-1} \mathrm{Ge}^{-1}$ $0.2 \mathrm{A} \mathrm{g}^{-1}$ $404 \mathrm{F} \mathrm{g}^{-1}$ $88.7\%, 5000, 14 \mathrm{g}^{-1a}$ $3 \mathrm{M} \mathrm{KOH}$ $196 \mathrm{MnNi-MOF-MXene}$ $251.77 \mathrm{m}^2 \mathrm{g}^{-1}$ $1 \mathrm{A} \mathrm{g}^{-1}$ $1028 \mathrm{C} \mathrm{g}^{-1}$ $68.9\%, 10 000, 10 \mathrm{A} \mathrm{g}^{-1}$ $2 \mathrm{M} \mathrm{KOH}$ $198 \mathrm{MOF} \mathrm{composite/MXene}$ $208 \mathrm{m}^2 \mathrm{g}^{-1}$ $1.5 \mathrm{A} \mathrm{g}^{-1}$ $285.5 \mathrm{F} \mathrm{g}^{-1}$ $94.4\%, 4000, 3 \mathrm{A} \mathrm{g}^{-1}$ $3 \mathrm{M} \mathrm{KOH}$ $198 \mathrm{MOF} \mathrm{composite/MXene}$ $208 \mathrm{m}^2 \mathrm{g}^{-1}$ $1.5 \mathrm{A} \mathrm{g}^{-1}$ $2720 \mathrm{F} \mathrm{g}^{-1}$ $84\%, 10 000, -0 \mathrm{M} \mathrm{G}^{-1}$ $ -$	Ni/Co-MOF@Ti ₃ C ₂ T _x -NH ₂	$129.22 \text{ m}^2 \text{ g}^{-1}$	0.5 A g^{-1}		58.13% , 10000 , 10 A g^{-1}	3 М КОН	186
$\begin{array}{cccccccccccccccccccccccccccccccccccc$	NiCo-MOF/MXene	$38.2 \text{ m}^2 \text{ g}^{-1}$	1 A g^{-1}	$1176.8 \; \mathrm{F \; g}^{-1}$	72.5% , 5000 , 10 A g^{-1}	2 M KOH	188
$ \begin{array}{llllllllllllllllllllllllllllllllllll$	MXene/Ni,Co-MOF	$11 \text{ m}^2 \text{ g}^{-1}$	1 A g^{-1}	58 mA h g^{-1}	89%, 10 000, 1 A g ⁻¹	1 M KOH	189
$ \begin{array}{cccccccccccccccccccccccccccccccccccc$	MXene-FeCu-MOF	_		$440 \; \text{mA h g}^{-1}$		2 M KOH	193
$ \begin{array}{cccccccccccccccccccccccccccccccccccc$	Meso-CuZn-MOFs@ $Ti_3C_2T_x$					3 M KOH	196
$\begin{array}{cccccccccccccccccccccccccccccccccccc$	MnNi-MOF-MXene	$251.77 \text{ m}^2 \text{ g}^{-1}$	1 A g^{-1}	$1028 \mathrm{C} \ \mathrm{g}^{-1}$	68.9%, 10 000, 10 A g ⁻¹	2 M KOH	198
$ \begin{array}{cccccccccccccccccccccccccccccccccccc$	MOF composite/MXene						
$ \begin{array}{cccccccccccccccccccccccccccccccccccc$	$Ti_3C_2T_x/ZIF-67/CoV_2O_6$	$49.466 \text{ m}^2 \text{ g}^{-1}$		$285.5 \; \mathrm{F \; g}^{-1}$	94.4% , 4000 , 3 A g^{-1}	3 М КОН	120
$\begin{array}{cccccccccccccccccccccccccccccccccccc$	CA@MIL-101(Cr)/MXene	$208 \text{ m}^2 \text{ g}^{-1}$	1.5 A g^{-1}	2720 F g^{-1}	84%, 10 000, —	_	219
$ \begin{array}{cccccccccccccccccccccccccccccccccccc$	MOF derivative/MXene						
$\begin{array}{cccccccccccccccccccccccccccccccccccc$	Co ₃ O ₄ @MXene	$76.14 \text{ m}^2 \text{ g}^{-1}$	1 A g^{-1}	732.5 F g^{-1}	83%, 5000, 7 A g^{-1}	6 M KOH	317
$\begin{array}{cccccccccccccccccccccccccccccccccccc$	$CoFe_2O_4/Ti_3C_2T_x$	_	$0.2~\mathrm{mA~cm^{-2}}$	$2467.6 \; \mathrm{F} \; \mathrm{cm}^{-3}$	88.2%, 10 000, 1.5 mA cm ^{-2a}	1 M LiCl	238
$\begin{array}{llllllllllllllllllllllllllllllllllll$	MnO ₂ @Co ₃ O ₄ -PC@MXene-CNF	$230.24 \text{ m}^2 \text{ g}^{-1}$	1 A g^{-1}	$475.4 \text{ mA h g}^{-1}$	92.08% , 10000 , 2 A g^{-1}	2 M KOH	245
$\begin{array}{llllllllllllllllllllllllllllllllllll$	Co_9S_8 @MXene $@Bi_2O_3$	$73.57 \text{ m}^2 \text{ g}^{-1}$	1 A g^{-1}	$646.1 \; \mathrm{F \; g^{-1}}$	$86.8\%, 7000, 2 \text{ A g}^{-1}$	6 M KOH	251
$\begin{array}{llllllllllllllllllllllllllllllllllll$	MXene@NiCo ₂ S ₄	$53.92 \text{ m}^2 \text{ g}^{-1}$	1 A g^{-1}	$451.12 \text{ mA h g}^{-1}$	90.68%, 10 000, 5 A g^{-1a}	2 M KOH	273
$ \begin{array}{llllllllllllllllllllllllllllllllllll$	CoNi ₂ S ₄ /MXene/NF	_	1 A g^{-1}	$933C g^{-1}$	80.5% , 10000 , 10 A g^{-1a}	3 M KOH	318
$ \begin{array}{llllllllllllllllllllllllllllllllllll$	MXene-CoS				94%, 5000, 30 mA cm ⁻²	2 M KOH	275
MXene@PCNF $405.59 \text{ m}^2 \text{ g}^{-1} 1 \text{ A g}^{-1} 572.7 \text{ F g}^{-1} 96.4\%, 10000, 2 \text{ A g}^{-1} 3 \text{ M KOH} 319$	$MXene@CoSe_2/Ni_3Se_4\\$	$740.93 \text{ m}^2 \text{ g}^{-1}$		283 mA h g^{-1}	75%, 10000 , 5 A g^{-1}	3 М КОН	263
MXene@PCNF $405.59 \text{ m}^2 \text{ g}^{-1} 1 \text{ A g}^{-1} 572.7 \text{ F g}^{-1} 96.4\%, 10000, 2 \text{ A g}^{-1} 3 \text{ M KOH} 319$	GO/MXene@NiZrP	$48.89 \text{ m}^2 \text{ g}^{-1}$	1 A g^{-1}	2358 F g^{-1}		6 М КОН	260
	MXene@PCNF	$405.59 \text{ m}^2 \text{ g}^{-1}$	1 A g^{-1}		96.4%, 10 000, 2 A g^{-1}	3 М КОН	319
	MXene@cobalt hydroxide	$85.10 \text{ m}^2 \text{ g}^{-1}$	1 A g^{-1}	348.55 F g^{-1}	_	3 М КОН	320

^a Electrochemical properties measured in a two-electrode configuration, others in three-electrode configuration.

retention at 20 A g⁻¹. Further advancements were reported by Zheng et al. through MXene@Ni-MOF composites synthesis, attaining 979 F g⁻¹ specific capacitance at 0.5 A g⁻¹ with merely 2% capacity degradation after 5000 cycles. The electrochemical charge storage mechanism of this hybrid material is visually detailed in Fig. 16e.⁷⁰ Olatoye and co-workers introduced a novel Ni-ZIF-67 (NZ) composite architecture, followed by the development of NZ-R-2-200/K-Ar-MXene through surface modification of K-Ar-MXene with NZ-R-2-200 NPs. The fabricated asymmetric supercapacitor, employing NZ-R-2-200/K-Ar-MXene as positive electrode in combination with NPC/rGO negative electrode, demonstrated exceptional electrochemical performance. This configuration achieved specific energy and power values of 27.48 Wh Kg⁻¹ and 400 W kg⁻¹ respectively, while maintaining operational stability through 2000 cycles.¹⁵⁰ Fig. 16f depicts an all-solid-state asymmetric flexible SC assembled using a Ni-MOF/Ti₃C₂T_r nanocomposite as the cathode and activated carbon (AC) as the anode.152 The Ni-MOF//MXAC composite was electrochemically characterized in a 2 M KOH electrolyte under a two-electrode configuration. CV analysis at 30 mV s⁻¹ revealed capacitive performance of 536 F g^{-1} (1 A g^{-1} , 0-0.4 V) and 298 F g^{-1} (-1-0 V) for this electrode system. 153 In comparative studies, MXene/ZIF-8-4 hydrogel-based asymmetric supercapacitors achieved notable energy storage characteristics with 354.7 F g^{-1} at 0.5 A g^{-1} and 57.84 Wh kg^{-1} energy density at 0.628 kW kg^{-1} .168 Another system, Ni/Co-MOF@MXene-NH₂//AC configuration demonstrated enhanced energy storage metrics in three-electrode testing, delivering 1924 F g^{-1} at 0.5 A g^{-1} with sustained 98.1 Wh kg^{-1} at 600 W kg⁻¹, alongside exceptional cycling stability through 15 600 cycles. 186 The NiCo-MOF/MXene system exhibited superior charge storage capacity (1176.8 F g⁻¹ at 1 A g⁻¹) combined with 72.5% capacity retention after extended cycling, confirming its structural durability.188 MXene-FeCu-MOF//AC hybrids displayed remarkable electrochemical persistence, maintaining 89% initial capacity (440 mA h g⁻¹) through 10 000 operational cycles. 193

In the realm of MOF composites/MXene, Liu et al. strategically engineered 3D hollow-structured Ti₃C₂T_x/ZIF-67/CoV₂O₆ hybrids through the synergistic integration of ZIF-67 and

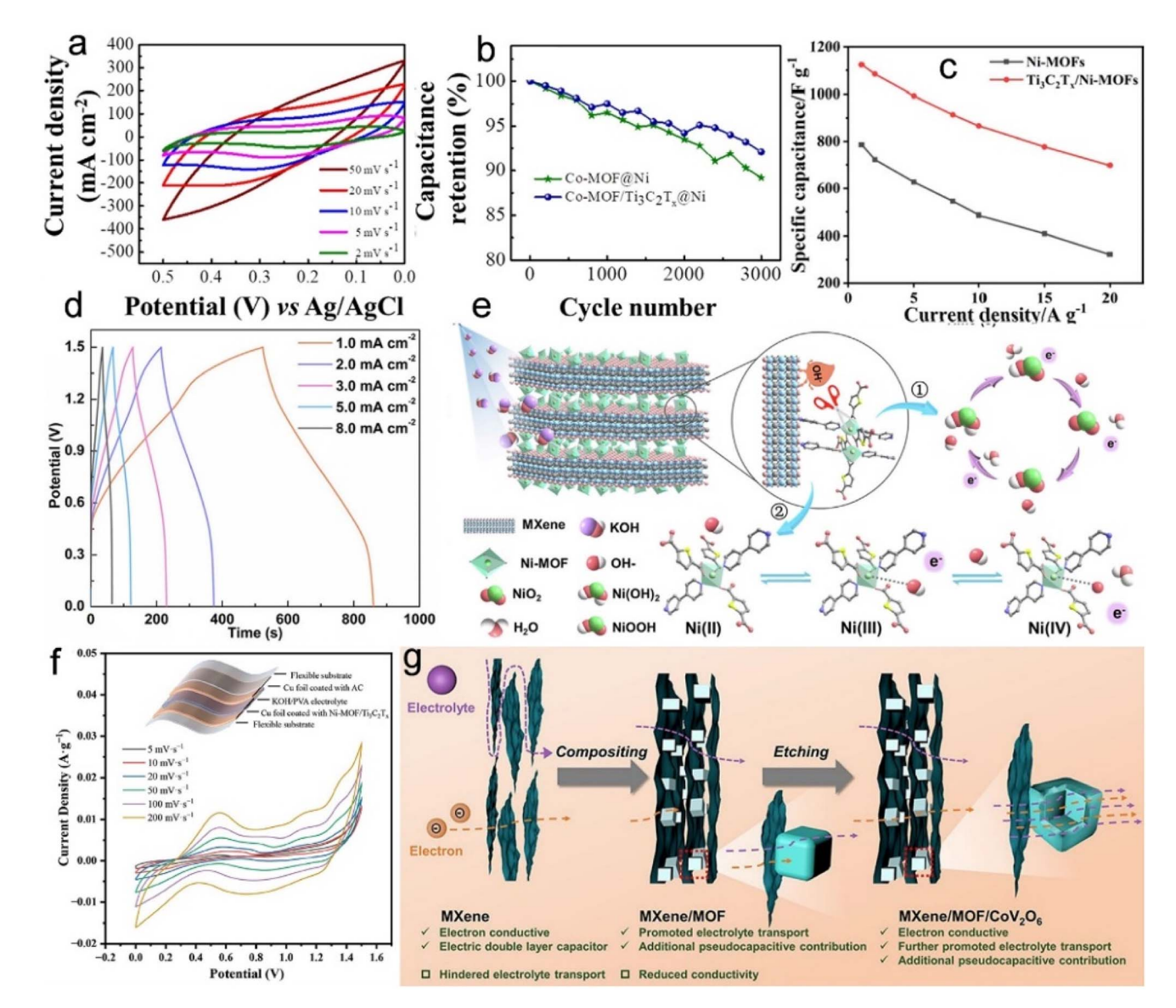


Fig. 16 (a) CV curves of Co-MOF/Ti₃C₂T_x@NF at different scan rates. (b) Capacitance retention of Co-MOF@NF and Co-MOF/Ti₃C₂T_x@NF. (c) Rate performance of Ti₃C₂T_x/Ni-MOF. (d) GCD curves of MXene@Ni-MOF. (e) The charge/discharge mechanism of MXene@Ni-MOF. (f) Schematic illustration of flexible SC and the CV curves of Ni-MOF/Ti₃C₂T_x//AC device. (g) Schematic of electrolyte/electron transport in Ti₃C₂T_x. $T_{i_3}C_2T_x$ /ZIF-67 and hollow Ti₃C₂T_x/ZIF-67/CoV₂O₆ electrodes. (a and b) Reproduced with permission. Copyright 2018, Elsevier. (c) Reproduced with permission. Copyright 2021, Elsevier. (d and e) Reproduced with permission. Copyright 2022, Elsevier. (f) Reproduced with permission. Multidisciplinary Digital Publishing Institute. (g) Reproduced with permission. Copyright 2023, Wiley.

 $Ti_3C_2T_x$ /ZIF-67. Electrochemical evaluations revealed that the optimized composite electrode exhibited a specific capacitance of 285.5 F g⁻¹, a significant increase compared to that of the ZIF-67 and $Ti_3C_2T_x$ /ZIF-67 electrode. The schematic representation in Fig. 16g illustrates electron/electrolyte transport pathways within $Ti_3C_2T_x$ -based electrodes.¹²⁰

In the field of MOF derivatives/MXene composites, Xie and colleagues fabricated a porous Co–Fe oxide nanorod derived from ${\rm Ti_3C_2T_x}$ -supported MOF. This innovative design enabled the fabrication of fully pseudocapacitive flexible supercapacitors with enhanced energy storage characteristics. The optimized composite exhibited outstanding electrochemical performance in 1 M LiCl electrolyte, achieving a high volumetric

capacitance of 2467.6 F cm⁻³. The flexible energy storage device maintained 88.2% initial capacitance after 10 000 cyclic operations, demonstrating remarkable durability.²³⁸ Kshetri *et al.* engineered multifunctional composite electrodes through an innovative integration strategy: capacitive-type Co-PC@MXene-CNF paired with battery-type MnO₂@Co₃O₄-PC@MXene-CNF. This configuration enabled their flexible wearable hybrid SC to achieve 72.5 Wh kg⁻¹ energy density at 832.4 W kg⁻¹, while demonstrating exceptional cyclic stability with >90.36% capacity preservation.²⁴⁵ In a parallel advancement, Wu *et al.* synthesized a Ti₃C₂@Co₃O₄/ZnO composite. When paired with AC cathodes in Li-ion hybrid capacitors, the system exhibited remarkable energy storage characteristics: 196.8 Wh kg⁻¹ at

RSC Advances Review

174.9 W kg⁻¹, sustaining 87.5Wh kg⁻¹ even under high-power conditions (3500 W kg⁻¹). The device maintained 75% capacitance retention after 6000 cycles at 2 A g⁻¹, confirming its electrochemical durability.246 Wang et al. synthesized Co₉S₈-2@MXene@Bi₂O₃ composite, which exhibited long-term cyclic stability and high discharge capacitance (646.1 F g⁻¹ at 1 A g⁻¹), these enhanced electrochemical properties were attributed to the unique core-shell architecture and optimized interfacial interactions between MXene and Bi₂O₃.²⁵¹ In contrast, Yang et al. fabricated a hierarchically structured MXene@CoSe2/ Ni₃Se₄ with honeycomb morphology, delivering 283 m Ah g⁻¹ capacity at 1 A g⁻¹ while maintaining 80% initial capacity after 5000 cycles, thereby establishing new benchmarks for SC energy storage systems.263 Meanwhile, MXene-CoS hybrids derived from MOFs have emerged as promising alternatives, leveraging their mesoporous structure (447 mA h g⁻¹ at 3 mA cm⁻²) with enhanced ion transport pathways and surface reactivity. 275 Most recently, Hussain et al.321 reported a novel NH4+ hybrid SC, assembled by Co-MOF@MXene carbonized nanofibers (MXCNF) cathode constructed by Co-MOF nanoflowers hydroanchored on MXCNF through thermally integrated electrospinning-carbonization synthesis, and a MXCNF anode. The architecture leveraged vertically aligned MXene cores for enhanced electrical conduction, complemented by homogeneously dispersed Co-MOF surface modifications that optimized redox-active surface utilization. This configuration achieved remarkable electrochemical performance, delivering 41.5 mW h kg⁻¹ at 800 mW kg⁻¹ power output while maintaining 87% cyclic stability over 16 000 cycles.

3.3. Sensors

MOF/MXene-based materials are extensively utilized in the realm of sensing.322,323 Table 3 provides a comprehensive summary of MOF/MXene-based materials for sensors.

A novel electrochemical approach for As(III) monitoring was developed by Xiao et al., utilizing a Fe-MOF/MXene compositemodified GCE. Fig. 17a illustrates the operational mechanism of adsorption-enhanced As(III) quantification through square wave anodic stripping voltammetry (SWASV). Experimental results indicate that the synergistic interaction between Fe-MOF nanostructures and MXene substrates significantly enhances both the preconcentration efficiency of As(III) and the electrochemical detection sensitivity, outperforming the individual components. This sensor has been successfully applied to the determination of As(III) in real water samples. Fig. 17b presents the SWASV responses of the Fe-MOF/MXene-1.5/GCE in 0.1 M PBS electrolyte containing progressively increasing concentrations of As(III). A linear relationship between electrochemical signals and analyte levels is demonstrated in the inset through current-concentration calibration curves. 133 Wang et al. successfully applied TiO₂/Ni-NC in detecting Hg²⁺, demonstrating good catalytic activity for the electrochemical reaction of Hg²⁺.324 Subsequently, Cheng et al. constructed a H₂O₂sensitive electrochemical platform based on Cu-MOF/MXene/ GCE. Chronoamperometric analysis at -0.35 V revealed a wide detection range (1 μ M-6.12 mM). The sensor displayed

ultrahigh sensitivity, rapid response kinetics, and straightforward operational design, highlighting its strong potential for practical diagnostic applications. 129 Parallel research efforts addressed DA sensing requirements through innovative nanocomposite design. Paul and co-workers engineered a MOF-Ti₃C₂ hybrid system combining Zn-based MOF ([Zn₄(1,2,4,5-benzenetetra carboxylate)₂ $(H_2O)_6$ _n·3nH₂O) with MXene substrates for redox-active DA quantification. Optimized conditions established linear current-concentration correlations (90-300 nM) via differential pulse voltammetry, achieving detection thresholds between 90-130 nM through enhanced anodic peak amplification.130 MOF/MXene-based composites have further expanded biosensing applications: Ti₃C₂T_x/ZIF-8 composites enabled hydrazine monitoring169 and HIV-1 protein,170 with mechanistic illustrations provided in Fig. 17c. Notably, a Ce-MOF/MXene assembly was developed as a selective L-Trp detector, maintaining stable performance across 10-50 μM concentrations (Fig. 17d).200 Furthermore, Ravipati et al. engineered an innovative MOF-71/V2C MXene hydrogel using solvothermal synthesis followed by lyophilization, establishing this nanocomposite as a precision biosensor for dual-analyte quantification of levothyroxine (LT4) and carbamazepine (CBZ).325 The developed sensor demonstrated exceptional analytical performance with extended linear response ranges spanning 10 nM to 100 μM (LT4) and 10 nM to 500 μM (CBZ), coupled with excellent selectivity and remarkably low detection thresholds of 5.6 nM (LT4) and 6.7 nM (CBZ). Owing to its intrinsic adaptability, the hydrogel showed applicability in flexible electrochemical wearables, creating new opportunities for biomedical sensor development.

Recent advances in MOF composite/MXene architectures have demonstrated remarkable versatility in self-powered biomotion and tactile sensing applications. A prominent example is the Ecoflex@Co-NPC@MXene developed by Rana et al., which has been successful implementation in self-powered biodynamic detection systems.216 This innovative configuration employs a hierarchical nanocomposite as a chargeenhancement layer in TENG, achieving a fourfold amplification in power generation efficiency compared to conventional designs. The structural architecture of this single-electrode TENG system is schematically illustrated in Fig. 17e. In the field of pathogen detection, the Zr-Fc MOF/AuNPs/4-MPBA sensing platform has emerged as a promising candidate for the ultrasensitive detection of E. coli O₁₅₇:H₇.²⁰⁹ The engineered MOF matrix capitalizes on its expansive surface topology to facilitate 4-MPBA through boronic acid-cis-diol interactions with bacterial lipopolysaccharides. This interaction enables signal labels to be fixed on the electrodes, forming a faradaic cage-type structure. The resulting sensor exhibits high sensitivity, excellent selectivity, and robust stability, highlighting its potential for real-world diagnostic applications. Given the significant health risks posed by pesticide residues, there is an urgent need to develop a sensitive and rapid method for pesticide monitoring. Addressing this critical demand for agrochemical monitoring, Tu et al.215 engineered a nanoengineered electrochemical sensing platform based on MXene/CNHs/β-CDMOFs for sensitive detection of carbendazim pesticide. The

This article is licensed under a Creative Commons Attribution-NonCommercial 3.0 Unported Licence. Open Access Article. Published on 29 August 2025. Downloaded on 12/3/2025 12:43:20 PM.

Table 3 MOF/MXene-based materials for sensors^a

MOF/MXene-based materials	Detection	Electrode	Linear ranges	Detection limits	Selectivity	Sensitivity	Ref.
Pure MOF/MXene Cu-MOF/MXene MOF-Ti ₃ C ₂ Fe-MOF/MXene MXene@MOF MXene/ZIF-8	H ₂ O ₂ DA AS(m) GPNMB N ₂ H ₄	GCE GCE GCE GCE	1–6120 µM 90–300 nM 1–10 ng L ⁻¹ – 10–7700 µM	0.35 µM 110 nM 0.58 ng L ⁻¹ 180.33 pg mL ⁻¹ 5.1 µM	AA, DA, UA, Glu AA, 5-AVA — AA, GSH, IgG, Glu, L-His NO3 -, SO4 ²⁻ , K', Cl ⁻ , DMF,	 8.94 μA ng ⁻¹ L¹ cm ⁻² 	129 130 133 165 169
Ti ₃ C ₂ T _x /ZIF-8 Ce-MOF/Ti ₃ C ₂ T _x MXene-NH ₂ @CeFe-MOF-NH ₂	HIV protein $_{\rm L^{*}}$ Trp $_{\rm Pb^{2+}}$, Hg ²⁺	GCE GCE	1 fM–1 nM 0.2–139 μM 5–50 nM, 1–35 nM	0.3 fM 0.19 µM 0.95 nM, 0.32 nM	ethanol, acrylic acid, 2-propanol BSA, PSA, AFP, CEA AA, DA, UA, L-Cys, Glu, KCl, NaCl Na ⁺ , K ⁺ , Ca ²⁺ , Fe ³⁺ , Ni ²⁺ , Mn ⁷⁺ , Mg ²⁺ , Al ³⁺ , Cl ⁻ , SO ₄ ²⁻	— 0.1556 µА µМ ⁻¹ сm ⁻² —, —	170 200 322
MOF composite/MXene Co-MOF-MXene@carbon black	Blood	I	10-800 μМ	0.005 µM	UA, urea, DA, GSH	$1.1~\mu{\rm A}~\mu{\rm M}^{-1}~{ m cm}^{-2}$	144
MXene/CNHs/β-CD-MOFs	creatinine Carbendazim	GCE	0.003-10.0 µМ	1.0 nM	Cl ⁻ , SO ₄ ²⁻ , Na ⁺ , Cu ²⁺ , Al ³⁺ , UA, AA, Glu, malathion, thiabendazole, Allocarbone for irreduction	$5.253~\mathrm{A~mol^{-1}L}$	215
Eu-MOF/PDA@MXene/Fe $_3$ O $_4$	TMAO	Magnetic	9×10^{-18} – 9×10^{-15} M	$1.25\times10^{-18}~\mathrm{M}$	Urea, Plasma	$63.73~\mu A~M^{-1}~cm^2$	223
MXene@PDA/MOF	L-Cys	GCE	$0.01-5 (10^{-6} \mathrm{M})$	$0.00374 (10^{-6} \mathrm{M})$	L-Arg, L-Leu, L-Trp, L-Phe,	I	224
rGO/PDA@MXene/FeCu-MOF	Ribavirin	GCE	I	0.053 nM	L'Mct, L'Asp, As, OA Lamivudine, sulfadiazine, inosine, uridine, DA, GSH, Glu	$1.43~\mu{\rm A~nM}^{-1}~{ m cm}^{-2}$	230
MOF derivative/MXene $In_2O_3/\Gamma i_3C_2T_x$ MXene	NH_3	Au	5–100 ppm	5 ppm	HCHO, CH ₃ OH, CH ₃ COCH ₃ ,	I	242
${ m In}_2{ m O}_3/{ m ZnO/Ti}_3{ m C}_2{ m T}_X$ MXene	Ethanol gas	I	2.15–10 ppm	I	C_2H_5OH , C_6H_6 , CO , NO_2 C_2H_5OH , CH_3OH , C_3H_6O , C_{11} N $_{11}$ C_{12} NI C_{11} N NO	I	243
Co ₃ O ₄ /Ti ₃ C ₂ T _x MXene MnO ₂ /Mn ₃ O ₄ @Ti ₃ C ₂ MXene/Au NPs	Ethanol gas Methamidophos	GCE	$^{-10^{-12}-10^{-6}}\mathrm{M}$	1 ppm $1.34 \times 10^{-13} \mathrm{M}$	C ₃ H ₉ IV, HCHCJ, NH ₃ , C ₆ H ₁₅ IV, NC ₂ CH ₃ OH, C ₃ H ₈ O, C ₃ H ₆ O, NH ₃ Glu, citric acid, NO ₃ ⁻ , SO ₄ ⁻ , PO ₃ ⁻ – C ₁ .2* $_{1}$ $_{2}$ $_{2}$ $_{2}$ $_{2}$ $_{3}$ $_{3}$	1 1	247 253
MXene-Cu/Cu ₂ O/C	Glu	Au	3-10 mM	1.70 mM	Lactose, fructose,	I	279
TiO ₂ /Ni-NC	${ m Hg}^{2+}$	GCE	0.001-10 µМ	Mu 67.0	Ca^{2+} , Pb^{2+} , Mn^{2+} , Zn^{2+} , Cd^{2+} , Cu^{2+}	I	324

^a AA: ascorbic acid; DA: dopamine; UA: uric acid; Glu: glucose; 5-AVA: 5-aminovaleric acid; L-Trp: L-tryptophan; L-Cys: L-cysteine; GPNMB: glycoprotein nonmetastatic melanoma protein B; GSH: glutathione; 1gG: human serum immunoglobulin G; L-His: L-histidine; TMAO: trimethylamine oxide; L-Arg: L-Arginine; L-Leu: L-leucine; L-Phe: L-phenylalanine; L-Met: L-methionine; L-Asp: L-asp: L-asp: L-Arginine; L-Arginine; L-Arginine; L-Arginine; L-Arginine; L-Arginine; L-Arginine; L-Phe: L-phenylalanine; L-Met: L-Metinethylalanine; L-Arginine; L-Argi

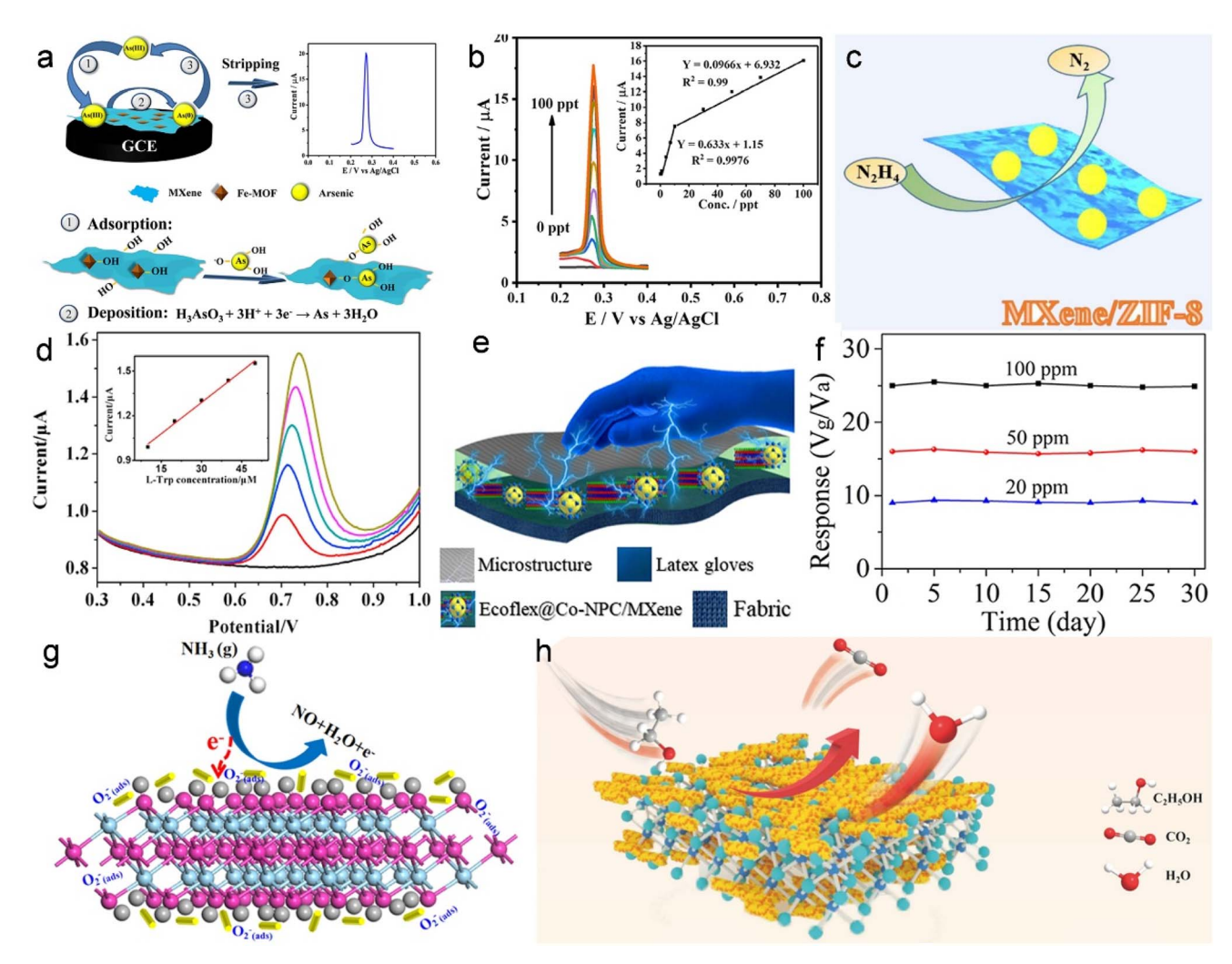


Fig. 17 (a) The schematic illustration of the adsorption-assisted As(III) detection on Fe-MOF/MXene/GCE by SWASV. (b) SWASV curves of the Fe-MOF/MXene/GCE in 0.1 M PBS solution with different As(III) concentrations. (c) Schematic illustration of N_2H_4 sensing. (d) differential pulse voltammetry curves of the Ce-MOF/Ti₃C₂T_x MXene/GCE. (e) Schematic of the single electrode Ecoffex@MXene@Co-NPC nanocomposite based TENG. (f) The long-term stability of self-powered MXene/CuO sensor. (g) Schematic diagram for the possible mechanism of $In_2O_3/Ti_3C_2T_x$ MXene composites toward NH₃. (h) Schematic diagram of the gas sensing mechanism of $In_2O_3/ZnO/Ti_3C_2T_x$ MXene-based sensor. (a and b) Reproduced with permission.¹³³ Copyright 2021, Elsevier. (c) Reproduced with permission.¹⁶⁹ Copyright 2021, Wiley. (d) Reproduced with permission.²⁵² Copyright 2022, Elsevier. (e) Reproduced with permission.²⁵³ Copyright 2021, American Chemical Society. (g) Reproduced with permission.²⁴⁴ Copyright 2022, Elsevier. (h) Reproduced with permission.²⁴⁵ Copyright 2023, Elsevier.

synergistic action of MXene/CNHs and β -CD-MOFs extends the linear range of the MXene/CNHs/ β -CD-MOFs electrode from 3.0 nM to 10.0 μ M, with a low detection limit of 1.0 nM (S/N = 3). The sensor demonstrates outstanding selectivity against common interferents, excellent reproducibility, and long-term operational stability, underscoring its practical applicability for on-site and routine monitoring of pesticide contaminants.

In the field of MOF derivatives integrated with MXene architectures, Song $et\ al.$ developed an innovative biosensing system by combining MnO₂/Mn₃O₄ with MXene/Au NPs hybrids for the detection of organophosphorus pesticides. This electrochemical platform exhibited exceptional analytical performance, demonstrating a broad detection window spanning six orders of magnitude ($10^{-12}\ M$ to $10^{-6}\ M$) and an

ultralow detection threshold of 1.34×10^{-13} M. The superior sensing characteristics stem from the collaborative interaction between the MnO₂/Mn₃O₄ and MXene/Au NPs composites, which collectively establish extensive active surfaces for electrochemical processes while preserving acetylcholinesterase functionality through favorable biocompatibility. These attributes position the platform as a highly promising tool for environmental monitoring and agricultural safety evaluation. ²⁵³ Regarding MXene/CuO, an organ-like gas sensor was developed for the detection of NH₃. The TENG-driven self-powered NH₃ sensor exhibited a strong response at room temperature (V_g/V_a = 24.8@100 ppm) and showed promise in monitoring pork quality. As depicted in Fig. 17f, the MXene/CuO hybrid sensor maintained consistent performance over time, confirming its

operational durability.252 Similarly, Liu et al. reported MOFderived In₂O₃/Ti₃C₂T_r MXene composites that achieved efficient NH₃ detection with strong linear correlation ($R^2 = 0.9785$) across 5-100 ppm concentrations. The architecture demonstrated rapid response and recovery dynamics (3/2 s), with Fig. 17g visually summarizing the proposed room-temperature sensing mechanism of these engineered nanomaterials.242 More recently, Co₃O₄/Ti₃C₂T_r nanocomposites with a mesoporous structure were synthesized by Bu and co-workers for ethanol sensing applications. The resulting sensor displayed excellent sensitivity, fast response and recovery kinetics, a low detection limit, high selectivity, and robust long-term stability, making it suitable for practical gas-sensing applications.247 Additionally, In₂O₃/ZnO/Ti₃C₂T_x MXene nanocomposites have been identified as a promising sensing material for ethanol detection, as depicted in Fig. 17h. These nanocomposites demonstrate a strong response to ethanol concentrations ranging from 2.15 to 10 ppm, along with outstanding selectivity towards ethanol gas.243 Furthermore, a novel wearable, stretchable multifunctional double-layer TENG has been developed, which combines the superior nanoporosity of NPCO with the charge capture and transport characteristics of MXene/ silicone. This TENG functions as a high-performance self-

3.4. Catalysts

10.4 W m⁻².250

Review

In light of rapid societal advancement, environmental pollution and escalating energy consumption have emerged as critical challenges threatening sustainable human development. Consequently, There is a growing demand for renewable energy and green energy sources within society. In response, an increasing number of researchers are dedicated to identifying viable, sustainable, and pollution-free solutions to address these urgent global issues. Among these efforts, catalysts-serving as the core tool of green chemistry, are becoming the key to break through the technical bottlenecks. This section systematically examines recent advancements in MXene/MOF composite catalysts and their electrocatalytic applications for energy conversion systems.

powered biosensor and delivers a high power density of

OER, HER, and ORR are three crucial reactions in the pursuit of sustainable energy.329,330 Among these, OER serves as a fundamental process in numerous renewable energy systems. Consequently, the search for cost-effective and efficient electrocatalysts to overcome the slow kinetics and high overpotential associated with OER is paramount.331 MOF materials have emerged as particularly attractive catalytic candidates owing to their customizable chemical properties, varied architectural features, and expansive active surfaces, positioning them at the forefront of catalyst innovation. Nevertheless, intrinsic limitations such as poor electrical conductivity and structural instability under operational conditions restrict their standalone performance. To address these challenges, researchers have strategically integrated MOFs with conductive MXene nanostructures, leveraging the excellent electron transport properties of MXenes to significantly enhance the overall

electrocatalytic activity of the hybrid systems.332,333 Notable examples include CoNi-ZIF-67@MXene MOF@MXene, representative MOF/MXene composites developed for OER applications. Wen et al. fabricated a Ti₃C₂T_r MXene-supported CoNi-ZIF-67 composite 67(aTi₃C₂T_r), demonstrating enhanced OER performance relative to pristine CoNi-ZIF-67, specifically achieving 275 mV onset potential versus RHE and a Tafel slope of 65.1 mV dec^{-1} . Comparative electrochemical metrics at 10 mA cm^{-2} are visually contrasted in Fig. 18a.132 Furthermore, Tan et al. developed a series of 2D MOF/MXene composites, in which the Co₂Ni-MOF layer is tightly anchored onto the MXene nanosheet, and the well-defined interface between the two layers facilitates the accelerated charge transfer kinetics during electrocatalytic operation. The OER performances of the Co₂Ni-MOF@MXene are depicted in Fig. 18b, while the Tafel curves of Co2Ni-MOF@MXene are presented in Fig. 18c. Among the series, Co2Ni-MOF@MXene-1 demonstrated superior electrocatalytic activity compared to other evaluated materials, achieving both the smallest Tafel slope (51.7 mV dec⁻¹) and minimal overpotential requirement (265 mV at 10 mA cm⁻²). These results indicate that electrostatically driven directional assembly is a viable and effective strategy for fabricating high-performance 2D OER catalysts. 187 In the realm of MOF derivatives/MXene, Zou et al. synthesized NiCoS/Ti₃C₂T_r hybrid demonstrating enhanced electrocatalytic performance. This improvement was attributed to the strong synergistic coupling between NiCoS and Ti₃C₂T_x, which facilitated improved charge carrier mobility and optimized electron transport pathways.272 Conversely, Du et al. investigated the influence of MXene incorporation on the OER activity of CoNi-MOF@MXene nanocomposites and observed an unexpected decrease in catalytic efficiency. This behavior was mechanistically attributed to the electron-donating nature of Ti₃C₂T_x MXene, which may alter the electronic structure of the active metal sites and suppress oxidative processes. 183 Furthermore, Hu's group successfully employed CoFe-LDH/ Ti₃C₂ as potential electrocatalysts for OER, achieving remarkable catalytic efficiency manifested by ultra-low overpotentials of 170 mV (10 mA cm⁻²) and 238 mV (100 mA cm⁻²).²⁷⁷ Fig. 18d presents free energy diagrams at 0 V for the OER on the surface of individual CoFe-LDH and CoFe-LDH/MXene composite. Additionally, MXene@MOF-Co2P composite material with engineered porosity demonstrated superior electrocatalytic behavior, requiring only 246 mV at 10 mA⁻² with accelerated kinetics evidenced by a 28.18 mV dec^{-1} Tafel slope. This performance enhancement arises from three synergistic effects: (1) heteroatom (C, N) doping-induced electronic modulation, (2) hierarchical pore networks preserved from MOF precursors, and (3) interfacial charge transfer between Co₂P and MXene components.257 HER significantly contributes to carbon mitigation strategies and net-zero emissions objectives. For instance, Zong et al. synthesized the MXene@MOF-CoP composite as a bifunctional catalyst. This innovative electrode configuration achieved notable hydrogen generation efficiency in diverse pH environments, particularly demonstrating 112 mV overpotential at pH = 14. The bifunctional activity based on MXene@MOF-CoP under alkaline conditions had a bias of

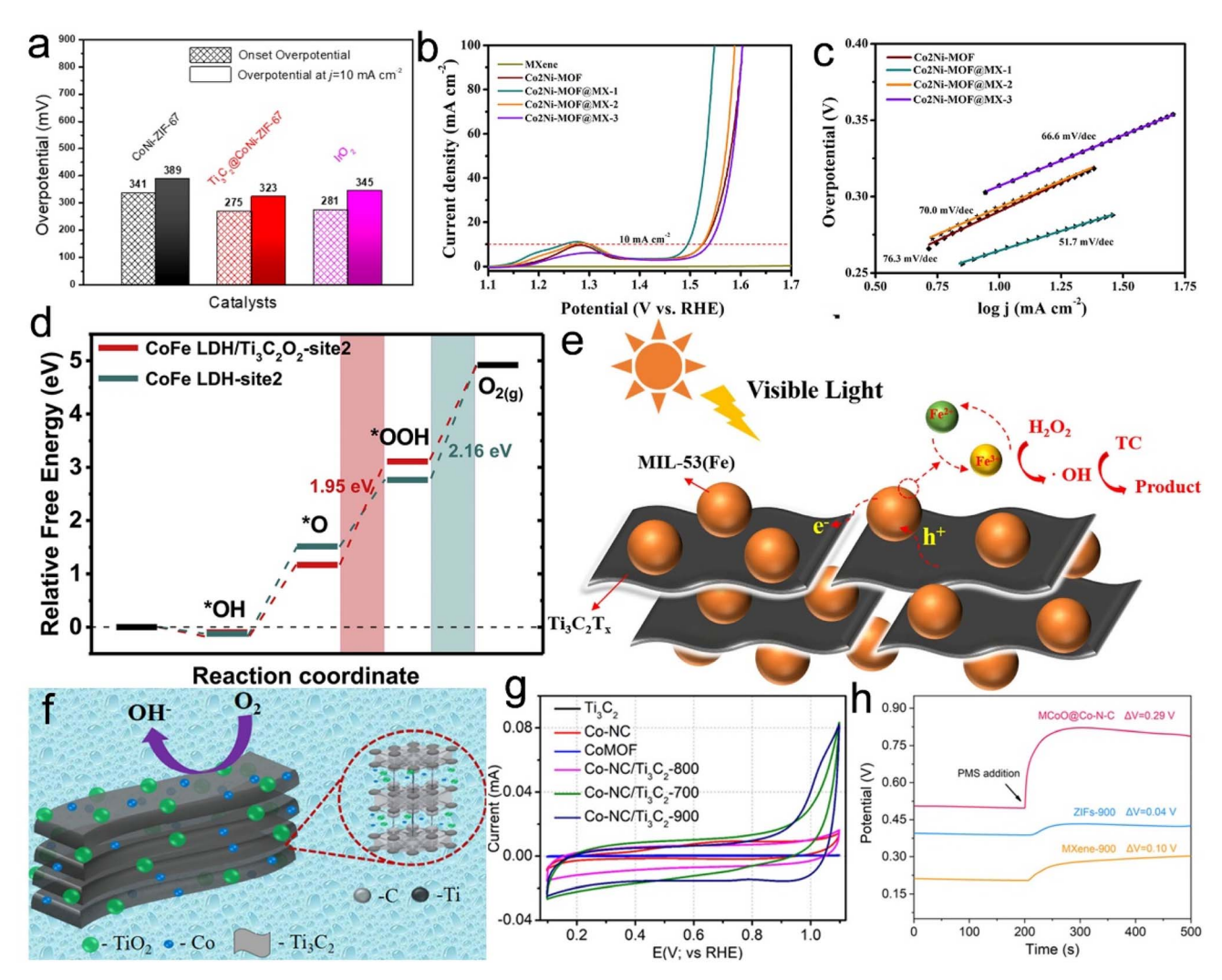


Fig. 18 (a) A comparison of the CoNi-ZIF-67 α Ti₃C₂T_x and CoNi-ZIF-67 catalysts in the onset potential and overpotential at 10 mA cm⁻². (b) LSV curves and (c) Tafel plots of Co₂Ni-MOF and Co₂Ni-MOF α MXene. (d) Free energy diagrams at 0 V for OER on the surface of individual CoFe LDH and CoFe LDH/Ti₃C₂O₂. (e) A schematic illustration of degradation of Ti₃C₂T_x over Ti₃C₂T_x/MIL-53(Fe) composite under visible light irradiation. (f) A schematic illustration of electroreduction of oxygen over Co-NC/Ti₃C₂-800. (g) Comparative CV curves for the Co-NC/Ti₃C₂ composites. (h) Variation of open circuit potential for MXene-CoO α Co-N-C, ZIF, and MXene catalysts. (a) Reproduced with permission.¹³² Copyright 2019, Multidisciplinary Digital Publishing Institute. (b and c) Reproduced with permission.¹⁸⁷ Copyright 2022, Elsevier. (d) Reproduced with permission.²³² Copyright 2021, American Chemical Society. (h) Reproduced with permission.³³⁴ Copyright 2022, Elsevier.

1.61 V at 10 mA cm $^{-2}$. The catalyst prepared using the MXene@MOF-CoP electrode exhibited excellent catalytic stability. 256 Similarly, $\mathrm{Ti_3C_2T_x@ZIF-8}$ catalyst developed by Hao *et al.* emerges as a viable alternative to expensive Pt-based catalysts, owing to its structural adaptability, enhanced conductivity, and expanded surface characteristics. CV measurements indicate an electrochemical active surface area of 122.5 cm 2 for this material, implying sustained operational stability through extended testing periods. 175 In energy conversion systems, ORR is a critical electrochemical process. Research by Parse *et al.* highlights the exceptional ORR catalytic behavior of Co-NC/ $\mathrm{Ti_3C_2}$ -800 composite, achieving an onset potential (E_{onset}) of 1.04 V with current density reaching 4.8 mA cm $^{-2}$ and half-wave potential ($E_{\mathrm{1/2}}$) at 0.93 V. This performance enhancement originates from synergistic effects between the Co

REDOX center and the NC matrices that form conformal coatings on $Ti_3C_2T_x$ skeleton, establishing optimized electron transport pathways during redox processes. Concurrent surface oxidation generating TiO_2 on MXene substrates further improves reaction kinetics by facilitating mass transport, ultimately boosting catalytic efficiency.²³² A schematic illustration of the oxygen electroreduction mechanism on the Co-NC/ Ti_3C_2 -800 composite is provided in Fig. 18f, while Fig. 18g compares the CV responses of various catalysts in N_2 -saturated electrolyte.

Photocatalysts, which exhibit excellent catalytic abilities under visible light, play a crucial role in the degradation of numerous wastes. Liu *et al.* developed a novel Ti₃C₂–Fe composite demonstrating enhanced visible-light photocatalytic performance with exceptional operational stability.¹²⁶ Fig. 18e schematically illustrates the tetracycline decomposition

reactions.335

Review

mechanism over TiCFe-1 under visible light. Subsequently, Qin's group engineered a Ti₃C₂-QD/Ni-MOF architecture that achieved exceptional N2 reduction efficiency, generating 88.79 μmol g_{cat}⁻¹ h⁻¹ of NH₃. Addressing the environmental concerns associated with methylene blue (MB), Cheng et al. synthesized Ni-MOF/Ti₃C₂ composites, which exhibited superior activity for the photocatalytic degradation of MB. When Ti₃C₂ was loaded with 1.5% wt%, the activity increased nearly fourfold.147 MOF composites with high porosity and tunable bandgap energy (4.99 eV), combined with exceptional surface area characteristics, effectively enhance charge transport kinetics while suppressing photogenerated electron-hole recombination, demonstrating superior dye degradation capabilities in photocatalytic applications. 176 Zhu and co-workers developed a MXene/CuPMOF nanohybrid, which achieved efficient hydrogen evolution photocatalysis through optimized interphase connectivity.163 Other examples of the catalytic aspects of MOF/MXene composites include a novel hybrid material synthesized by the hybrid reaction of hust-1 and $Ti_3C_2T_r$ by Gu's group. The resulting hybrid material exhibited good catalytic performance, with a conversion rate of 76.7% in the ring-opening reaction of styrene's catalytic oxidation, significantly higher than the 23.1% achieved with pure hust-1, with full activity recovery maintained through six catalytic cycles. 159 Cheng et al. further engineered 2D/2D Ni-MOF/Ti₃C₂ heterostructures with conductive interfaces, showing 4-fold photocatalytic activity enhancement compared to pure Ni-MOF

at optimal 1.5% wt% Ti₃C₂ loading. 147 In electrocatalysis, Zhan

et al. synthesized nitrogen-doped MXene-supported carbon-

encapsulated CoP nanoarrays decorated with ultrafine Pt

nanoparticles. The synergistic interaction between lattice-

incorporated nitrogen, CoP, and Pt effectively mitigated CO

poisoning, stabilized Pt nanoparticles, and enhanced the

intrinsic activity of Pt active sites, resulting in superior

electrocatalytic performance for relevant energy conversion

Additionally, Li et al. developed a VCo-MOF@Ti₃C₂T_x demonstrating remarkable catalyst ymonosulfate (PMS) activation efficiency, achieving 96.14% ciprofloxacin (CIP, 20 mg L⁻¹) within 30 min using merely 5 mg catalyst. This enhanced performance stems from the material's dual functionality in PMS adsorption and activation processes.192 Furthermore, Guo's group engineered a MXene-CoO@Co-N-C heterostructure with sandwich-like architecture that maintained 100% bisphenol A degradation efficiency under hypersaline conditions (200 mM). The system achieved exceptional catalytic turnover (TOF = 8.64 min^{-1}) at low reagent concentrations (0.05 g per L catalyst + 0.1 g L^{-1} of PMS), representing a 22.5-fold enhancement over MOF-derived catalyst without MXene. Comparative open-circuit potential variations across catalyst types are illustrated in Fig. 18h. 334 This MXene-CoO@Co-N-C catalyst has been successfully employed to remove trace organic contaminants from brackish water using PMS, exhibiting robust decontamination efficacy even under high-salinity environments.334 Additionally, the TS-V2CTx/ CoV₂O₆ HN hybrid demonstrates enhanced electrocatalytic performance in both HER and OER. The MOF-derived CoV2O6 nanocubes possess hollow architectures that optimize electrolyte infiltration while promoting efficient charge transfer kinetics. When configured as a water splitting module, this heterostructure achieves stable current output at 10 mA cm⁻² with a low battery voltage of 1.358 V.249

3.5. Electromagnetic/microwave absorption

Growing environmental challenges, particularly pervasive air pollution, have spurred intensive research into advanced adsorbent materials. Parallel demands exist for electromagnetic pollution mitigation, driving the need for lightweight broadband EMW absorbers. MOF/MXene-based materials play a pivotal role in advancing critical technological applications. The results of the latest studies on electromagnetic/microwave absorption are summarized in Table 4.

Table 4 MOF/MXene-based materials for electromagnetic/microwave absorption

MOF/MXene-based materials	$\mathrm{EAB}^a/\mathrm{GHz}$	Thicknesses/mm	$\mathrm{RL}^b/\mathrm{dB}$	Ref.
Electromagnetic absorption				
Ti ₃ C ₂ T _x /CNTs/Co	6.10	1.40	-85.80	234
$NiSe_2$ - $CoSe_2$ @ $C/Ti_3C_2T_x$	5.68	2.60	-60.46	262
Co/TiO ₂ -C	9.00	2.00	-41.10	285
Fe&TiO ₂ @C	6.50	1.60	-51.80	286
$Ti_3C_2T_x$ @CoFe@ TiO_2	5.02	1.40	-62.90	239
Co/Nb ₂ CT _x /carbon	4.00	1.67	-60.25	288
CoPC/CNTs@MXene	5.60	1.80	-10.00	258
CNCM-7	6.80	2.70	-65.30	284
Microwave absorption				
MXene/Co-CZIF 50%	10.20	2.70	-60.09	233
MXene/Ni-CZIF 50%	4.56	3.40	-64.11	233
MXene/1D N-CNTs	8.40	1.49	-57.78	282
MXene fibers/CoNi/C and CNTs/CoNi	4.50	1.60	-51.60	184
Ti ₃ C ₂ T _x /CNFs/TiO ₂ /CoNi	4.00	1.76	-54.60	235
Ni/TiO ₂ /C	3.40	1.50	-45.60	287

^a EAB: effective absorption bandwidth. ^b RL: reflection loss.

RSC Advances Review

High-performance EMW absorption materials with multifunctional properties have attracted considerable scientific and technological interest. Nevertheless, significant challenges remain in their development and optimization. Xiang et al. renanocomposite Ti₃C₂T_r/CNT/Co outstanding EMW absorption performance. The enhanced EMW capability originates from synergistic mechanisms, including charge carrier migration, dipolar polarization (both electric and magnetic), interfacial polarization effects, natural resonance phenomena, and optimized multi-path reflection configurations. As predicted, the engineered composite manifests outstanding absorption characteristics with a remarkable reflection loss value reaching -85.8 dB while maintaining an ultrathin profile of merely 1.4 mm.234 Similarly, Hou et al. prepared a device with a maximum RL of -60.46 dB at 2.6 mm

using a NiSe₂–CoSe₂@C Ti₃C₂T_x composite material with a mass fraction of Ti₃C₂T_x at 40 wt%. The RL <–10 db can reach 5.68 GHz (10.32–16 GHz). This innovative EMW absorption material derives its enhanced performance from two distinctive attributes: a hierarchically layered architecture and intrinsic metalloid characteristics. ²⁶² Additionally, Liao and co-workers synthesized a novel Co/TiO₂–C composite material through thermal treatment. This material exhibits superior microwave absorption characteristics, attaining optimal RL of –41.1 dB at 9.0 GHz (3.0 mm thickness) and –31.0 dB at 13.9 GHz (2.0 mm thickness). The operational bandwidth (RL ≤–10 dB) reached 3.04 GHz and 4.04 GHz at these frequencies, respectively. Comparative analysis with pristine MOF-derived carbon composites reveals three primary enhancement mechanisms: (1) multilayered microstructure-induced EMW scattering; (2)

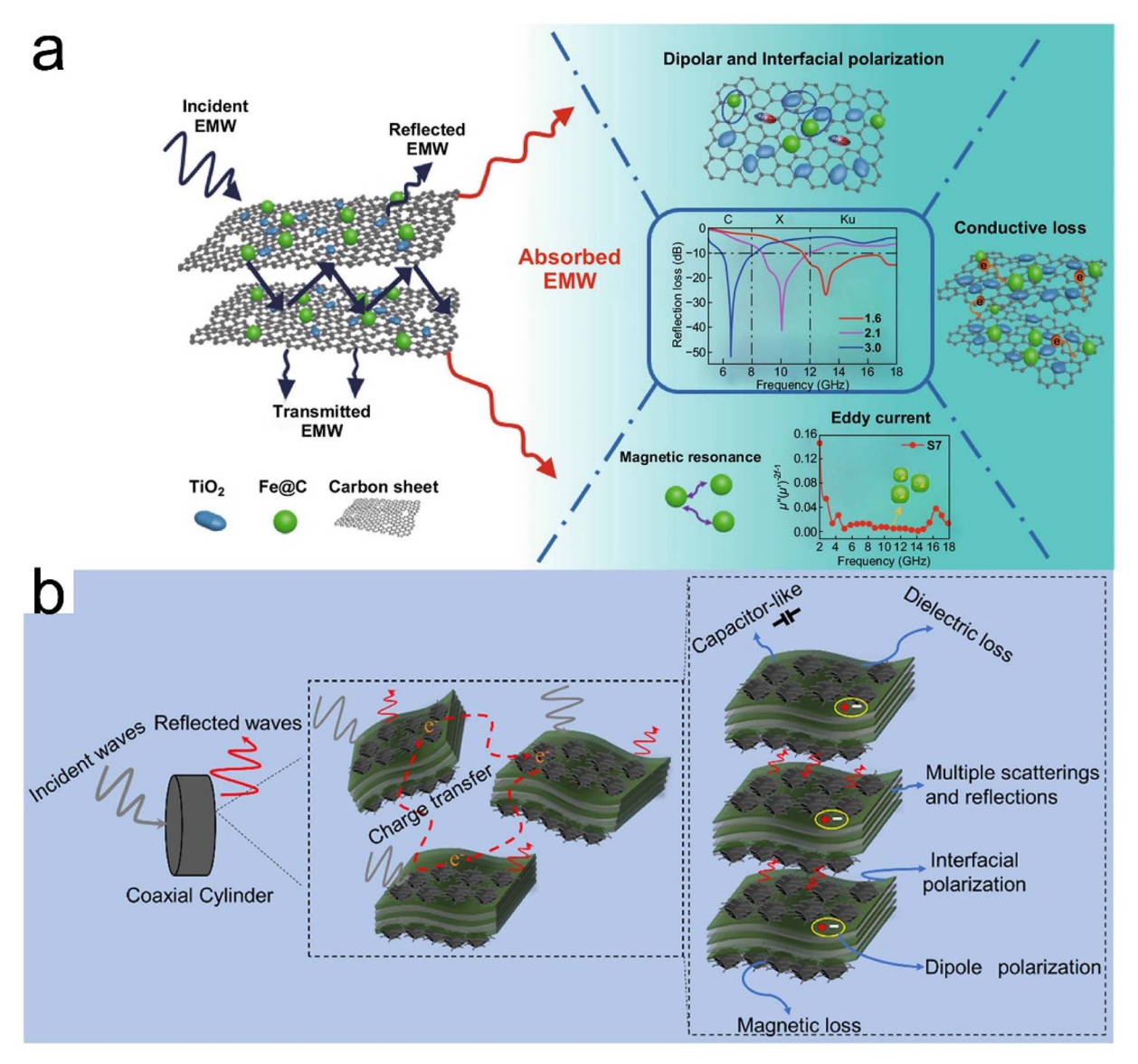


Fig. 19 (a) Illustration of EMW absorption mechanisms for Fe&TiO $_2$ @C nanocomposites. (b) Schematic illustration of the possible MA mechanism for MXene@Co-CZIF and MXene@Ni-CZIF. (a) Reproduced with permission. Copyright 2020, Springer. (b) Reproduced with permission. Copyright 2020, American Chemical Society.

interface/dipole polarization effects arising from heterojunctions, structural defects, and carbon matrix interactions; (3) improved dielectric dissipation through optimized electrical conductivity. These attributes render the ${\rm Co/TiO_2-C}$ hybrid composite a promising candidate for electromagnetic absorption applications. ²⁸⁵

EMW absorbing materials play a crucial role in military and engineering applications, underscoring the pressing demand for advanced absorption solutions. Lei et al. developed a sandwich-like Ti₃C₂T_r-based nanocomposite that demonstrated superior EMW absorption properties, attaining -62.9 dB minimum RL at 1.2 mm thickness within 17.95 GHz spectrum. The material demonstrated 5.02 GHz EAB (12.74-17.76 GHz) when fabricated at 1.4 mm depth, highlighting its capability as a thin, broadband absorber for mitigating pervasive electromagnetic interference in modern electronic environments.²³⁹ In a related advancement, Deng et al. investigated an innovative 2D hybrid architecture incorporating Fe&TiO2 NPs within carbon matrices. As depicted in Fig. 19a, the composite achieved 6.5 GHz EAB absorption bandwidth at 1.6 mm thickness while demonstrating -51.8 dB peak attenuation at 6.6 GHz with 3 mm configuration, offering new perspectives for MXenederived nanomaterial synthesis.286 Employing a porous structural engineering approach, Cui et al. synthesized a porous Co/ Nb₂CT_x/CA composite. This composite, characterized by its low density (54.03 mg cm⁻³), superior reflection loss, and expansive effective absorption bandwidth (reaching -60.25 dB and 4 GHz, respectively) at an ultra-thin thickness of 1.67 mm and an ultralow filling content of 10 wt%, demonstrated a radar cross

section reduction value of 31.24 dB m⁻², suggesting promising potential for excellent thermal insulation and flame retardant properties.²⁸⁸ To develop efficient EMW absorbing materials with robust absorption capacity, Wang and colleagues synthesized the CoPC/CNTs@MXene (CCM) absorber through controlled pyrolysis of ZnCo-MOF precursors at 800 °C, followed by electrostatic self-assembly within the Ti₃C₂T_x matrix. Notably, the CCM-20 composite demonstrated exceptional EMW absorption at 5.56 GHz, achieving a minimum RL of -54.2 dB. More remarkably, the CCM-30 composite variant attained effective microwave attenuation (EAB <-10 dB) at 5.6 GHz with merely 1.8 mm thickness, attributed to its hierarchical 0D/1D/2D structure that enhances electromagnetic energy dissipation through synergistic scattering mechanisms.258

High-performance microwave absorbing materials featuring layered and 3D architectures with abundant interfacial structures can significantly enhance EMW absorption efficiency. Such structural designs also contribute to improved microwave absorption performance, particularly by broadening the effective absorption bandwidth. Han *et al.* fabricated advanced MXene@Co-CZIF and MXene@Ni-CZIF composites (Fig. 19b) through electrostatic self-assembly, achieving exceptional EMW attenuation. The MXene/Co-CZIF 50% variant displayed notable absorption capabilities, attaining a minimum RL of -60.09 dB at 7.36 GHz with 9.3 GHz effective bandwidth (RL <-10 dB). Meanwhile, the MXene/Ni-CZIF 50% counterpart exhibited superior performance metrics, registering a peak RL value of -64.11 dB at 5.12 GHz accompanied by a 4.56 GHz operational

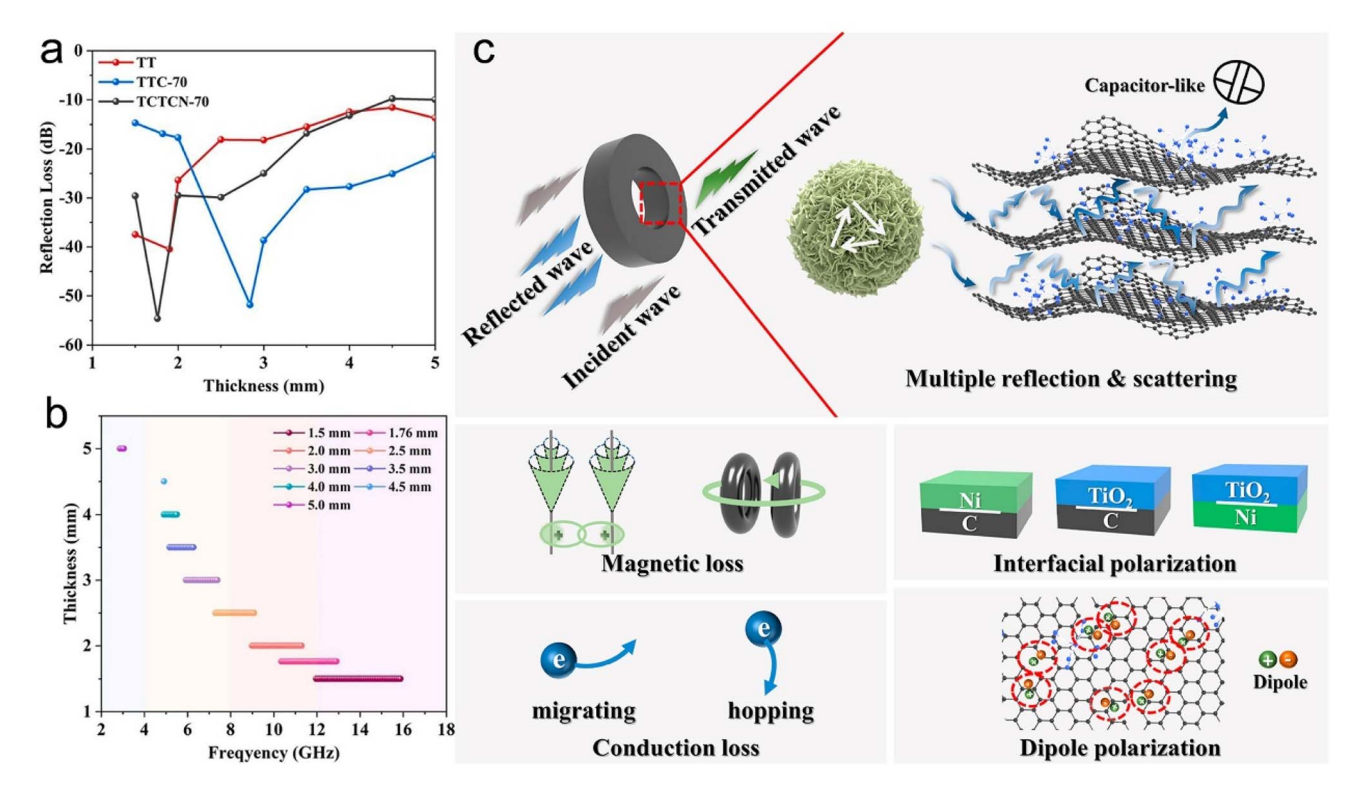


Fig. 20 (a) Dependence of the minimum RL values on the thickness and (b) EAB of $Ti_3C_2T_x/CNFs/TiO_2/CoNi$. (c) Schematic illustration of possible EMW absorption mechanisms for the Ni/TiO₂/C nanocomposites. (a and b) Reproduced with permission.²³⁵ Copyright 2022, Elsevier. (c) Reproduced with permission.²⁸⁷ Copyright 2022, Elsevier.

RSC Advances Review

bandwidth under equivalent threshold conditions. This methodology provides novel design principles for developing MOF-MXene hybrid absorbers with enhanced functionality.233 Furthermore, Liu et al. successfully synthesized a Ti₃C₂T_r/CNFs/ TiO₂/CoNi nanocomposite through electrostatic self-assembly and thermal treatment, demonstrating superior EMW absorption characteristics. In this architecture, Ni-catalyzed CNFs interconnect layered MXene substrates (originally employed for MOF anchoring) to establish an interconnected framework. This structural configuration enhances dielectric loss through the creation of extensive heterogeneous interfaces, while the incorporation of CoNi NPs introduces additional magnetic loss mechanisms, enabling balanced impedance matching and synergistic attenuation. With 40 wt% filler loading, the Ti₃C₂T_x/ CNFs/TiO₂/CoNi-70 composite achieves a RL of -54.6 dB and 4.0 GHz EAB at 1.76 mm thickness (Fig. 20a and b). This methodology advances microwave absorption material design through synergistic structural engineering.235 Despite its high electrical conductivity, 2D laminated Ti₃C₂T_x MXene suffers from an excessively high dielectric constant and a lack of magnetic loss, leading to significant impedance mismatch that restricts its practical application in EMW absorption. To tackle this challenge, Wang et al. successfully synthesized a multilayered Ni/TiO2/C nanocomposite. Remarkable enhancement in EMW absorption properties was observed through precision modulation of calcination parameters. As depicted in Fig. 20c, the optimized specimen treated at 700 °C exhibited exceptional absorption characteristics: a minimum RL of −45.6 dB, an EAB of 3.40 GHz (14.6-18.0 GHz), and ultra-thin 1.5 mm. This study establishes a novel pathway for developing high-performance MXene-derived electromagnetic absorbers through simplified synthesis protocols.287 Like other 2D materials, MXene are prone to severe aggregation and stacking issues that impede their applications. To overcome this issue, Wu et al. assembled a 1D heterostructure without the need for templates or rigid frameworks. The results indicated that the absorber attained a minimum RL of -51.6 dB at a matched thickness of 1.6 mm, with an EAB (RL <-10 dB) extending across 4.5 GHz within the 13.2-17.7 GHz frequency range. These findings advance the methodology for engineering efficient microwave absorption materials.184

3.6. Others

MOF/MXene hybrid systems exhibit dual functionalities that extend beyond the previously described chemical interactions, serving as highly effective flame-retardant additives with significant protective capabilities. For instance, Wan et~al. employed solvothermal synthesis to fabricate 3D flower-shaped Ni-MOFs while achieving functionalization of multi-terminal layered ${\rm Ti_3C_2T_x}$. The engineered Ni-MOF@ ${\rm Ti_3C_2T_x}$ integration substantially improved the flame-retardant performance of TPU. Quantitative analysis revealed distinct combustion parameter reductions: TPU composites containing 2% Ni-MOF, 1% Ni-MOF@ ${\rm Ti_3C_2T_x}$, and 2% Ni-MOF@ ${\rm Ti_3C_2T_x}$ exhibited smoke production rate (SPR) reductions of 41.2%, 44.1%, and 35.3% respectively, along with corresponding total smoke

production decreases measuring 22.5%, 26.4%, and 23.0% relative to pure TPU. Mechanistic investigations identified three synergistic protective mechanisms: MXene's physical barrier formation, catalytic carbonization capability, and gaseousphase radical quenching, complemented by MOF-mediated enhancement of MXene dispersion efficiency, thermal resilience, and flame suppression effectiveness.128 To develop an eco-friendly flame-retardant system with multi-component synergy for polymer composites, Gong et al. synthesized a biomimetic MXene@Bi-MOF composite through interfacial engineering and integrated it into epoxy resin (EP). Experimental characterization revealed that the 2 wt% MXene@Bi-MOF modified EP composite exhibited superior fire safety performance compared to pristine EP, demonstrating significant reductions in key combustion parameters: 28.8% peak heat release rate, 45.3% peak smoke production rate, 36.5% total heat release, 30.7% peak CO emission, and 55.3% smoke factor. Additionally, the composite simultaneously achieved decreased char residue carbonization efficiency and reduced fire growth index, indicating enhanced flame inhibition mechanisms. This performance enhancement originates from the complementary interactions between MXene's catalytic carbonization capability and Bi-MOF's gas-phase radical trapping function during thermal degradation processes.199 In another effort to enhance the flame resistance of TPU, Wan and colleagues successfully synthesized ZIF-67@MXene and integrated it into TPU materials. Remarkably, even at a low loading of 0.5 wt%, the composite demonstrated substantial fire safety enhancements: a 26% reduction in peak heat release, 9% decrease in total heat emission, 50% suppression of maximum smoke generation, and 22% mitigation in both total smoke output and carbon monoxide formation relative to unmodified TPU.141 These improvements primarily stem from the hybrid material's barrier mechanism that effectively impedes combustion propagation within the polymer matrix.

Furthermore, MOF/MXene exhibits adsorption and sterilization properties.339 In the design of antibacterial platforms, Guo et al. developed an oxygen-enriched Schottky interface by partially substituting Zn coordination sites in Zn-MOF with Ti atoms derived from Ti₃C₂T_x nanosheets. This structural innovation facilitated superior separation efficiency and accelerated electron transfer of photogenerated charge carriers under 808 nm near-infrared illumination. The resulting Zn-MOF@Ti3C2Tx composite exhibited remarkable biocompatibility and multimodal antibacterial performance, showing promising therapeutic applications for Staphylococcus aureusinfected wound regeneration.172 Triazole fungicides, widely utilized in agriculture due to their high efficacy, broad-spectrum activity, and chemical stability, are the primary agents for controlling rice blast. To mitigate environmental concerns associated with triazole fungicide residues, Lu et al. fabricated a novel magnetic composite, Fe₃O₄@MXene@MOF-74, via a facile synthesis approach. Various analytical techniques were employed to characterize the morphology and properties of the fabricated composite, with its adsorption capabilities being methodically evaluated. In practical applications, satisfactory removal effects were achieved for paddy water samples.

Importantly, Fe₃O₄@MXene@MOF-74 exhibited notable antibacterial properties, achieving a 50% effective inhibitory concentration against Magnaporthe oryzae proliferation. These results underscore the composite's dual-functional capability in simultaneously removing pollutants and suppressing phytopathogens, positioning Fe₃O₄@MXene@MOF-74 as a promising candidate for agricultural water remediation. More recently, Zhu *et al.* synthesized MXene/Cu-MOF composites with varying MXene loadings (3.3%, 6.7%, and 13.3%) through an *in situ* precipitation method. Compared to pristine MXene and Cu-MOF, the optimized 3.3% MXene/Cu-MOF composite showed a significant improvement in the adsorption performance of methylbenzyl sulfide in model fuels, with an equi-

librium adsorption capacity reaching 87.4 mg g⁻¹.340

The continuous progress in science and technology has enabled the development of ion-based flexible actuators capable of sustained shape adaptation, offering a promising alternative to conventional rigid mechanical components. This innovation has generated considerable attention regarding their prospective utilization in emerging metaverse platforms and flexible robotic systems. In this regard, Garai et al. introduced a novel Ti₃C₂T_x electrode-anchored Mn-based MOF (MnBTC), which can be utilized for super-stable electro-ionic artificial muscles. The Ti₃C₂T_x-MnBTC composite nanostructure forms coordination bonds, hydrogen bonds, and hydrophilic interactions with the conductive polymer poly(3,4ethylenedioxythiophene) polystyrene sulfonate, resulting in an electrode with both mechanical flexibility and ionic activity. The Ti₃C₂T_x-MnBTC composite electrode ion actuator demonstrated a substantial bending displacement of 12.5 mm under 0.5 V at 0.1 Hz. It also exhibited an ultra-fast drive response time of 0.77 s at a DC input signal of 0.5 V, without any backlash phenomenon. Notably, the actuator maintained 98% long-term durability for over 43 200 seconds (≈12 h) at a frequency of 1 Hz, with no distortion of the electrodes. These findings highlight the viability of MXene-MOF hybrid constructs as foundational materials for next-generation biomimetic systems requiring both dynamic performance and operational longevity.309 More recently, Memon et al. developed MOF-808@MXene composites for use as triboactive materials in TENG, which exhibited a high triboelectric output of 296.22 V, 30.7 μ A, and 67.4 mW m⁻². Furthermore, the device was stable in repetitive cycles of 5000 and showed only 34% degradation after a duration of 10 weeks, thus making it suitable as a durable and long-lasting power source based on applications in microcircuit devices.341

In an effort to enhance the flux, antifouling, and dye separation properties of polyether-based membranes, Yao *et al.* developed mixed matrix membranes using polyether blends combined with ZIF-8@Ti $_3$ C $_2$ T $_x$. With a 3% microemulsion content, the membrane achieved an optimal flux of 280 L m $^{-2}$ h $^{-1}$ and demonstrated an antifouling performance with a 91% bovine serum albumin rejection rate. Notably, the membrane maintained a 140 L m $^{-2}$ h $^{-1}$ high flux in high-salinity wastewater, achieving a dye removal efficiency of up to 98% while only removing 5% of salt ions. To address the challenge of antifouling coating degradation and efficacy loss, Wang and his

collaborators successfully synthesized a novel MOF, MZ-8, based on mercaptobenzothiazole (MBT). By integrating MZ-8 with MXene nanosheets, they formulated an organic-inorganic nanocomposite, MZ-8/MXene, which was employed as a reinforcing filler in PU resin. The resulting MZ-8/MXene/PU coating exhibited reduced microbial adhesion due to photothermal effects, zinc ions release, and MBT presence, leading to over 99% reduction in surface-adherent bacteria and 93% in microalgae. This advanced coating system, combining robust antifouling performance with intrinsic self-healing capabilities, presents significant potential for applications in marine antifouling and biomedical devices.³⁴²

Li and colleagues successfully fabricated a 3D amidoximefunctionalized Ti₃C₂T_x/ZIF-67 structure that demonstrated a uranium extraction capacity of 2224.54 mg g^{-1} at 1 V. The material showed exceptional selectivity towards uranium, with a reusability rate of 63.51% after 10 cycles. Furthermore, Ti₃C₂T_x/ZIF-67 displayed nearly 100% bactericidal efficiency against Escherichia coli and Staphylococcus aureus, underscoring its superior antibacterial properties. Under an electric field, the uranium adsorption rate of Ti₃C₂T_x/ZIF-67 reached 11.40 mg g⁻¹ within 24 h, which is 5.3 times higher than that of physicochemical adsorption. This study presents a promising method for the efficient capture of uranium resources from seawater through electro adsorption. 142 Subas Kashif et al. 178 fabricated the UiO-66/MXene composite material via a solvothermal method. A series of studies have shown that the UiO-66/MXene composite exhibits removal rates of 98% for MB, 97% for rhodamine B, and 99% for tetracycline. The maximum adsorption capacities of UiO-66/MXene for MB, rhodamine B, and tetracycline are 312, 285, and 476 mg g⁻¹, respectively. These findings offer a promising outlook for the development of water-refining adsorbents. In another study, Deng et al. developed MXene nanosheets and ZIF-8 functionalized PU sponges (PU-Ti₃C₂T_r-MOF), resulting in excellent hydrophobicity and a water contact angle of 135°. The sponges demonstrated high adsorption capacities for liquid hazardous chemicals, absorbing up to 48-91 times their weight. Additionally, the materials exhibited excellent recyclability, retaining significant adsorption capabilities toward oils and organic solvents through five consecutive usage cycles. This study proposes a novel engineering approach for fabricating specialized polymeric sponges with significant promise for rapid response to accidental chemical spills.174

Navid Rabiee *et al.*¹⁷¹ conducted a study on an inorganic MXene/MOF-5 nanostructure for the co-delivery of drugs and genes. The results indicated a complete dose-dependency, with a significant decrease in relative cell viability observed as the treatment time extended from 24 h to 72 h, characterized by a pronounced slope. The chitosan-alginate bilayer coating approach significantly enhanced the mitigation efficiency of nanocarriers. To evaluate their dual delivery capability, the engineered nanosystems were functionalized with pCRISPR for simultaneous tracking and therapeutic assessment. Confocal microscopy analysis demonstrated effective pCRISPR internalization in both HEK-293 and HeLa cellular models, particularly evidenced by 26% elevation in green fluorescent protein signal

RSC Advances Review

intensity observed in HeLa populations. These findings suggest that this strategy, along with the optimized MXene/MOF-5 nanosystem, holds promise for further development in drug/ gene co-delivery applications in animal models. To address the challenge of efficiently treating bacterially infected wounds, Guo et al. developed a new oxygen-rich vacancy Schottky junction. This junction notably enhances the separation of photoinduced carriers and electron transfer kinetics under 808 nm near-infrared irradiation. The resulting Zn-MOF@Ti₃C₂T_x composite demonstrates remarkable biocompatibility along with multimodal antimicrobial efficacy against both Staphylococcus aureus and Escherichia coli, while promoting rapid wound healing post-Staphylococcus aureus infection, achieving a wound closure rate of 99%. 172 Acknowledging the limited availability of biosensors capable of detecting both chemical and biological signals, Lin et al. designed a multifunctional biosensor. The device integrates three functionalities: sweat-based electrochemical biosensing for UA/Glu monitoring, electrophysiological signal recording, and electrostimulation therapy delivery. Additionally, they fabricated a MOF/MXene electrode suitable for electrical muscle stimulation therapy. This research underscores its considerable potential in muscle therapy and daily noninvasive monitoring, while also offering timely nutritional guidance to individuals with hyperuricemia or hyperglycemia.154 More recently, Alqahtani et al.343 based on MXene coupled with Zn-BTC MOF and coated by chitosan for smart drug delivery, forming a MXene-Zn-BTC@chitosan nanosystem. The nanosystem could enhance cancer cell therapy by combining controlled release with effective cancer treatment and improving the cells sensitivity to therapeutic intervention, thus improving the therapeutic effect of the cisplatin-MXene-Zn-BTC@chitosan nanocomposites as a chemo-photothermal therapy agent against HepG2 cancer cells.

3.7 Summary

The superior performance of MOF/MXene-based materials across a wide range of application fields (from energy storage and sensing to catalysis and electromagnetic interference shielding) highlights their great potential. However, the scalability of these materials from laboratory-scale synthesis to industrial production and real-world deployment remains a critical, application-specific challenge that must be addressed for their widespread adoption.

A critical analysis reveals that the primary bottlenecks are inherent to the synthesis of the constituent materials and the manufacturing of final devices. The production of high-quality MXene typically involves hazardous etchants (e.g., HF) and multi-step processes, which are energy-intensive and difficult to control. This poses a significant obstacle to safe, cost-effective, and environmentally sustainable large-scale production. Similarly, the synthesis of many MOF materials, especially those that require solvothermal conditions, is usually time-consuming and relies on large volumes of organic solvents, increasing the overall cost and environmental pollution. The challenges of scalability manifest differently in various applications:

- (1) In energy storage (*e.g.*, batteries, SCs), the performance of electrodes like MXene@ hydroxide and ZIF-67@MXene is highly dependent on precise control of morphology and composition. Scaling up while maintaining this level of control, and ensuring the long-term stability of the MXene component, is a significant engineering hurdle.
- (2) In sensing applications, the high selectivity and sensitivity of devices usually rely on complex nanostructures and surface functionalization, which may be difficult to reproduce consistently and affordably on a large scale.
- (3) In catalysis, the hydrogen evolution performance of materials depends on the interfacial connectivity and exposure of active sites. Expanding the synthesis scale while maintaining these nanoscale features is a challenge.
- (4) In electromagnetic interference shielding, achieving high performance typically requires a high filler loading and precise control of microstructure for the composites to balance impedance matching and attenuation. The dispersion of 2D MXene sheets and prevention of restacking are critical for maintaining performance at scale.

Furthermore, the susceptibility of MXene to oxidation under environmental conditions raises concerns about long-term reliability and shelf life, which are critical for commercial products. It is crucial to develop stable, low-cost, and scalable fabrication processes (e.g., printing, roll-to-roll manufacturing) to maintain high performance. In conclusion, while MOF/MXene-based materials offer a compelling combination of properties, their path to widespread application depends on overcoming these multifaceted scalability barriers. Future research should prioritize the development of greener, more efficient, and scalable synthesis routes for both MXene and MOF, alongside the design of stable and simplified device architectures. As highlighted in recent perspectives on zinc-air batteries,107 a concerted effort from materials scientists, chemical engineers, and industry partners is required to bridge the gap between the laboratory and the market.

4. Summary and outlook

In summary, this review has systematically presented the synthesis and applications of MOF/MXene-based materials, categorized into pure MOF/MXene, MOF composite/MXene, and MOF derivative/MXene. The synergistic integration of the high surface area and tunable functionality of MOF materials with the exceptional electrical conductivity and rich surface chemistry composition of MXene has led to remarkable advancements across diverse fields, including energy storage, sensing, catalysis, and electromagnetic interference shielding. This powerful combination has established MOF/MXene-based materials as a development direction for next-generation materials. However, to fully exploit the potential of these materials and transform laboratory innovation into influential industrial technologies, a concerted effort is needed to address key challenges and explore new fields.

4.1. Specific research directions

Review

Future research should focus on advancing a deeper understanding and precise control of MOF/MXene-based materials. Building upon the synthesis strategies discussed, a primary direction is advanced interfacial engineering to achieve strong chemical bonds (e.g., Ti-O-C) at the interface, which is crucial for efficient and stable charge transfer. This requires a deeper mechanistic understanding of the nucleation and growth processes, potentially through the application of in situ characterization techniques. Furthermore, it is crucial to develop more environmentally friendly and scalable synthetic strategies. This includes innovating in situ and ex situ methods and ensuring the environmental sustainability of production processes. The field of MOF derivatives offers a rich platform for innovation, with opportunities to design novel bimetallic or multi-functional hybrids with MXene for enhanced catalytic and electrochemical performance. Finally, reinforcing the integration of theoretical and experimental research will be essential to elucidate the structure-property relationships and guide the rational design of these materials.

4.2. Challenges to commercialization

The path to commercialization is fraught with significant hurdles. The large-scale, cost-effective, and environmentally sustainable production of both high-quality MXene and MOF remains the most critical bottleneck. The synthesis of MXene usually involves hazardous etchants and complex, energyintensive processes, while MOF synthesis can rely on large volumes of organic solvents. The long-term stability of these composites, particularly the susceptibility of MXene to oxidation, is a major concern for device reliability. Additionally, the integration of these nanomaterials into practical devices presents engineering challenges. Combining bottom-up selfassembly approaches with scalable manufacturing technologies, such as 3D printing and roll-to-roll deposition, may facilitate large-scale integration. Fostering collaboration between academia, industry, and government is crucial to translate lab innovations into commercial technologies.

4.3. Interdisciplinary opportunities

The future of MOF/MXene-based materials lies in interdisciplinary collaboration. By merging expertise from materials science, chemistry, physics, and engineering, these composites can be tailored for next-generation technologies. A promising frontier is flexible and wearable electronics, where the mechanical flexibility of MXene and the functional versatility of MOF can be harnessed for integrated health-monitoring devices. Another significant opportunity lies in smart systems and the internet of things, where MOF/MXene composites can serve as multifunctional units combining sensing, energy storage, and signal processing. Exploring their use in solid-state batteries, fuel cells, SCs, and water-splitting devices for hydrogen production represents a crucial interdisciplinary venture. This collaborative effort is indispensable for transforming the exceptional laboratory performance of MOF/

MXene-based materials into transformative practical applications.

Author contributions

Shasha Zheng: writing review & editing, data curation, formal analysis, project administration, investigation, supervision. Keke Zhou: writing original draft, software. Xiaoxue Zhang: writing original draft, investigation. Ning Ren: methodology, investigation.

Conflicts of interest

There are no conflicts to declare.

Data availability

No primary research results, software or code have been included and no new data were generated or analysed as part of this review.

Acknowledgements

This work was supported by the Key Scientific Research Projects Plan of Colleges and Universities in Henan Province (No. 24A150021) and Youth Science and Technology Innovation Special Project of Zhumadian (No. QNZX202308).

References

- 1 Z. Pei, H. Lei and L. Cheng, *Chem. Soc. Rev.*, 2023, **52**, 2031–2081.
- X. Luo, Y. Zhai, P. Wang, B. Tian, S. Liu, J. Li, C. Yang,
 V. Strehmel, S. Li, K. Matyjaszewski, G. Yilmaz,
 B. Strehmel and Z. Chen, *Angew. Chem., Int. Ed.*, 2024, 63, e202316431.
- 3 L. Liu, Y. Pan, L. Ye, C. Liang, X. Mou, X. Dong and Y. Cai, Coord. Chem. Rev., 2024, 517, 216006.
- 4 S. Liang, J. Yao, D. Liu, L. Rao, X. Chen and Z. Wang, *Adv. Mater.*, 2023, **35**, 2211130.
- I. E. Khalil, J. Fonseca, M. R. Reithofer, T. Eder and J. M. Chin, *Coord. Chem. Rev.*, 2023, 481, 215043.
- 6 T. Yao, X. Zeng, X. Tao and H. Xu, Chem. Eng. J., 2024, 487, 150641.
- 7 S. Guo, M. Gao, W. Zhang, F. Liu, X. Guo and K. Zhou, *Adv. Mater.*, 2023, 35, 2303065.
- 8 Y. Wang, Y. Yang, J. Liu, X. Zi, H. Zhu, X. Sun, Y. Miao and Y. Fu, *Chem. Eng. J.*, 2024, **500**, 156850.
- 9 S. Zhou, F. Jia, Y. Wei, J. Du, J. Liu, W. Dong, J. Sui, W. Xue, Y. Yang, L. Chen, X. Meng and S. Yu, *Adv. Funct. Mater.*, 2024, 34, 2314012.
- 10 J. M. Huang, X. D. Zhang, J. Y. Huang, D. S. Zheng, M. Xu and Z. Y. Gu, *Coord. Chem. Rev.*, 2023, **494**, 215333.
- 11 S. Li, W. Han, Q. An, K. Yong and M. Yin, *Adv. Funct. Mater.*, 2023, **33**, 2303447.
- 12 J. Li, C. Hou, C. Chen, W. Ma, Q. Li, L. Hu, X. Lv and J. Dang, *ACS Nano*, 2023, **17**, 10947–10957.

13 Y. Song, C. Yu, D. Ma and K. Liu, *Coord. Chem. Rev.*, 2024, 499, 215492.

RSC Advances

- 14 A. H. Mamaghani, J. Liu, Z. Zhang, R. Gao, Y. Wu, H. Li, M. Feng and Z. Chen, *Adv. Energy Mater.*, 2024, 14, 2402278.
- 15 J. Park, M. Lee, D. Feng, Z. Huang, A. C. Hinckley, A. Yakovenko, X. Zou, Y. Cui and Z. Bao, *J. Am. Chem. Soc.*, 2018, 140, 10315–10323.
- 16 A. M. Patil, S. Moon, Y. Seo, S. B. Roy, A. A. Jadhav, D. P. Dubal, K. Kang and S. C. Jun, *Small*, 2023, 19, 2205491.
- 17 H. Zhu, S. Li, L. Peng, W. Zhong, Q. Wu, S. Cheng and J. Xie, *Nano Energy*, 2024, **125**, 109571.
- 18 W. Zhou, Y. Tang, X. Zhang, S. Zhang, H. Xue and H. Pang, Coord. Chem. Rev., 2023, 477, 214949.
- 19 P. Wiśniewska, J. Haponiuk, M. R. Saeb, N. Rabiee and S. A. Bencherif, *Chem. Eng. J.*, 2023, 471, 144400.
- 20 H. Abed, R. Sabouni and M. Ghommem, *RSC Adv.*, 2024, **14**, 39472–39497.
- 21 T. Zhao, H. Wu, X. Wen, J. Zhang, H. Tang, Y. Deng, S. Liao and X. Tian, *Coord. Chem. Rev.*, 2022, 468, 214642.
- 22 B. Xu, Z. Huang, Y. Liu, S. Li and H. Liu, *Nano Today*, 2023, 48, 101690.
- 23 H. Yang, L. Wang and X. Huang, Coord. Chem. Rev., 2023, 495, 215372.
- 24 G. Tatrari, R. An and F. U. Shah, *Coord. Chem. Rev.*, 2024, 512, 215876.
- 25 R. Abazari, S. Sanati, W. K. Fan, M. Tahir, S. Nayak, K. Parida, M. El-Shahat, R. M. Abdelhameed, D. S. Nesterov, A. M. Kirillov and J. Qian, *Coord. Chem. Rev.*, 2025, 523, 216256.
- 26 W. Zhang, X. Li, X. Ding, K. Hua, A. Sun, X. Hu, Z. Nie, Y. Zhang, J. Wang, R. Li and S. Liu, RSC Adv., 2023, 13, 10800–10817.
- 27 R. Ji, Z. Cui, T. Wu, Y. Xu, M. Yang, R. Zhang, F. Kang, Q. Huang, Q. Zhang and D. Tian, *Coord. Chem. Rev.*, 2025, 540, 216778.
- 28 S. Zheng, X. Li, B. Yan, Q. Hu, Y. Xu, X. Xiao, H. Xue and H. Pang, Adv. Energy Mater., 2017, 7, 1602733.
- 29 Y. Xue, S. Zheng, H. Xue and H. Pang, *J. Mater. Chem. A*, 2019, 7, 7301–7327.
- 30 Y. Du, X. Jia, L. Zhong, Y. Jiao, Z. Zhang, Z. Wang, Y. Feng, M. Bilal, J. Cui and S. Jia, *Coord. Chem. Rev.*, 2022, 454, 214327.
- 31 C. Zhang, Y. Wu, D. Li and H. L. Jiang, *Chem. Sci.*, 2025, **16**, 13149–13172.
- 32 L. Jia, S. Zhou, A. Ahmed, Z. Yang, S. Liu, H. Wang, F. Li, M. Zhang, Y. Zhang and L. Sun, *Chem. Eng. J.*, 2023, 475, 146361.
- 33 Z. Wang, C. Wei, H. Jiang, Y. Zhang, K. Tian, Y. Li, X. Zhang, S. Xiong, C. Zhang and J. Feng, *Adv. Mater.*, 2024, 36, 2306015.
- 34 W. Zeng, X. Ye, Y. Dong, Y. Zhang, C. Sun, T. Zhang, X. Guan and L. Guo, Coord. Chem. Rev., 2024, 508, 215753.
- 35 Z. Wu, S. Liu, Z. Hao and X. Liu, Adv. Sci., 2023, 10, 2207174.
- 36 W. Cao, J. Nie, Y. Cao, C. Gao, M. Wang, W. Wang, X. Lu, X. Ma and P. Zhong, *Chem. Eng. J.*, 2024, 496, 154097.

37 H. Wu, M. Almalki, X. Xu, Y. Lei, F. Ming, A. Mallick, V. Roddatis, S. Lopatin, O. Shekhah, M. Eddaoudi and H. N. Alshareef, J. Am. Chem. Soc., 2019, 141, 20037–20042.

- 38 C. Zheng, Y. Yao, X. Rui, Y. Feng, D. Yang, H. Pan and Y. Yu, *Adv. Mater.*, 2022, **34**, 2204988.
- 39 D. Lei, N. Liu, T. Su, Q. Zhang, L. Wang, Z. Ren and Y. Gao, Adv. Mater., 2022, 34, 2110608.
- 40 C. Wei, Q. Zhang, Z. Wang, W. Yang, H. Lu, Z. Huang, W. Yang and J. Zhu, *Adv. Funct. Mater.*, 2023, 33, 2211889.
- 41 S. Kazim, C. Huang, N. H. Hemasiri, A. Kulkarni, S. Mathur and S. Ahmad, *Adv. Funct. Mater.*, 2024, 34, 2315694.
- 42 J. Li, L. Han, Y. Li, J. Li, G. Zhu, X. Zhang, T. Lu and L. Pan, *Chem. Eng. J.*, 2020, **380**, 122590.
- 43 L. Sun, J. Sun, S. Zhai, T. Dong, H. Yang, Y. Tan, X. Fang, C. Liu, W. Deng and H. Wu, Adv. Energy Mater., 2022, 12, 2200113.
- 44 Y. Chen, H. Yang, Z. Han, Z. Bo, J. Yan, K. Cen and K. K. Ostrikov, *Energy Fuels*, 2022, **36**, 2390–2406.
- 45 B. Zhang, A. Boretti and S. Castelletto, *Chem. Eng. J.*, 2022, 435, 134959.
- 46 X. Bai and J. Guan, Small Struct., 2023, 4, 2200354.
- 47 M. Bilal, A. K. Singh, H. M. N. Iqbal and G. Boczkaj, *Chem. Eng. J.*, 2023, 474, 145020.
- 48 X. Fan, Y. Yang, X. Shi, Y. Liu, H. Li, J. Liang and Y. Chen, *Adv. Funct. Mater.*, 2020, **30**, 2007110.
- 49 L. Wang, H. Song, L. Yuan, Z. Li, P. Zhang, J. K. Gibson, L. Zheng, H. Wang, Z. Chai and W. Shi, *Environ. Sci. Technol.*, 2019, 53, 3739–3747.
- 50 M. Mozafari, A. Arabi Shamsabadi, A. Rahimpour and M. Soroush, *Adv. Mater. Technol.*, 2021, **6**, 2001189.
- 51 I. Persson, J. Halim, H. Lind, T. W. Hansen, J. B. Wagner, L. Å. Näslund, V. Darakchieva, J. Palisaitis, J. Rosen and P. O. Å. Persson, Adv. Mater., 2019, 31, 1805472.
- 52 Y. Zhou, Y. Zhang, K. Ruan, H. Guo, M. He, H. Qiu and J. Gu, *Sci. Bull.*, 2024, **69**, 2776–2792.
- 53 J. Liu, M. Wang, C. Guo, Z. Tao, M. Wang, L. He, B. Liu and Z. Zhang, *Food Chem.*, 2023, 416, 135839.
- 54 Y. Jo, Y. K. Jo, J. Lee, H. W. Jang, I. Hwang and D. J. Yoo, *Adv. Mater.*, 2023, 35, 2206842.
- 55 R. Qin, J. Nong, K. Wang, Y. Liu, S. Zhou, M. Hu, H. Zhao and G. Shan, *Adv. Mater.*, 2024, **36**, 2312761.
- 56 S. Elbeltagi, M. Al-zharani, F. A. Nasr, A. M. Ismail, H. M. El-Tohamy, K. M. Abdelbased and Z. E. Eldin, *Int. J. Pharm.*, 2025, 674, 125492.
- 57 B. Deng, Z. Liu, F. Pan, Z. Xiang, X. Zhang and W. Lu, *J. Mater. Chem. A*, 2021, **9**, 3500–3510.
- 58 M. Liu, Z. Zhang, M. Yang, P. Li, Y. Wang, Y. He and J. Yuan, *Composites, Part A*, 2022, **161**, 107122.
- 59 L. Wang, H. Liu, X. Lv, G. Cui and G. Gu, *J. Alloys Compd.*, 2020, **828**, 154251.
- 60 Y. Ji, Y. Zhang, J. Lu, F. Gao, X. Lv, X. Qu, G. Zhu, T. Tian, H. Pang, Y. Tian and X. Dong, *Adv. Healthc. Mater.*, 2025, 14, 2404723.
- 61 Y. He, Y. Zou, L. Sun, F. Xu, Y. Xia, Y. Chen, S. Wang, Z. Hu, S. Hao and C. Xiang, *J. Energy Storage*, 2025, **119**, 116385.
- 62 X. Zhang, G. Jin, Y. Liu, Y. Liu, M. Zhang, C. Li, X. Zhang and D. Cao, *Adv. Compos. Hybrid Mater.*, 2025, **8**, 206.

63 X. Zhuang, S. Zhang, Y. Tang, F. Yu, Z. Li and H. Pang, Coord. Chem. Rev., 2023, 490, 215208.

- 64 H. Saini, N. Srinivasan, V. Šedajová, M. Majumder, D. P. Dubal, M. Otyepka, R. Zbořil, N. Kurra, R. A. Fischer and K. Jayaramulu, *ACS Nano*, 2021, **15**, 18742–18776.
- 65 T. Xu, Y. Wang, Y. Xue, J. Li and Y. Wang, *Chem. Eng. J.*, 2023, 470, 144247.
- 66 F. Ren, L. Ma, C. Li, T. Wu, J. Zhang, L. Pei, Y. Jin, Z. Sun, Z. Guo, P. Song and P. Ren, *Carbohydr. Polym.*, 2025, 356, 123369
- 67 A. Hanan, M. N. Lakhan, F. Bibi, A. Khan, I. A. Soomro, A. Hussain and U. Aftab, *Chem. Eng. J.*, 2024, 482, 148776.
- 68 I. Ijaz, A. Bukhari, E. Gilani, A. Nazir and H. Zain, *RSC Adv.*, 2023, **13**, 5643–5655.
- 69 H. Kefayati, Y. Yamini and M. Ghaemmaghami, *Microchim. Acta*, 2025, **192**, 145.
- 70 S. Zheng, H. Zhou, H. Xue, P. Braunstein and H. Pang, J. Colloid Interface Sci., 2022, 614, 130–137.
- 71 S. Huang, H. Wang, C. Xiang, D. Luo, H. Zeng, A. Cai, X. Ma, C. Fang and J. Deng, J. Membr. Sci., 2025, 719, 123738.
- 72 A. Chaouiki, M. Chafiq, R. Salghi, N. Elboughdiri, J. H. Kang, Y. G. Ko and M. Abboud, J. Energy Chem., 2025, 104, 687–715.
- 73 S. Bibi, S. S. A. Shah, M. A. Nazir, M. H. Helal, S. M. El-Bahy, Z. M. El-Bahy, S. Ullah, M. A. Wattoo and A. ur Rehman, Adv. Sustain. Syst., 2024, 8, 2400011.
- 74 Y. Zhao, J. Zhang, X. Guo, X. Cao, S. Wang, H. Liu and G. Wang, *Chem. Soc. Rev.*, 2023, **52**, 3215–3264.
- 75 N. Kitchamsetti and J. S. Cho, *J. Energy Storage*, 2024, **80**, 110293.
- 76 H. Wang, X. Li, Y. Deng, J. Jiang, H. Ma and J. Zou, *Coord. Chem. Rev.*, 2025, 529, 216462.
- 77 H. Ji, Y. Liu, G. Du, T. Huang, Y. Zhu, Y. Sun and H. Pang, *Chem. Res. Chin. Univ.*, 2024, **40**, 943–963.
- 78 G. T. Tran, T. T. T. Nguyen and T. Van Tran, *Coord. Chem. Rev.*, 2025, **544**, 217002.
- 79 R. Ghanbari and E. Nazarzadeh Zare, *Coord. Chem. Rev.*, 2024, 518, 216089.
- 80 Y. Zheng, S. Zheng, H. Xue and H. Pang, *Adv. Funct. Mater.*, 2018, **28**, 1804950.
- 81 N. A. I. M. Mokhtar, R. M. Zawawi, W. M. Khairul and N. A. Yusof, *Environ. Chem. Lett.*, 2022, **20**, 3099–3131.
- 82 S. Ullah, A. ur Rehman, T. Najam, I. Hossain, S. Anjum, R. Ali, M. U. Shahid, S. S. A. Shah and M. A. Nazir, *J. Ind. Eng. Chem.*, 2024, 137, 87–105.
- 83 S. Gautam, S. Rialach, S. Paul and N. Goyal, *RSC Adv.*, 2024, **14**, 14311–14339.
- 84 Y. Absalan, M. Gholizadeh, E. B. Kim, S. Ameen, Y. Wang, Y. Wang and H. He, *Coord. Chem. Rev.*, 2024, 515, 215972.
- 85 A. K. Bindra, D. Wang and Y. Zhao, *Adv. Mater.*, 2023, 35, 2300700.
- 86 Y. Zhang, X. Feng, S. Yuan, J. Zhou and B. Wang, *Inorg. Chem. Front.*, 2016, 3, 896–909.
- 87 F. Parsapour, M. Moradi, V. Safarifard and S. Sojdeh, *J. Energy Storage*, 2024, **82**, 110487.
- 88 C. Brahmi, M. Benltifa, C. Vaulot, L. Michelin, F. Dumur, F. Millange, M. Frigoli, A. Airoudj, F. Morlet-Savary,

- L. Bousselmi and J. Lalevée, Eur. Polym. J., 2021, 154, 110560.
- 89 M. Kalaj, K. C. Bentz, S. Ayala, J. M. Palomba, K. S. Barcus, Y. Katayama and S. M. Cohen, *Chem. Rev.*, 2020, **120**, 8267– 8302
- I. Salahshoori, M. Golriz, M. Namayandeh Jorabchi,
 S. Moghari and H. A. Khonakdar, *Coord. Chem. Rev.*, 2025,
 543, 216919.
- 91 W. Lv, Y. Song, H. Pei and Z. Mo, *J. Ind. Eng. Chem.*, 2023, **128**, 17–54.
- 92 T. Wu, X. Liu, Y. Liu, M. Cheng, Z. Liu, G. Zeng, B. Shao, Q. Liang, W. Zhang, Q. He and W. Zhang, *Coord. Chem. Rev.*, 2020, 403, 213097.
- 93 J. Aguilera-Sigalat and D. Bradshaw, *Coord. Chem. Rev.*, 2016, 307, 267–291.
- 94 M. Zahran, S. Tian, J. Li, A. H. Marei, Y. Xie, Q. Liu, J. Huang, D. Wang, X. Ning, J. Wang, H. Chi and X. Li, RSC Adv., 2025, 15, 10801-10815.
- 95 Y. Liu, Z. Liu, D. Huang, M. Cheng, G. Zeng, C. Lai, C. Zhang, C. Zhou, W. Wang, D. Jiang, H. Wang and B. Shao, Coord. Chem. Rev., 2019, 388, 63-78.
- 96 M. Mukoyoshi and H. Kitagawa, Chem. Commun., 2022, 58, 10757–10767.
- 97 S. Tang, Y. Wang, P. He, Y. Wang and G. Wei, *Materials*, 2024, 17, 2660.
- 98 J. Yu, C. Mu, B. Yan, X. Qin, C. Shen, H. Xue and H. Pang, *Mater. Horiz.*, 2017, 4, 557–569.
- 99 Y. Liu, D. Huang, M. Cheng, Z. Liu, C. Lai, C. Zhang, C. Zhou, W. Xiong, L. Qin, B. Shao and Q. Liang, *Coord. Chem. Rev.*, 2020, 409, 213220.
- 100 X. Lian, Y. Fang, E. Joseph, Q. Wang, J. Li, S. Banerjee, C. Lollar, X. Wang and H. C. Zhou, *Chem. Soc. Rev.*, 2017, 46, 3386–3401.
- 101 J. Jiang, Y. Shi, M. Wu, M. Rezakazemi, T. M. Aminabhavi, R. Huang, C. Jia and S. Ge, *Chem. Eng. J.*, 2024, **494**, 152932.
- 102 Y. Chen, Y. Shi, G. Song, B. Yang and H. Pang, *Next Mater.*, 2025, **6**, 100323.
- 103 Q. Wu, J. Liang, D. Wang, R. Wang and C. Janiak, *Chem. Soc. Rev.*, 2025, 54, 601–622.
- 104 W. K. Fan, A. Sherryna and M. Tahir, *ACS Omega*, 2022, 7, 38158–38192.
- 105 Y. Ji, Y. You, G. Xu, X. Yang and Y. Liu, *Chem. Eng. J.*, 2024, 483, 149365.
- 106 H. Yang, G. X. Zhang, H. J. Zhou, Y. Y. Sun and H. Pang, *Energy Mater. Adv.*, 2023, 4, 0033.
- 107 T. Ramachandran, R. K. Raji and M. Rezeq, *J. Mater. Chem. A*, 2025, **13**, 12855–12890.
- 108 S. Venkateswarlu, S. Vallem, M. Umer, N. V. V. Jyothi, A. Giridhar Babu, S. Govindaraju, Y. Son, M. Jong Kim and M. Yoon, *J. Energy Chem.*, 2023, **86**, 409–436.
- 109 N. Khosroshahi, M. Bakhtian, A. Asadi and V. Safarifard, *Nano Express*, 2023, **4**, 042002.
- 110 B. Tahir, A. Alraeesi and M. Tahir, *Front. Chem.*, 2024, **12**, 1448700.
- 111 S. Afzal, A. ur Rehman, T. Najam, I. Hossain, M. A. I. Abdelmotaleb, S. Riaz, M. R. Karim, S. S. A. Shah and M. A. Nazir, *Chemosphere*, 2024, 364, 143194.

RSC Advances

- 112 S. Bagyalakshmi, K. S. Balamurugan, M. Mathankumar, A. Sivakami and N. R. Devi, J. Mol. Struct., 2025, 1334, 141838.
- 113 P. Cao, Y. L. Liu, Q. Zhang, C. Guo, J. Li and Q. Zeng, Coord. Chem. Rev., 2025, 545, 217018.
- 114 R. Verma, P. Thakur, A. Chauhan, R. Jasrotia and A. Thakur, Carbon, 2023, 208, 170-190.
- 115 S. Feng, S. Wen, R. Wang, X. Yang, X. Yuan, Y. Liu, J. Ma and Z. Li, Nanomaterials, 2025, 15, 841.
- 116 Z. Bai, L. Guo, J. Huang, H. Li, G. An, H. Zheng, N. Wang, Z. Li and Y. Zhu, Chem. Eng. J., 2024, 479, 147932.
- 117 Y. Liu, D. Luo, Y. Deng, J. Zheng, F. Wu, X. Dai and C. Deng, J. Energy Storage, 2023, 67, 107641.
- 118 K. Sharma, V. Hasija, S. Patial, P. Singh, V. H. Nguyen, A. K. Nadda, S. Thakur, P. Nguyen-Tri, C. C. Nguyen, S. Y. Kim, Q. Van Le and P. Raizada, Int. J. Hydrogen Energy, 2023, 48, 6560-6574.
- 119 Y. Sun, C. Song, X. Guo, S. Hong, J. Choi and Y. Liu, J. Membr. Sci., 2020, 616, 118615.
- 120 C. Liu, Y. Bai, W. Li, F. Yang, G. Zhang and H. Pang, Angew. Chem., Int. Ed., 2022, 61, e202116282.
- 121 M. Mahato, J. Kim, M. Lee, S. Jo, G. Kim, S. Nam, J. Kim, V. H. Nguyen, M. Garai, H. Yoo, D. Saatchi, Z. Ullah, C. W. Ahn, Y. Gogotsi and I. Oh, Adv. Mater., 2025, 2500479.
- 122 X. Zhang, Z. Wang and X. Guo, Sci. Rep., 2025, 15, 3727.
- 123 G. Zeng, Y. Liu, Q. Lin, S. Pu, S. Zheng, M. B. M. Y. Ang and Y. H. Chiao, Sep. Purif. Technol., 2022, 293, 121052.
- 124 J. Zhang, Z. Li, Q. Zhang, L. Zhang, T. Ma, X. Ma, K. Liang, Y. Ying and Y. Fu, ACS Appl. Mater. Interfaces, 2023, 15, 17222-17232.
- 125 J. Zhang, X. Cheng, J. Jiang, A. Pattanateeradetch, S. Shi, C. Chokejaroenrat, Q. Xu and J. Lu, Inorg. Chem., 2025, 64, 4920-4933.
- 126 N. Liu, Y. Zheng, C. Jing, B. Gao, W. Huang, Z. Li, J. Lei, X. Zhang, L. Cui and L. Tang, J. Mol. Liq., 2020, 311, 113201.
- 127 L. Yang, Y. Chen, Q. Wen, H. Xu, X. Pan and X. Li, Electrochim. Acta, 2022, 428, 140959.
- 128 M. Wan, C. Shi, X. Qian, Y. Qin, J. Jing, H. Che, F. Ren, J. Li and B. Yu, Composites, Part A, 2022, 163, 107187.
- 129 D. Cheng, P. Li, X. Zhu, M. Liu, Y. Zhang and Y. Liu, Chin. J. Chem., 2021, 39, 2181-2187.
- 130 J. Paul and J. Kim, Appl. Surf. Sci., 2023, 613, 156103.
- 131 R. Li, X. Fu, G. Liu, J. Li, G. Zhou, G. Liu and W. Jin, J. Membr. Sci., 2022, 664, 121097.
- 132 Y. Wen, Z. Wei, C. Ma, X. Xing, Z. Li and D. Luo, Nanomaterials, 2019, 9, 775.
- 133 P. Xiao, G. Zhu, X. Shang, B. Hu, B. Zhang, Z. Tang, J. Yang and J. Liu, J. Electroanal. Chem., 2022, 916, 116382.
- 134 B. Jia, H. Yang, L. Wang, Z. Zhao and X. Wu, Appl. Surf. Sci., 2022, 602, 154386.
- 135 H. Li, H. Lin, S. Raza, C. Chen, W. Yu, Q. Zeng, Z. Zhao, X. Huang and L. Shen, J. Membr. Sci., 2025, 718, 123685.
- 136 J. Wang, Y. Shen, Y. Zhuang, J. Wang and Y. Zhang, Anal. Chem., 2024, 96, 12102-12111.
- 137 W. Han, Y. Yan, H. Wang, J. Li, P. Zhao, Z. Liu, F. Yu, J. Cui and G. Zhang, Langmuir, 2024, 40, 21767-21779.

- 138 Y. Liu, X. Meng, Z. Ma, H. Gu, X. Luo, X. Yin, H. Yi and Y. Chen, Food Chem., 2025, 463, 141496.
- 139 R. Ramachandran, K. Rajavel, W. Xuan, D. Lin and F. Wang, Ceram. Int., 2018, 44, 14425-14431.
- 140 X. Liang, X. Ren, Q. Yang, L. Gao, M. Gao, Y. Yang, H. Zhu, G. Li, T. Ma and A. Liu, Nanoscale, 2021, 13, 2843-2848.
- 141 M. Wan, C. Shi, X. Qian, Y. Qin, J. Jing and H. Che, Nanomaterials, 2022, 12, 1142.
- 142 N. Li, L. Yang, R. Su, N. Shi, J. Wu, J. Zhao, L. Wen and Z. Wang, Desalination, 2023, 566, 116940.
- 143 K. S. Ranjith, S. Sonwal, A. Mohammadi, G. Seeta Rama Raju, M.-H. Oh, Y. S. Huh and Y.-K. Han, J. Mater. Chem. A, 2024, 12, 26132-26146.
- 144 D. Roy, R. Singh, S. Mandal and N. Chanda, Anal. Methods, 2024, 16, 6183-6192.
- 145 J. Ding, Q. Wang, X. Liu, S. Li and H. Li, J. Hazard. Mater., 2024, 480, 136261.
- 146 J. Qin, B. Liu, K. H. Lam, S. Song, X. Li and X. Hu, ACS Sustain. Chem. Eng., 2020, 8, 17791-17799.
- 147 L. Cheng, Y. Tang, M. Xie, Y. Sun and H. Liu, J. Alloys Compd., 2021, 864, 158913.
- 148 X. Zhang, S. Yang, W. Lu, D. Lei, Y. Tian, M. Guo, P. Mi, N. Qu and Y. Zhao, J. Colloid Interface Sci., 2021, 592, 95-102.
- 149 H. Zhang, Z. Li, Z. Hou, H. Mei, Y. Feng, B. Xu and D. Sun, Chem. Eng. J., 2021, 425, 130602.
- 150 A. Ganiyat Olatoye, W. Li, E. Oluwaseyi Fagbohun, X. Zeng, Y. Zheng and Y. Cui, J. Electroanal. Chem., 2023, 928, 117036.
- 151 X. Yang, Y. Tian, S. Li, Y. P. Wu, Q. Zhang, D. S. Li and S. Zhang, J. Mater. Chem. A, 2022, 10, 12225-12234.
- 152 S. Li, Y. Wang, Y. Li, J. Xu, T. Li and T. Zhang, Nanomaterials, 2023, 13, 610.
- 153 O. P. Nanda, M. Ravipati, L. Durai and S. Badhulika, Mater. Res. Bull., 2023, 168, 112488.
- 154 X. Lin, D. Song, T. Shao, T. Xue, W. Hu, W. Jiang, X. Zou and N. Liu, Adv. Funct. Mater., 2023, 2311637.
- 155 W. Xu, Y. Lu, Z. Zhang, Q. Zhou, W. Zhao, R. Yang, L. Zhang, L. Yang, X. Gao and G. Pan, IEEE Sens. J., 2024, 24, 9437-9448.
- 156 R. Zhu, Y. Gu, L. Liu, J. Lu and H. Pang, New J. Chem., 2024, 48, 10593-10598.
- 157 Y. Ji, W. Li, Y. You and G. Xu, Chem. Eng. J., 2024, 496, 154009.
- 158 D. S. Shivade, A. N. Kurade, R. K. Bhosale, S. S. Kundale, A. R. Shelake, A. D. Patil, P. P. Waifalkar, R. K. Kamat, A. M. Teli and T. D. Dongale, J. Energy Storage, 2024, 100,
- 159 C. Gu, C. Lu, Y. X. Gao, P. Tan, S. S. Peng, X. Q. Liu and L. B. Sun, Inorg. Chem., 2021, 60, 1380-1387.
- 160 H. Hassan, E. Umar, M. W. Iqbal, A. K. Alqorashi, B. S. Almutair, H. Alrobei, A. M. Afzal and N. Ahmad, New J. Chem., 2024, 48, 6277-6295.
- 161 Z. Liu, H. Lv, Y. Zhang, J. W. He, L. Han, S. Li, L. Yang and Y. Xu, ACS Sens., 2024, 9, 3641-3651.

162 A. Sharma, H.-S. Lee, C.-M. Yeom, H. K. Surendran, C. Narayana, S. B. Eadi, R. Zboril, H.-D. Lee and K. Jayaramulu, *Chem. Mater.*, 2024, **36**, 8466–8476.

- 163 H. Zhu, Y. Chen, T. Zhang, L. Qin, S. Z. Kang and X. Li, *J. Solid State Chem.*, 2023, **327**, 124298.
- 164 W. H. Lin, T. Y. Huang, C. H. Bai, C. H. Hung, C. A. Lung, W. H. Hung, K. Gopinadhan and L. H. Yeh, *Nano Energy*, 2024, 128, 109924.
- 165 Y. Wang, W. Yang, J. Cao, Y. Liu, M. Shao, X. Xu and H. Chen, *Sens. Actuators*, *B*, 2024, 417, 136066.
- 166 Q. Zhou, Q. Ding, Z. Geng, C. Hu, L. Yang, Z. Kan, B. Dong, M. Won, H. Song, L. Xu and J. S. Kim, *Nano-Micro Lett.*, 2025, 17, 50.
- 167 Y. Ge, D. Lei, C. Zhang, Q. Zhang, J. Mu and J. Li, *Adv. Sci.*, 2025, **12**, 2500027.
- 168 Y. Li, P. Kamdem and X. J. Jin, *J. Electrochem. Soc.*, 2020, **167**, 110562.
- 169 Y. Yao, X. Han, X. Yang, J. Zhao and C. Chai, *Chin. J. Chem.*, 2021, **39**, 330–336.
- 170 Y. Wang, W. Sun, Y. Li, X. Zhuang, C. Tian, F. Luan and X. Fu, *Microchem. J.*, 2021, **167**, 106332.
- 171 N. Rabiee, M. Bagherzadeh, M. Jouyandeh, P. Zarrintaj, M. R. Saeb, M. Mozafari, M. Shokouhimehr and R. S. Varma, *ACS Appl. Bio Mater.*, 2021, 4, 5106–5121.
- 172 C. Guo, F. Cheng, G. Liang, S. Zhang, S. Duan, Y. Fu, F. Marchetti, Z. Zhang and M. Du, *Adv. NanoBiomed Res.*, 2022, 2, 2200064.
- 173 Y. Yao, T. Wang, L. Wu and H. Chen, *Desalination*, 2022, 543, 116116.
- 174 G. Deng, M. Sun, Y. Shi, Y. Feng, Y. Lv, L. Tang, J. Gao and P. Song, *J. Clean. Prod.*, 2023, **403**, 136887.
- 175 L. P. Hao, A. Hanan, R. Walvekar, M. Khalid, F. Bibi, W. Y. Wong and C. Prakash, *Catalysts*, 2023, 13, 802.
- 176 H. Shahriyari Far, M. Najafi, M. Hasanzadeh and R. Rahimi, *Inorg. Chem. Commun.*, 2023, **152**, 110680.
- 177 C. Wen, D. Guo, X. Zheng, H. Li and G. Sun, *ACS Appl. Energy Mater.*, 2021, **4**, 8231–8241.
- 178 S. Kashif, S. Akram, M. Murtaza, A. Amjad, S. S. A. Shah and A. Waseem, *Diam. Relat. Mater.*, 2023, **136**, 110023.
- 179 B. Xiang, J. Gong, Y. Sun, W. Yan, R. Jin and J. Li, *J. Membr. Sci.*, 2024, **691**, 122247.
- 180 A. Maleki and A. Bozorg, Chemosphere, 2024, 364, 143273.
- 181 Y. Meng, F. Yue, S. Zhang, L. Zhang, C. Li, M. Shi, Y. Ma, M. Berrettoni, X. Zhang and H. Zhang, *Carbon Capture Sci. Technol.*, 2024, 13, 100274.
- 182 Y. Liu, Y. He, E. Vargun, T. Plachy, P. Saha and Q. Cheng, *Nanomaterials*, 2020, **10**, 695.
- 183 C. Du, Q. Song, Q. Liang, X. Zhao, J. Wang, R. Zhi, Y. Wang and H. Yu, *ChemNanoMat*, 2021, 7, 539–544.
- 184 F. Wu, Z. Liu, J. Wang, T. Shah, P. Liu, Q. Zhang and B. Zhang, *Chem. Eng. J.*, 2021, 422, 130591.
- 185 T. Xiao, J. Jin, Y. Zhang, W. Xi, R. Wang, Y. Gong, B. He and H. Wang, *Electrochim. Acta*, 2022, **427**, 140851.
- 186 L. Yue, L. Chen, X. Wang, D. Lu, W. Zhou, D. Shen, Q. Yang, S. Xiao and Y. Li, *Chem. Eng. J.*, 2023, **451**, 138687.
- 187 P. Tan, R. Gao, Y. Zhang, N. Han, Y. Jiang, M. Xu, S. J. Bao and X. Zhang, *J. Colloid Interface Sci.*, 2023, **630**, 363–371.

- 188 D. Xu, Z. Zhang, K. Tao and L. Han, *Dalton Trans.*, 2023, **52**, 2455–2462.
- 189 J. Liu, Q. Xia, L. Wang, Q. Hu, N. M. Shinde and A. Zhou, *ACS Appl. Mater. Interfaces*, 2024, **16**, 49380–49391.
- 190 M. Murtaza, K. Farooq, W. A. Shah, I. Ahmad and A. Waseem, *Nanoscale Adv.*, 2024, **6**, 6317–6327.
- 191 K. Yu, J. Zhang, Y. Hu, L. Wang, X. Zhang and B. Zhao, Catalysts, 2024, 14, 184.
- 192 Z. Li, S. Ning, F. Hu, H. Zhu, L. Zeng, L. Chen, X. Wang, T. Fujita and Y. Wei, *J. Colloid Interface Sci.*, 2023, **629**, 97–110.
- 193 M. Adil, A. G. Olabi, M. A. Abdelkareem, H. Alawadhi, A. Bahaa, K. ElSaid and C. Rodriguez, *J. Energy Storage*, 2023, **68**, 107817.
- 194 M. Murtaza, K. Farooq, A. A. Amjad, S. S. A. Shah and A. Waseem, *Diam. Relat. Mater.*, 2024, **147**, 111379.
- 195 V. A. Thai, T. B. Nguyen, C. W. Chen, X. T. Bui, R. Doong and C. D. Dong, *Environ. Sci. Nano*, 2024, **11**, 3871–3886.
- 196 S. Li, L. Zhang, P. Ye, M. Zhu, Y. Nie, Y. Dai and F. Yang, *Cryst. Growth Des.*, 2024, 24, 7445–7454.
- 197 M. Ali, A. M. Afzal, S. Mumtaz, K. Yusuf and A. Deifalla, *J. Energy Storage*, 2024, **92**, 111972.
- 198 S. Siva Shalini, Y. P. Fu and A. Chandra Bose, *Chem. Eng. J.*, 2024, **500**, 156751.
- 199 K. Gong, L. Cai, C. Shi, F. Gao, L. Yin, X. Qian and K. Zhou, *Composites, Part A*, 2022, **161**, 107109.
- 200 Y. Chen, S. Li, L. Zhang, T. Jing, J. Wang, L. Zhao, F. Li, C. Li and J. Sun, J. Solid State Chem., 2022, 308, 122919.
- 201 S. Li, H. Chai, L. Zhang, Y. Xu, Y. Jiao and J. Chen, *J. Colloid Interface Sci.*, 2023, **642**, 235–245.
- 202 Y. Zhang, H. Yuan, X. Chen, Z. Jiang, J. Lu and F. Xin, *ACS Appl. Polym. Mater.*, 2024, **6**, 8277–8290.
- 203 S. Li, Q. Cheng, P. Ye, Y. Zhang, L. Zhang, F. Liu, H. Qiu, X. Qu and Y. Nie, *Appl. Organomet. Chem.*, 2024, 38, e7547.
- 204 K. Zhao, B. Zhang, X. Cui, X. Chao, F. Song, H. Chen and B. He, *Food Chem.*, 2024, 461, 140828.
- 205 F. Yu, X. Yu, P. Jia, X. Zhou, H. Wang, Y. Hou, B. Wang, L. Song and Y. Hu, *Chem. Eng. J.*, 2024, 499, 156145.
- 206 Y. Lin, W. Dong, S. Li, S. Zhang, X. Chen, B. Wang and L. Du, *Polym. Degrad. Stab.*, 2025, 234, 111251.
- 207 G. Kaur, S. Sharma, N. Bhardwaj, M. K. Nayak and A. Deep, *Food Control*, 2024, **165**, 110694.
- 208 W. Wang, Y. Bai, P. Yang, S. Yuan, F. Li, W. Zhao, B. Jin, X. Zhang, S. Liu, D. Yuan and Q. Zhao, *Sci. Bull.*, 2023, 68, 2180–2189.
- 209 G. Dai, Y. Li, Z. Li, J. Zhang, X. Geng, F. Zhang, Q. Wang and P. He, *ACS Appl. Nano Mater.*, 2022, 5, 9201–9208.
- 210 H. Huang, J. Qin, C. Liu, L. Luo, Y. Lan, L. Yang, J. Zhang and H. He, *Carbon*, 2024, **226**, 119171.
- 211 W. Wen, Y. Dang, J. Tang, C. Su, S. Yu, J. Ma and Y. Zhou, *J. Electrochem. Soc.*, 2024, **171**, 057514.
- 212 X. Zhang, H. Wang, R. Dai, P. Zhao and Y. Wang, *J. Colloid Interface Sci.*, 2025, **690**, 137278.
- 213 Z. H. Lu, Q. Tian, D. D. Zhou, M. Chen, Y. W. Cao, L. Y. Zhuang, X. Liu, Z. H. Yang and I. A. Senosy, *J. Environ. Chem. Eng.*, 2022, **10**, 108037.

214 J. Chi, P. Ju, F. Bi, T. Jiang, S. Wen, Y. Cai, L. Wang and M. Qiu, *Adv. Funct. Mater.*, 2025, 35, 2415174.

RSC Advances

- 215 X. Tu, F. Gao, X. Ma, J. Zou, Y. Yu, M. Li, F. Qu, X. Huang and L. Lu, *J. Hazard. Mater.*, 2020, **396**, 122776.
- 216 S. M. S. Rana, M. T. Rahman, M. A. Zahed, S. H. Lee, Y. Do Shin, S. Seonu, D. Kim, M. Salauddin, T. Bhatta, K. Sharstha and J. Y. Park, *Nano Energy*, 2022, **104**, 107931.
- 217 A. Rajan, M. Daniel, J. Rafi, A. R. S. C. Lazuli and B. Neppolian, *ChemSusChem*, 2024, **18**, e202400207.
- 218 Y. Qi, Y. Chen, Q. Li, X. Dang and H. Chen, *Anal. Chim. Acta*, 2024, **1316**, 342876.
- 219 H. Hassan, K. Khan, S. Mumtaz, A. A. Rafi, A. M. Idris, A. Althobaiti and A. Mohammad, J. Power Sources, 2024, 623, 235486.
- 220 Z. F. Lin, T. H. Wang, P. Venkatesan and R. A. Doong, *Chem. Eng. J.*, 2025, **505**, 159411.
- 221 X. Zhao, M. Zhu, C. Tang, K. Quan, Q. Tong, H. Cao, J. Jiang, H. Yang and J. Zhang, *J. Colloid Interface Sci.*, 2022, **620**, 478–485.
- 222 L. Guo, L. Tao and T. Wang, Langmuir, 2024, 40, 8862-8871.
- 223 X. Liang, Y. Yan, G. Liu, S. Hou and S. Hou, *Chem. Eng. J.*, 2024, **483**, 149301.
- 224 S. Hou, M. Wen, J. Wei, L. Li and G. Liu, *J. Mol. Struct.*, 2025, 1321, 140076.
- 225 X. Zhu, F. Liu, L. Meng, Q. Gao, X. Wang, M. Lou, X. Xu, W. Zhang, F. Li and B. Van der Bruggen, *Nano Lett.*, 2025, 25, 2810–2819.
- 226 H. Yang, P. Zhang, Q. Zheng, A. Hayat, H. S. M. Abd-Rabboh, S. Raza, D. Li and Y. Sui, *J. Mater. Chem. C*, 2024, 12, 17620–17634.
- 227 C. Sun, D. Lan, Z. Jia, Z. Gao and G. Wu, *Small*, 2024, **20**, 2405874.
- 228 H. Yang, S. Yin, P. Zhang, Q. Zheng, S. Raza, D. Li and Y. Sui, *Sep. Purif. Technol.*, 2025, **365**, 132600.
- 229 J. Bian, M. Liu, X. Liu, X. Bian, C. Gu, J. Ma and T. Jiang, Microchem. J., 2025, 210, 113021.
- 230 H. Gao, J. You, H. Wu and M. Tian, *Food Chem.*, 2025, 473, 143092.
- 231 J. Wang, Y. Zhang, Z. Chen, Z. Zhou, J. Wang, C. Ma, W. Qiao, Z. Xu and L. Ling, *J. Colloid Interface Sci.*, 2025, 678, 79–88.
- 232 H. B. Parse, I. Patil, B. Kakade and A. Swami, *Energy Fuels*, 2021, 35, 17909–17918.
- 233 X. Han, Y. Huang, L. Ding, Y. Song, T. Li and P. Liu, *ACS Appl. Nano Mater.*, 2021, 4, 691–701.
- 234 Z. Xiang, Y. Shi, X. Zhu, L. Cai and W. Lu, *Nano-Micro Lett.*, 2021, 13, 150.
- 235 Z. Liu, J. Chen, M. Que, H. Zheng, L. Yang, H. Yuan, Y. Ma, Y. Li and X. Yang, *Chem. Eng. J.*, 2022, **450**, 138442.
- 236 W. Liu, X. Liu, X. Tan, M. Zhao, Z. Liu, M. Yi, Q. Ding, Y. Ren and H. Li, *Sens. Actuators, B*, 2025, **433**, 137577.
- 237 C. Ji, C. Yan, Z. Wei, T. Yu, J. Fan and Y. Li, *Chem. Eng. J.*, 2024, **483**, 149431.
- 238 W. Xie, Y. Wang, J. Zhou, M. Zhang, J. Yu, C. Zhu and J. Xu, *Appl. Surf. Sci.*, 2020, **534**, 147584.
- 239 B. Lei, X. Huang, P. Wu, L. Wang, J. Huang and Z. Wang, *Ceram. Int.*, 2022, **48**, 25111–25119.

- 240 C. Shi, Z. Long, C. Wu, H. Dai, Z. Li, H. Qiao, K. Liu, Q. H. Fan and K. Wang, *Small*, 2023, **19**, 2303802.
- 241 S. R. Shingte, V. D. Chavan, R. P. Dhavale, D.-K. Kim, H.-H. Park, T. D. Dongale and P. B. Patil, *J. Energy Storage*, 2024, **92**, 112169.
- 242 M. Liu, J. Wang, P. Song, J. Ji and Q. Wang, *Sens. Actuators*, *B*, 2022, **361**, 131755.
- 243 S. Zhang, Y. Ding, Q. Wang and P. Song, *Sens. Actuators, B*, 2023, **393**, 134122.
- 244 A. Wei, L. Wang and Z. Li, *J. Alloys Compd.*, 2022, **899**, 163369.
- 245 T. Kshetri, D. D. Khumujam, T. I. Singh, Y. S. Lee, N. H. Kim and J. H. Lee, *Chem. Eng. J.*, 2022, **437**, 135338.
- 246 W. Wu, C. Zhao, H. Liu, T. Liu, L. Wang and J. Zhu, *J. Colloid Interface Sci.*, 2022, **623**, 216–225.
- 247 X. Bu, F. Ma, Q. Wu, H. Wu, Y. Yuan, L. Hu, C. Han, X. Wang, W. Liu and X. Li, *Sens. Actuators*, B, 2022, 369, 132232.
- 248 H. Geun Oh and S. K. Park, Appl. Surf. Sci., 2021, 564, 150415.
- 249 Y. Zhou, Y. Wu, D. Guo, J. Li, D. Chu, S. Na, M. Yu, D. Li, G. Sui and D. F. Chai, *J. Alloys Compd.*, 2023, 963, 171133.
- 250 M. T. Rahman, S. M. S. Rana, M. Salauddin, M. A. Zahed, S. Lee, E. S. Yoon and J. Y. Park, *Nano Energy*, 2022, **100**, 107454.
- 251 J. Wang, Y. Huang, S. Zhang, X. Du, Z. Duan and X. Sun, *J. Mater. Sci. Technol.*, 2023, **147**, 112–123.
- 252 D. Wang, D. Zhang, Y. Yang, Q. Mi, J. Zhang and L. Yu, ACS Nano, 2021, 15, 2911–2919.
- 253 D. Song, X. Jiang, Y. Li, X. Lu, S. Luan, Y. Wang, Y. Li and F. Gao, *J. Hazard. Mater.*, 2019, **373**, 367–376.
- 254 H. Zong, L. Hu, Z. Wang, R. Qi, K. Yu and Z. Zhu, *Chem. Eng. J.*, 2021, **416**, 129102.
- 255 X. Liu, F. Liu, X. Zhao and L. Z. Fan, *J. Mater.*, 2022, **8**, 30–37.
- 256 H. Zong, R. Qi, K. Yu and Z. Zhu, *Electrochim. Acta*, 2021, 393, 139068.
- 257 J. Li, C. Chen, Z. Lv, W. Ma, M. Wang, Q. Li and J. Dang, *J. Mater. Sci. Technol.*, 2023, 145, 74–82.
- 258 H. Wang, J. Zhao, J. Yu and Z. Wang, *Synth. Met.*, 2023, **292**, 117215
- 259 Y. Ma, H. Zhang, H. Cong, Y. Wang, S. Xin, P. Xu, Y. Qin, G. Xu, X. Kang and F. Wang, J. Alloys Compd., 2023, 968, 171985.
- 260 Y. Cui, L. Zhao, D. He, J. Sun, J. Yang, W. Tang, H. Yu, C. Lou, W. Wang, X. Zhang and H. Zhao, ACS Appl. Mater. Interfaces, 2024, 16, 47751–47762.
- 261 M. Zhang, S. Yun, T. Yang, G. Yang, M. Sun, J. Dang, Z. Wang, H. Yang, S. Yuan, A. Arshad and K. Wang, *J. Mater. Chem. A*, 2024, 12, 29479–29492.
- 262 T. Hou, Z. Jia, B. Wang, H. Li, X. Liu, Q. Chi and G. Wu, Chem. Eng. J., 2021, 422, 130079.
- 263 Y. Yang, X. Huang, C. Sheng, Y. Pan, Y. Huang and X. Wang, J. Alloys Compd., 2022, **920**, 165908.
- 264 H. Li, J. Li, L. Ma, X. Zhang, J. Li, J. Li, T. Lu and L. Pan, *J. Mater. Chem. A*, 2023, **11**, 2836–2847.

265 X. Shi, W. Liang, G. Liu, B. Chen, L. Shao, Y. Wu, Z. Sun and F. García, *Chem. Eng. J.*, 2023, **462**, 142271.

- 266 L. Wang, Z. Liu, Y. Ma, Z. Li, M. Xiao, B. Tu and H. Song, *Dalton Trans.*, 2023, 572–581.
- 267 W. Liang, M. Liu, X. Shi, B. Chen, L. Shao, J. Xu and Z. Sun, *Batter. Supercaps*, 2023, 7, e202300462.
- 268 R. Hu, D. Sha, X. Cao, C. Lu, Y. Wei, L. Pan and Z. M. Sun, *Adv. Energy Mater.*, 2022, **12**, 2203118.
- 269 J. H. Na, H. G. Oh, S. Lee and S. K. Park, *J. Mater. Chem. A*, 2023, **12**, 2848–2855.
- 270 S. Vallem, S. Song, Y. Oh, J. Kim, M. Li, Y. Li, X. Cheng and J. Bae, *J. Colloid Interface Sci.*, 2024, **665**, 1017–1028.
- 271 Y. Xue, W. Li, R. Liu, T. Zhao, Y. Lv, J. Li, Y. Guo, R. Hao, X. Liu and H. He, *Batter. Supercaps*, 2025, e202400770.
- 272 H. Zou, B. He, P. Kuang, J. Yu and K. Fan, *ACS Appl. Mater. Interfaces*, 2018, **10**, 22311–22319.
- 273 J. Wei, F. Hu, C. Lv, L. Bian, X. Quan and Q. Ouyang, *Small*, 2025, **21**, 2411146.
- 274 Q. Li, Q. Jiao, Y. Yan, H. Li, W. Zhou, T. Gu, X. Shen, C. Lu, Y. Zhao, Y. Zhang, H. Li and C. Feng, *Chem. Eng. J.*, 2022, 450, 137922.
- 275 M. Adil, A. G. Olabi, M. A. Abdelkareem, H. Alawadhi, A. Bahaa, K. ElSaid and C. Rodriguez, *J. Energy Storage*, 2023, **60**, 106537.
- 276 K. Farooq, M. Murtaza, Z. Yang, A. Waseem, Y. Zhu and Y. Xia, *Nanoscale Adv.*, 2024, **6**, 3169–3180.
- 277 L. Hu, R. Xiao, X. Wang, X. Wang, C. Wang, J. Wen, W. Gu and C. Zhu, *Appl. Catal.*, *B*, 2021, **298**, 120599.
- 278 K. Kasinathan, Y. K. Park, B. Ravindran, K. Marimuthu, G. Munuswamy-Ramanujam, S. Woong Chang and J. H. Yim, *Chem. Eng. J.*, 2024, 482, 149088.
- 279 A. Alshraim, S. Rahman, M. Al-Gawati, A. N. Grace and A. N. Alodhayb, *Int. J. Electrochem. Sci.*, 2025, 20, 100980.
- 280 Y. Zhang, Z. Li, B. Qu, X. Shen, L. Tong, J. Wang, J. Cui, X. Li, Q. Xie and J. Wang, *Inorg. Chem.*, 2025, 64, 6822–6831.
- 281 X. Liu, Y. Zhang and Y. Q. Liu, Appl. Surf. Sci., 2025, 694, 162859.
- 282 J. Zhou, G. Zhang, J. Luo, Y. Hu, G. Hao, H. Guo, F. Guo, S. Wang and W. Jiang, *Chem. Eng. J.*, 2021, **426**, 130725.
- 283 W. Gu, M. Wu, J. Xu and T. Zhao, *Int. J. Hydrogen Energy*, 2022, 47, 17224–17232.
- 284 T. Wu, F. Ren, Z. Guo, J. Zhang, X. Hou, Z. Chen, Y. Jin and P. Ren, *J. Alloys Compd.*, 2024, **976**, 172984.
- 285 Q. Liao, M. He, Y. Zhou, S. Nie, Y. Wang, B. Wang, X. Yang, X. Bu and R. Wang, *Langmuir*, 2018, **34**, 15854–15863.
- 286 B. Deng, Z. Xiang, J. Xiong, Z. Liu, L. Yu and W. Lu, *Nano-Micro Lett.*, 2020, 12, 55.
- 287 M. Wang, P. Zhou, T. Feng, Z. Song, Q. Ren, H. Gu, X. Shi, Q. Zhang and L. Wang, *Ceram. Int.*, 2022, 48, 22681–22690.
- 288 C. Cui, L. Geng, S. Jiang, W. Bai, L. Dai, E. Ren, L. Liu and R. Guo, *Ind. Eng. Chem. Res.*, 2023, **62**, 8297–8311.
- 289 J. Zheng, C. Xu, Z. Li, C. Gu, X. Li, Z. Li, Y. Li, G. Lou and Y. Chen, *J. Mater. Chem. A*, 2024, **12**, 29103–29112.
- 290 Z. Guo, Y. Zhao, P. Luo, J. Wang, L. Pei, H. Yu, P. Song, F. Ren and P. Ren, *Chem. Eng. J.*, 2024, 497, 155707.
- 291 Y. Yao, Y. Ma, C. Chen, K. Zhu, G. Wang, D. Cao and J. Yan, J. Energy Storage, 2025, 114, 115877.

- 292 Q. Liu, H. Zhang, J. Xie, F. Yang, Z. Yang, X. Liu, H. Wu, Q. Liu and X. Lu, *Nano Energy*, 2023, **113**, 108567.
- 293 Y. Wang, R. Niu, L. Chen, Y. Yang, H. Yu and X. Qiu, *Chem. Eng. J.*, 2025, **512**, 162305.
- 294 M. Daniel, G. Mathew, M. Anpo and B. Neppolian, *Coord. Chem. Rev.*, 2022, **468**, 214627.
- 295 B. Mohanty, S. Kumari, P. Yadav, P. Kanoo and A. Chakraborty, *Coord. Chem. Rev.*, 2024, **519**, 216102.
- 296 Y. Lu, J. Sun, W. Xu, X. Di, W. Zhao, L. Zhang and G. Pan, *IEEE Sens. J.*, 2025, 25, 5294–5303.
- 297 S. Vallem, S. Venkateswarlu, Y. Li, S. Song, M. Li and J. Bae, *Energy Storage Mater.*, 2024, **65**, 103159.
- 298 K. Farooq, Z. Yang, M. Murtaza, M. A. Naseeb, A. Waseem, Y. Zhu and Y. Xia, *Adv. Energy Sustain. Res.*, 2025, 2400400.
- 299 J. Liu, L. Chen, H. Cui, J. Zhang, L. Zhang and C.-Y. Su, Chem. Soc. Rev., 2014, 43, 6011–6061.
- 300 Y. Wang, J. Chen, J. Shi, J. Zhang, Y. Ma, X. Yang and Y. Li, *Appl. Surf. Sci.*, 2025, **710**, 163965.
- 301 B. Shan, Y. Wang, X. Ji and Y. Huang, *Nano-Micro Lett.*, 2024, **16**, 212.
- 302 F. Wu, P. Hu, F. Hu, Z. Tian, J. Tang, P. Zhang, L. Pan, M. W. Barsoum, L. Cai and Z. Sun, *Nano-Micro Lett.*, 2023, 15, 194.
- 303 G. Song, Y. Shi, S. Jiang and H. Pang, *Adv. Funct. Mater.*, 2023, 33, 2303121.
- 304 J. Liu, T. A. Goetjen, Q. Wang, J. G. Knapp, M. C. Wasson, Y. Yang, Z. H. Syed, M. Delferro, J. M. Notestein, O. K. Farha and J. T. Hupp, *Chem. Soc. Rev.*, 2022, 51, 1045–1097.
- 305 S. Bai, M. Yang, J. Jiang, X. He, J. Zou, Z. Xiong, G. Liao and S. Liu, *npj 2D Mater. Appl.*, 2021, 5, 78.
- 306 Z. Qian, R. Zhang, Y. Xiao, H. Huang, Y. Sun, Y. Chen, T. Ma and X. Sun, *Adv. Energy Mater.*, 2023, **13**, 2300086.
- 307 A. Fattah-alhosseini, Z. Sangarimotlagh, M. Karbasi and M. Kaseem, *Nano-Struct. Nano-Objects*, 2024, **38**, 101192.
- 308 Y. Chen, Y. Qiu, T. Chen and H. Wang, *ACS Nano*, 2025, **19**, 6588–6600.
- 309 M. Garai, M. Mahato, S. Nam, E. Kim, D. Seo, Y. Lee, V. H. Nguyen, S. Oh, P. Sambyal, H. Yoo, A. K. Taseer, S. A. Syed, H. Han, C. W. Ahn, J. Kim and I. K. Oh, *Adv. Funct. Mater.*, 2023, 33, 2212252.
- 310 F. Wei, F. Liang, Y. Zhao, Z. Ji, T. Yan, R. Li, H. Liu, Y. Kong, H. He, W. Huang, C. Cao, W. Zhang, B. Fei and M. Ge, *J. Mater. Chem. A*, 2025, **13**, 13070–13080.
- 311 L. Sun, H. Wang, S. Zhai, J. Sun, X. Fang, H. Yang, D. Zhai, C. Liu, W. Q. Deng and H. Wu, J. Energy Chem., 2023, 76, 368–376.
- 312 H. Zhang, D. Xiong, Y. Xie, K. Wu, Z. Feng, K. Wen, Z. Li and M. He, *Colloids Surf.*, *A*, 2023, **656**, 130332.
- 313 W. Wang, J. Si, L. Yue, W. Zhang, Q. Chen, H. Huang, F. Lin, Y. Zhao, S. Meng and L. Liu, *Chem. Eng. J.*, 2025, 507, 160363.
- 314 J. Sun, L. Zhang, F. Li, F. Yang, M. Liu, S. Li and D. Zhang, Adv. Funct. Mater., 2025, 2501181.
- 315 J. Li, X. Qiang, B. Jia, L. Wang and X. Wu, *Appl. Surf. Sci.*, 2025, **695**, 162867.

A. M. Shehzad, A. Shahzad, O. Sahin and S. Shahzad, RSC Adv., 2025, 15, 17130-17141.

RSC Advances

- 317 J. Kunwar, D. Acharya, K. Chhetri, B. Karki, B. Deo, R. M. Bhattarai, S. Neupane, M. P. Adhikari and A. P. Yadav, J. Electroanal. Chem., 2023, 950, 117915.
- 318 C. Ruan, D. Zhu, J. Qi, Q. Meng, F. Wei, Y. Ren, Y. Sui and H. Zhang, Surf. Interfaces, 2021, 25, 101274.
- 319 I. Pathak, D. Acharya, K. Chhetri, P. Chandra Lohani, S. Subedi, A. Muthurasu, T. Kim, T. H. Ko, B. Dahal and H. Y. Kim, J. Mater. Chem. A, 2023, 11, 5001-5014.
- 320 C. Liu, W. Feng, Y. Bai and H. Pang, Inorg. Chem. Front., 2022, 9, 5463-5468.
- 321 N. Hussain and S. M. Mobin, Chem. Sci., 2025, 16, 8460-
- 322 Y. Shi, F. Dong, A. Rodas-Gonzalez, G. Wang, L. Yang, S. Chen, H.-B. Zheng and S. Wang, Food Chem., 2025, 475, 143362.
- 323 Y. Wang, X. Wang, M. Chu, J. Xin, Y. Liu, H. Pang, G. Yang and H. Ma, Anal. Chim. Acta, 2025, 1346, 343770.
- 324 X. Wang, X. Bai, W. Wang, Z. Zhao and J. Shan, J. Electrochem. Soc., 2023, 170, 037519.
- 325 M. Ravipati, D. Ramasamy and S. Badhulika, Electrochim. Acta, 2025, 525, 146154.
- 326 X. Zheng, M. Yuan, P. Su, J. Xu and G. Sun, Appl. Surf. Sci., 2025, 692, 162742.
- 327 M. Murtaza, K. Farooq, W. A. Shah and A. Waseem, Fuel, 2025, 394, 135095.
- 328 Z. H. Zhu, X. Y. Wu, J. F. Lu, H. Xu, S. L. Hou, J. Zhao, S. J. Liu and H. R. Wen, Inorg. Chem., 2025, 64, 8261-8269.
- 329 A. P. Tiwari, P. Chandra, M. S. Rahman, K. A. Mirica and W. J. Scheideler, Nanoscale, 2025, 17, 11028-11036.

- 330 J. Jiang, C. Xi, Y. Zhao, Y. Zhu, K. Hu, Y. Wang, S. Wang, Z. Zhang and S. Han, ACS Catal., 2025, 15, 2561-2575.
- 331 I. Pathak, D. Acharya, K. Chhetri, Y. R. Rosyara, A. Muthurasu, T. Kim, T. H. Ko and H. Y. Kim, Composites, Part B, 2025, 296, 112238.
- 332 T. Fang, J. Ma, Y. Dai, J. Gou, X. Li, C. Li and J. Tong, ACS Appl. Nano Mater., 2025, 8, 3519-3526.
- 333 S. Raza, A. U. Rehman, C. Chen, T. Zhao, A. Hayat, T. Bashir, L. Shen, Y. Orooji and H. Lin, J. Mater. Chem. A, 2025, 13, 4390-4403.
- 334 X. Guo, H. Zhang, Y. Yao, C. Xiao, X. Yan, K. Chen, J. Qi, Y. Zhou, Z. Zhu, X. Sun and J. Li, Appl. Catal., B, 2023, 323, 122136.
- 335 W. Zhan, L. Ma and M. Gan, Mater. Today Chem., 2022, 26,
- 336 Y. Zhou, Y. Duan, Y. Liu, Y. Geng, Z. Jin, L. Yu and S. Li, Appl. Surf. Sci., 2025, 691, 162621.
- 337 Z. Lin, H. Xiao, Y. Chen and H. Cai, J. Alloys Compd., 2025, 1020, 179368.
- 338 O. Peng, W. Yu, C. Gao, L. Geng, P. Fatehi, S. Wang and F. Kong, Adv. Compos. Hybrid Mater., 2025, 8, 232.
- 339 G. Zhang, G. Zhang, H. Zhang, Y. Lu, Q. Shi, R. Li and J. Song, Appl. Surf. Sci., 2025, 688, 162327.
- 340 Y. Zhu, Y. Yang, S. Li, C. Zhu, Z. Qiu and Q. Zhu, New J. Chem., 2025, 49, 2889-2897.
- 341 M. H. Memon, A. Mir, F. Rehman, U. Amjad and M. Mustafa, Energy Technol., 2025, 2500041.
- 342 P. Wang, B. He, B. Wang, S. Liu, Q. Ye, F. Zhou and W. Liu, Chem. Eng. J., 2023, 474, 145835.
- 343 A. S. Alqahtani, A. S. Alahmari, Z. E. Eldin and S. Elbeltagi Inorg. Chem. Commun., 2025, 176, 114128.